Title
Utilization of Intestinal Monolayers to Study Stem Cell Differentiation and Drug Toxicity

Author
Bieber, Jake Matthew

Publication Date
2022

Peer reviewed|Thesis/dissertation

Utilization of Intestinal Monolayers to Study Stem Cell Differentiation and Drug Toxicity

by

Jake Bieber

DISSERTATION

Submitted in partial satisfaction of the requirements for degree of

DOCTOR OF PHILOSOPHY

in

Bioengineering

in the

GRADUATE DIVISION

of the

UNIVERSITY OF CALIFORNIA, SAN FRANCISCO
AND
UNIVERSITY OF CALIFORNIA, BERKELEY

Approved:

DocuSigned by:
Lani Wu
6F84CA582ABA4BF...

Lani Wu

Chair

DocuSigned by:
Steven Altschuler
DocuSigned by:
Kevin Healy
DocuSigned by:
Ophir Klein
F985C63D8CE3437...

Steven Altschuler

Kevin Healy

Ophir Klein

Committee Members

ACKNOWLEDGEMENTS

I am extremely grateful to all of those that have supported me throughout my graduate studies.

My graduate advisors, Steven Altschuler and Lani Wu, who enabled me to pursue scientific questions I found interesting, while providing guidance to turn these pursuits into successful endeavors. I know Steve and Lani will always celebrate my successes and be there to provide mentorship for any challenges I face in the future.

The Altschuler-Wu Lab for providing an amazing community to conduct science in. A special thank you to Laura Sanman who taught me everything I know about guts. Vany Sun, Heinz Hammerlindl, Feng Bao, Maike Roth, and Megan Koleske for helping me complete my review experiments. Capria Rinaldi for being there for all the highs and lows of grad school.

My qualifying and thesis committee members, Ophir Klein, Kevin Healy, Zev Gartner, Averil Ma, and Seth Shipman, who have helped shape my research over the last four years.

To my friends who made the last five years so enjoyable. I am lucky that my college friends, Sebastian Yllanes, Alexander Broholm, and Tucker Brownell all moved to San Francisco and were around to spend almost every weekend with. While I wish Sadie Alpertson, Henry Sokol, and Jasmine Tang were in the bay area, I am grateful for all our trips and phone calls. After college it is challenging to make new friends, but I did make one sure to be life-long friend, Ivana Vasic.

To my family for always being there for me and trying their best to understand my research. Max and Andie not only are you my siblings, but you truly are my best friends. To my mom and dad for always supporting me and instilling in me the confidence to pursue my dreams.

Julian Dishart, meeting you was the best thing that happened in graduate school, and I am excited to spend the rest of my life with you. Not only do you make me a better scientist, but you make me a better person, and for that I will always be grateful.

CONTRIBUTIONS

Sanman L.E., Chen I.W., **Bieber J.M.**, Thorne C.A., Wu L.F., & Altschuler S.J. (2020). Generation and Quantitative Imaging of Enteroid Monolayers. In: Ordóñez-Morán P. (eds) Intestinal Stem Cells. Methods in Molecular Biology, 2171, 99-113.

Sanman L.E., Chen I.W., **Bieber J.M.**, Steri V., Trentesaux C., Hann B., Klein O.D., Wu L.F., & Altschuler S.J. (2021). Transit-Amplifying Cells Coordinate Changes in Intestinal Epithelial Cell-Type Composition. Developmental Cell, 56(3), 356-365.

Bieber J.M., Sanman L.E., Xiaoxiao S., Hammerlindl H., Bao F., Roth M.A., Koleske M.L., Huang L., Aweeka F., Wu L.F., & Altschuler S.J. (2022). Differential Toxicity to Murine Small and Large Intestinal Epithelium Induced by Oncology Drugs. Communications Biology, 5, 99.

ABSTRACT

Utilization of Intestinal Monolayers to Study Stem Cell Differentiation and Drug Toxicity

by

Jake M. Bieber

The intestinal epithelium is a single layer of cells that plays a critical role in digestion, absorbs nutrients from food, and coordinates the delicate interplay between microbes in the gut lumen and the immune system. Epithelial homeostasis is crucial for maintaining health; disruption of homeostasis results in disorders including inflammatory bowel disease and cancer. The advent of 3D intestinal epithelial organoids has greatly advanced our understanding of the molecular underpinnings of epithelial homeostasis and disease. Recently, we developed an intestinal monolayer culture system that recapitulates important features of 3D organoids and the in vivo intestinal epithelium such as tissue renewal, representation of diverse epithelial cell types, self-organization, and apical-basolateral polarization. Intestinal monolayers are cultured in microtiter plates, enabling high-throughput experiments. Furthermore, their 2D nature makes it easier to distinguish individual cells by fluorescent microscopy, enabling quantitative analysis of single cell behaviors within the epithelial tissue.

In Chapter 1, I describe experimental methods for generating intestinal monolayers and computational methods for analyzing immunofluorescence images of intestinal monolayers. We outline experimental methods for generating intestinal monolayers from freshly isolated intestinal crypts, frozen intestinal crypts, and 3D organoids. Fresh crypts are easily obtained from murine or human intestinal samples, and the ability to derive intestinal monolayers from both frozen crypts and 3D organoids enables genetic modification and/or biobanking of patient samples for future studies. We outline computational methods for identifying distinct epithelial

cell types in immunofluorescence images of intestinal monolayers. Together, these methods enable detailed studies of epithelial homeostasis and drug-induced gastrointestinal toxicity.

In Chapter 2, I investigate the responses of the intestinal epithelium to individual and paired perturbations across eight epithelial signaling pathways to better understand how complex milieus of microenvironmental signals are interpreted to coordinate tissue cell-type composition. Renewing tissues have the remarkable ability to continually produce both proliferative progenitor and specialized differentiated cell types. Using a high-throughput approach that combines intestinal monolayers and quantitative imaging, we identified conditions that enrich for specific cell types as well as interactions between pathways. Importantly, we found that modulation of transit-amplifying cell proliferation changes the ratio of differentiated secretory to absorptive cell types. These observations highlight an underappreciated role for transit-amplifying cells in the tuning of differentiated cell-type composition.

Finally, in Chapter 3, I establish the ability to use murine small and large intestine-derived monolayers to screen drugs for toxicity. Gastrointestinal toxicity is a major concern in the development of drugs. As a proof-of-concept, we applied this system to assess gastrointestinal toxicity of ~50 clinically used oncology drugs, encompassing diverse mechanisms of action. Nearly all tested drugs had a deleterious effect on the gut, with increased sensitivity in the small intestine. The identification of differential toxicity between the small and large intestine enabled us to pinpoint differences in drug uptake, drug metabolism and cell signaling across the gut. These results highlight an under-appreciated distinction between small and large intestine toxicity and suggest distinct tissue properties important for modulating drug-induced gastrointestinal toxicity. The ability to accurately predict where and how drugs affect the murine gut will accelerate preclinical drug development.

TABLE OF CONTENTS

LIST OF FIGURES

LIST OF TABLES

LIST OF ABBREVIATIONS

2D	two-dimensional
3D	three-dimensional
4-HC	4-hydroperoxycyclophosphamide
4-OHCP	4-hydroxycyclophosphamide
aSMA	alpha-smooth muscle actin staining
BMP	bone morphogenetic protein
BSA	bovine serum albumin
CP	cyclophosphamide
CYP450	cytochrome P450
DMSO	dimethyl sulfoxide
DTT	dithiothreitol
EE	enteroendocrine
ERL	erlotinib
EGFR	epidermal growth factor receptor
GEF	gefitinib
GSK3-i	glycogen synthase kinase 3-inhibitor
HBSS	Hank's Buffered Saline Solution
HDAC	histone deacetylase
IACUC	Institutional Animal Care and Use Committee
IL-4	interleukin 4
JAK	Janus kinase
LI	large intestine

Lyz	Lysozyme
MAPK	mitogen-activated protein kinase
mTOR	mechanistic target of rapamycin kinase
MTX	methotrexate
Muc2	Mucin-2
OBM	organoid basal media
OSI	osimertinib
PBS	phosphate buffered saline
PBS-T	tween-20 in PBS
PCFT	proton-coupled folate transporter
PEM	pemetrexed
qRT-PCR	quantitative reverse transcriptase PCR
RFC	reduced folate carrier
SATB2	special AT-rich sequence-binding protein 2
SI	small intestine
SSZ	sulfasalazine
TA	transit-amplifying
TGF-b	transforming growth factor beta
TUNEL	terminal deoxynucleotidyl transferase (TdT) dUTP nick-end labeling

CHAPTER 1

Generation and Quantitative Imaging of Enteroid Monolayers

INTRODUCTION

The development of three-dimensional (3D) organoids has greatly advanced our ability to study the intestinal epithelium in a con- trolled manner in vitro (Sato et al., 2009). Indeed, studies in 3D organoids over the past 10 years have revealed a multitude of insights into mechanisms of homeostatic maintenance and intestinal epithelial dysfunction in disease (van de Watering et al., 2015; Farin et al., 2016). To study the intestinal epithelium at the single-cell level in high-throughput, we recently developed an enteroid monolayer culture system which recapitulates key features of 3D organoids and the in vivo intestinal epithelium. Specifically, enteroid monolayers are composed of the major intestinal epithelial cell types (stem, transit-amplifying, goblet, Paneth, tuft, and enteroendocrine) and they also renew, self-organize, and polarize with apical face exposed. Enteroid monolayers are readily cultured for up to 2 weeks and maintain both distinct crypt-like regions composed of stem cells and villus-like regions composed of differentiated cells throughout the course of treatment. Enteroid monolayers are two-dimensional (2D) and can be cultured in 96-well imaging plates, facilitating high-throughput investigation of tissue-level and single-cell behaviors (Thorne et al., 2018).

Here, we first outline three methods (Figure 1.1) for deriving enteroid monolayer cultures: from freshly isolated and frozen murine small intestinal crypts and from 3D organoids. Fresh intestinal crypts are plentiful and highly reproducible when derived from laboratory mouse strains, enabling the quantitative comparison of hundreds of different experimental conditions with crypts from a single mouse. In contrast, freezing crypts or propagating crypts as 3D organoids prior to generating enteroid monolayers enables banking and/or genetically modifying

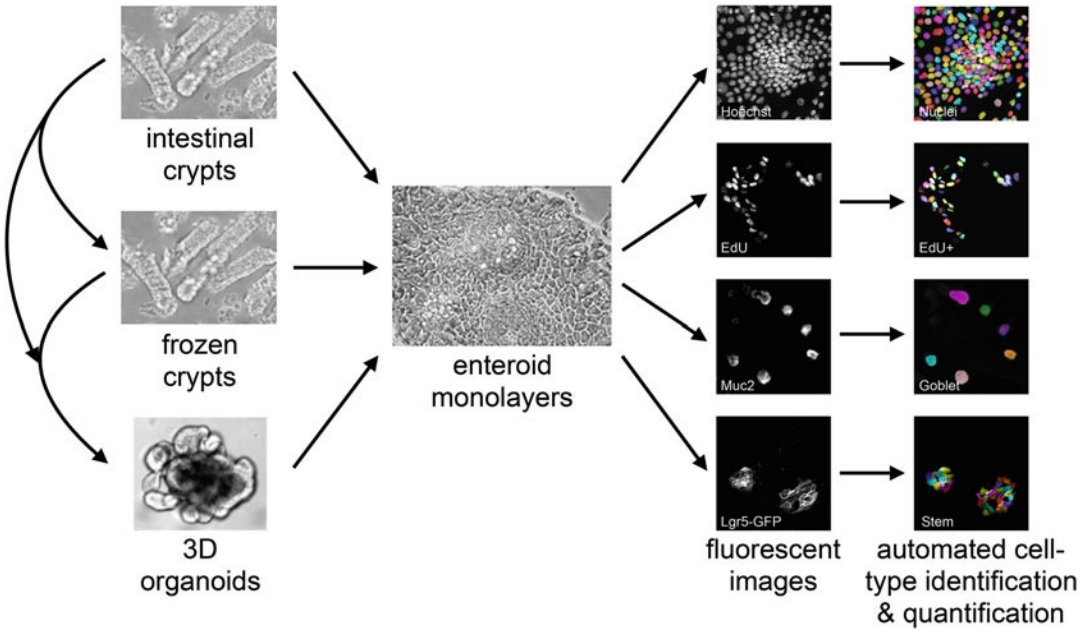

Figure 1.1: Workflow for generating and analyzing enteroid monolayers. Enteroid monolayers can be derived from fresh or frozen intestinal crypts and from 3D organoids. Immunofluorescence assays are used to identify the identity of individual cell types in enteroid monolayers. Numbers of each cell type in the resulting fluorescent images are quantified.

precious samples from patients or genetically engineered mice. We also describe an immunofluorescence protocol optimized for enteroid monolayers.

Second, we outline computational methods for segmenting (identifying) individual nuclei, EdU+ nuclei, Lgr5+ stem cells, and Muc2+ goblet cells in immunofluorescence images of enteroid monolayers. The synopsis of each method is accompanied by step-by-step instructions and links to a GitHub repository containing example code and sample images that should enable others to implement segmentation methods in their own research.

Taken together, the methods discussed below provide a detailed experimental and computational framework with which to generate and analyze enteroid monolayer cultures. These methods provide the opportunity to (1) disentangle the contributions of morphogens vs. 3D tissue architecture to tissue homeostasis, (2) easily access the luminal face of the epithelium, enabling studies of topics including host–microbiome interactions and drug trans- porters, and

(3) study single-cell identity and signaling in the tissue context in high throughput. With these advantages over more traditional 3D organoid models, enteroid monolayer cultures enable investigations to further our understanding of epithelial homeostasis and dysregulation in disease.

MATERIALS

Culturing Enteroid Monolayers from Freshly Isolated Murine Intestinal Crypts

1. Phosphate buffered saline (PBS): 137 mM NaCl, 2.7 mM KCl, 10 mM Na2HPO4, 1.8 mM KH2PO4 (no Ca2+/Mg2+).

2. Intestine washing buffer: PBS supplemented with 100 U/mL penicillin/100 µg/mL streptomycin.

> NOTE: If contamination is an issue, Primocin is another antimicrobial option that we have found to be effective and gentle on enteroid cultures; use at manufacturer's recommended concentration of 100 µg/mL.

3. Intestine harvest buffer: PBS supplemented with 1 mM EDTA, 2 mM dithiothreitol (DTT), 100 U/mL penicillin/100 µg/ mL streptomycin, and 10 µM Y-27632.

4. Crypt dissociation buffer: PBS supplemented with 3 mM EDTA, 2 mM DTT, 100 U/mL penicillin/100 µg/mL streptomycin, and 10 µM Y-27632.

> NOTE: Increase EDTA concentration to 5–10 mM and/or extend shaking and time in crypt dissociation buffer to harvest ileal crypts or colon crypts.

5. Organoid basal medium: Advanced DMEM/F12 with nonessential amino acids and sodium pyruvate and without L-glutamine, supplemented with 2 mM GlutaMAX, 10 mM HEPES, 100

U/mL penicillin/100 µg/mL streptomycin, 1 mM N- acetylcysteine, 1x N-2 supplement, and 1x B-27 supplement.

6. 100 µm cell strainer.

7. 70 µm cell strainer.

8. Forceps.

9. Dissecting scissors.

10. Growth factor–reduced Matrigel, phenol red-free.

11. Plating medium: organoid basal medium supplemented with 3 µM CHIR-99021, 50 ng/mL murine EGF, 100 ng/mL murine Noggin, 500 ng/mL murine R-spondin-1, and 10 µM Y-27632.

NOTE: The BMP receptor inhibitor LDN-193189 (100 nM to 1 µM) can be substituted for recombinant Noggin to save costs.

12. Long-term culture medium: organoid basal medium supplemented with 50 ng/mL EGF, 100 ng/mL Noggin, and 500 ng/mL R-spondin-1.

NOTE: R-spondin-1 conditioned medium (15%) can be substituted for recombinant R-spondin-1. We often observe more robust growth in R-spondin-1 conditioned medium, though it can suffer from batch-to-batch variability. Regardless of source, R-spondin-1 must be of high quality and concentration for optimal enteroid monolayer growth.

13. Glass microscope slides (e.g., 75 mm x 25 mm).

14. Brightfield or phase contrast inverted microscope.

15. 96-well clear polystyrene bottom imaging plates.

NOTE: There is batch-to-batch variability in plate manufacture that can affect enteroid monolayer growth and imaging. Specifically, plates that are as flat as possible and have minimal blue channel autofluorescence are ideal.

16. Wildtype or Lgr5-eGFP-DTR mice.

NOTE: Kind gift of Frederic de Sauvage via Ophir Klein under MTA #OM-216813 (Tian et al., 2012).

Culturing Enteroid Monolayers from Frozen Crypts

1. Matrigel, organoid basal medium, plating medium, and long-term culture medium.

2. Freezing medium: DMEM supplemented with 10% FBS and 10% dimethyl sulfoxide (DMSO).

Culturing Enteroid Monolayers from 3D Organoids

1. Matrigel, organoid basal medium, plating medium, and long-term culture medium.

2. TrypLE Express.

3. Fire-polished Pasteur pipettes.

4. Hemocytometer or automated cell counter.

Performing Immunofluorescence on Enteroid Monolayers

1. Fixation buffer: 4% PFA in PBS.

NOTE: We have also seen improvements in immunofluorescence signal-to-noise ratio using 4% PFA + 4% sucrose fixative.

2. Permeabilization buffer: 0.3% Triton-X-100 in PBS.

3. Blocking buffer: 3% bovine serum albumin (BSA) in PBS.

4. Antibody buffer: 1% BSA, 0.3% Triton-X-100 in PBS.

5. Washing buffer: 0.1% Tween-20 in PBS (PBS-T).

6. Click reaction buffer: 1 mM $CuSO_4$, 5 μM fluorophore-azide (e.g., sulfo-Cy5-azide; LumiProbe), and 100 mM sodium ascorbate in PBS.

NOTE: We find that it is best to prepare sodium ascorbate stock solutions fresh in water prior to preparing click reaction buffer.

7. Nuclear staining buffer: 5 μg/mL Hoechst 33342 in antibody buffer or PBS.

8. Primary antibody of interest.

9. Dye-conjugated species-specific secondary antibody (e.g., Alexa-conjugated antibodies).

Equipment

1. Automated point-scanning confocal or epifluorescent microscope.

Image Analysis Software

1. Miniconda3 (https://docs.conda.io/en/latest/miniconda. html).

2. Python 3.7.2 (https://www.python.org/downloads/, see below for installation).

3. Github repository of custom Python code (https://github. com/AltschulerWu-Lab/EnteroidSeg).

4. Install Miniconda3 for Python 3.7, which can be downloaded at the link above.

5. Download the Github repository linked above. The repository can be downloaded in the following ways: clone the repository using the Github desktop app (under Clone Repository, enter the link to the repository) or clone the repository using the command git clone followed by link to the repository.

6. Navigate to the EnteroidSeg directory in the downloaded repository. Install Python 3.7.2 and associated Python packages required for running the code using the following command.

conda env create --file1⁄4environment.yaml

7. Activate the conda environment with the following command.

source activate enteroidseg

METHODS

Culturing Enteroid Monolayers from Freshly Isolated Intestinal Crypts

1. Prepare intestine washing buffer (>30 mL per intestine), intestine harvest buffer (10 mL per intestine), and crypt dissociation buffer (10 mL per intestine) and keep on ice.

2. Prepare organoid basal medium (500 mL). Store a 50 mL aliquot at 4°C and warm the remainder to 37°C.

3. Thaw 10 mL vial of Matrigel on ice and make 1 mL aliquots. Prior to each experiment, thaw a Matrigel aliquot on ice. Avoid freeze-thaw cycles.

4. Thaw EGF, Noggin, and R-spondin-1 aliquots on ice.

5. Bring CHIR-99021 and Y-27632 aliquots to room temperature.

6. After organoid basal medium is warmed and EGF, Noggin, R-spondin-1, CHIR-99021, and Y-27632 are thawed, make plating medium (20 mL per intestine) and long-term culture medium (20 mL per intestine).

> NOTE: We store organoid basal medium for 2 months maximum. We store both plating and long-term culture medium for 1 week maximum.

7. Isolate small intestine from a male or female mouse between 6 and 12 weeks of age. We typically harvest the jejunum because it is the largest section of the mouse small intestine. Filet open longitudinally and wash in intestine washing buffer until fecal matter and debris are cleared.

8. Transfer washed intestine to intestine harvest buffer in 50 mL conical tube and incubate for 15 min on ice to loosen mucus and debris.

9. Shake intestine in intestine harvest buffer in 50 mL conical tube for 1 min. Use forceps to transfer intestine to crypt dissociation buffer in 50 mL conical tube and incubate for 1 h on ice with gentle rocking.

NOTE: If crypt yield is insufficient, one can also shake the conical tube containing intestine and crypt dissociation buffer every ~10 min during the incubation period.

10. During the 1 h incubation period, coat plates with Matrigel. In short: pipet Matrigel up and down gently to homogenize, mix Matrigel with ice-cold organoid basal medium at ratio of 1:40, aliquot 100 µL of Matrigel–medium mixture into each well of 96-well imaging plate, and place plate in 37°C tissue culture incubator for at least 30 min prior to using.

NOTE: We have also successfully cultured enteroid monolayers on Collagen I (Corning)-coated plates. Imaging is more difficult due to the thickness of the collagen coating. To perform Collagen I coating, add 50 µL/well of 1.6 mg/mL Collagen I diluted in long-term culture medium and NaOH (see manufacturer's instructions).

11. Shake intestine in crypt dissociation buffer for 1 min or until solution is cloudy. Shaking time can be extended if increased crypt yield is desired, though excessive shaking can cause deterioration of the crypt structures.

12. Remove intestine from crypt dissociation buffer and discard.

NOTE: Can keep intestine if one wants to have the option of shaking off more crypts. If so, place into a separate tube of crypt dissociation buffer rather than discarding.

13. Centrifuge crypt dissociation buffer at 300 x g for 3 min at room temperature. An epithelial cell pellet will be observed at the bottom of the tube.

14. Aspirate buffer. Resuspend epithelial cell pellet gently with 10 mL warm organoid basal medium. Centrifuge at 300 x g for 3 min at room temperature.

NOTE: Washes can be conducted in other buffers or media that contain Ca2+/Mg2+, we have personally tested Hank's Buffered Saline Solution (HBSS) and DMEM supplemented with 10% FBS.

15. Repeat step 14.

16. Aspirate medium. Resuspend in 10 mL warm organoid basal medium. Pass through 100 μm filter then 70 μm filter. Centrifuge at 300 x g for 3 min at room temperature.

17. Resuspend in 2–3 mL plating medium. Evaluate success of intestinal crypt harvest by observing a 10 μL aliquot on a glass slide under a brightfield or phase contrast microscope.

18. Determine crypt concentration by aliquoting 10 μL of crypt/ medium solution (1:10 dilution or no dilution) onto a glass slide and counting the number of crypts under a brightfield or phase contrast microscope.

19. Dilute crypts to a final concentration of 3000 crypts per mL in plating medium.

20. Remove Matrigel-coated 96-well imaging plates from tissue culture incubator and flick out medium into waste container in a laminar flow biosafety cabinet. Aliquot 100 μL of crypt/ medium solution into each well. Assess plating density and consistency under brightfield or phase contrast microscope.

21. Transfer plate to tissue culture incubator and incubate for 4 h.

NOTE: Length of incubation in plating media can vary from 4 to 24 h depending on the needs of the experiment, but 4 h is used as a default. Enteroid monolayers should not be cultured in media containing Y-27632 longer than 24 h.

22. After 4 h, flick medium out of plates and wash once with organoid basal medium. Add 100 μL of long-term culture medium to each well. Assess seeding efficiency under brightfield or

phase contrast microscope. At this point, crypts should have flattened out into disk-shaped enteroid monolayers.

NOTE: After changing into long-term medium, enteroid monolayers can be imaged on a brightfield point-scanning microscope to assess plating consistency. We find that between 10% and 30% confluent enteroid monolayers tend to grow to a consistent density and cell-type composition.

23. Add perturbations of interest. If perturbing cell-type composition, we typically treat with morphogens for 48 h prior to fixation and analysis. Change medium every 2 days to maintain optimal growth.

NOTE: When changing medium, if there is an excessive amount of debris, wash once with organoid basal medium prior to putting fresh long-term culture medium on enteroid monolayers.

NOTE: Generally, enteroid monolayers will increase in size for the first 3–4 days. A subset (~10%) of seeded crypts survives beyond 3–4 days and can be cultured for weeks. Enteroid monolayers derived from 3D cultures tend to not have this drop off in crypt survival.

Culturing Enteroid Monolayers from Frozen Crypts

Freezing Crypts

1. Prepare freezing medium.

2. Follow steps 1–18 of 'Culturing Enteroid Monolayers from Freshly Isolated Intestinal Crypts' to harvest intestinal crypts.

3. Centrifuge crypts at 300 x g for 3 min at room temperature.

4. Resuspend crypts to a final concentration of 3000–5000 crypts per mL in freezing medium.

5. Transfer 1 mL of crypts suspended in freezing medium to a cryovial and freeze in a freezing container in -80°C overnight and then transfer to liquid nitrogen for long-term storage.

Deriving Enteroid Monolayers from Frozen Crypts

1. Coat 96-well imaging plates with Matrigel as described in step 10 of 'Culturing Enteroid Monolayers from Freshly Isolated Intestinal Crypts'.

2. Prepare organoid basal medium, plating medium, and long-term culture medium.

3. Revive crypt aliquots by thawing cryovials in 37°C water bath.

4. Transfer crypts to 15 mL conical tube and add 9 mL warm organoid basal medium.

5. Centrifuge crypts at 300 x g for 3 min at room temperature.

6. Resuspend in warm plating medium to a final concentration of 3000 crypts per mL.

7. Follow steps 20–23 of 'Culturing Enteroid Monolayers from Freshly Isolated Intestinal Crypts' to generate enteroid monolayers.

Culturing Enteroid Monolayers from 3D Organoids

1. Generate 3D organoid cultures: embed freshly isolated intestinal crypts in Matrigel (200 crypts/100 µL Matrigel). Pipette 100 µL of Matrigel slowly into each well of a 24-well plate to form a dome. Place in 37°C incubator for 10 min to stiffen Matrigel. Once Matrigel has stiffened, add 500 µL long-term culture medium per well. Propagate 3D cultures as long as desired.

2. Coat 96-well imaging plates with Matrigel as described in step 10 of 'Culturing Enteroid Monolayers from Freshly Isolated Intestinal Crypts'.

3. Prepare organoid basal medium, plating medium, and long- term culture medium.

4. Warm TrypLE Express to 37°C.

5. Aspirate medium from around Matrigel domes containing 3D organoids.

6. Dissolve Matrigel dome and 3D organoids in cold organoid basal medium by adding organoid basal medium to well and then pipetting up and down several times to dislodge Matrigel.

7. Transfer cold medium, Matrigel, and 3D organoid mixture to 15 mL conical tube.

8. Add approximately 10 mL cold organoid basal medium to tube to further dissolve remaining Matrigel.

9. Centrifuge at 300 x g for 5 min at 4°C. A small organoid pellet should be visible at the bottom of the tube. If there appears to still be Matrigel in the pellet, aspirate medium and repeat step 8. The Matrigel will usually fully dissolve after a second wash with cold medium.

10. Aspirate medium and resuspend in a small volume (500–1000 µL) of cold organoid basal medium.

11. Shear organoids by running them through a fire-polished glass Pasteur pipet 8–10 times.

12. Centrifuge at 300 x g for 5 min at 4°C.

13. If 3D organoids contained many dead luminal cells, then aspirate medium, resuspend in cold organoid basal medium, and then centrifuge at 300 x g for 5 min at 4°C again.

14. Aspirate medium from organoids. Add 500 µL TrypLE Express and resuspend thoroughly. Incubate at 37°C for 5–10 min, shaking or triturating with a P1000 pipette a few times to break up cell clumps.

15. Add 5 mL warm organoid basal medium. Centrifuge at 300 x g for 5 min at room temperature.

16. Aspirate medium, resuspend in 5 mL warm organoid basal medium, and then centrifuge at 300 x g for 5 min at room temperature again.

17. Resuspend in small volume of plating medium. At this point, organoids should be single cells and some small clumps of cells.

18. Count cells using hemocytometer or automated cell counter.

19. Dilute cells to a final concentration of 50,000 cells per mL in plating medium.

20. Remove Matrigel-coated 96-well imaging plates from tissue culture incubator and flick out medium into waste container. Aliquot 100 μL of cell/medium solution into each well. Assess plating density and consistency under brightfield or phase contrast microscope.

21. After 18–24 h, flick medium out of plates. Add 100 μL of long- term culture medium to each well. There should be some cell aggregation at this point which will proceed over the course of the next 4–7 days to re-form crypt-villus–like patterning (Thorne et al., 2012). Change medium every 2 days to maintain optimal growth.

Performing Immunofluorescence on Enteroid Monolayers

1. Prepare PBS, washing buffer, fixation buffer, permeabilization buffer, blocking buffer, and antibody buffer.

2. If assaying proliferating cells, add 10 μM EdU in culture medium to enteroid monolayers for 1–2 h prior to fixation.

3. Flick medium out of plates. Wash once with 50 μL/well PBS.

4. Add 50 μL/well fixation buffer and incubate for 15 min at room temperature.

5. Wash three times with washing buffer. Add 50 μL/well permeabilization buffer and incubate for 10 min at room temperature.

> NOTE: Ice-cold methanol can be substituted for permeabilization buffer for specific antibodies; proceed according to manufacturer's instructions.

6. Flick permeabilization buffer out of plates. Wash three times with washing buffer. Add blocking buffer and incubate for 30 min at room temperature.

7. Flick blocking buffer out of plates. Wash three times with washing buffer. Add 25 μL/well antibody buffer containing primary antibody of interest. Incubate overnight at 4°C.

NOTE: We find it helpful to wrap imaging plates in wet paper towels and plastic wrap for overnight antibody incubation to maintain moisture.

8. Wash three times with 50 μL/well washing buffer for 5+ min each.

NOTE: Washes can be extended for antibodies that exhibit nonspecific staining.

9. Add 25 μL/well antibody buffer containing species-specific fluorescent secondary antibody of interest. Incubate for 2 h at room temperature in the dark.

10. Repeat step 8.

11. If assaying proliferating cells, prepare click reaction buffer. Wash three times with PBS and then add 50 μL click reaction buffer to each well. Incubate for 30 min at room temperature in the dark.

12. Wash three times with washing buffer and then add 50 μL nuclear staining solution to each well. Incubate for 30 min at room temperature in the dark.

13. Repeat step 8.

14. Store and image in washing buffer. Wrap in Parafilm for extended storage.

Quantitative Analysis of Immunofluorescence Images

Nuclear Segmentation

Nuclei in enteroid monolayers are highly heterogeneous in size and density with small, densely packed nuclei in crypt-like regions and large, sparsely distributed nuclei in villus-like regions (Thorne et al., 2012). To accommodate the range of nuclear characteristics, we employed a two-pass segmentation process. The first pass detects large, sparse nuclei and the second pass segments small dense nuclei. All parameters are set in DNA Segmentation section of the

config/seg_- params.yaml file. To skip parameter tuning and to run the script on the provided sample image, go to step 9.

1. Smooth image with a bilateral filter. Set parameters for bilateral filter: BILATERAL_SIGMA_COLOR (standard deviation for pixel value range over which pixels are averaged), BILATER- AL_SIGMA_SPATIAL (standard deviation for spatial distance range over which pixels are averaged).

2. Threshold image using a modified Otsu threshold method. Set parameter for thresholding: THRESHOLD_FACTOR (adjustment factor on Otsu threshold).

3. Detect location of nuclei using a multiscale Laplacian of Gaussian (LoG) method parameterized for large, sparse nuclei. Set parameters for sparse segmentation under LOG_SPARSE: MIN_SIG (lower bound for standard deviation of LoG filters), MAX_SIG (upper bound for standard deviation of LoG filters), NUM_SIG (number of standard deviations), THRESH (minimum intensity of peaks), OVERLAP (overlap allowance for neighboring objects).

4. Segment using watershed to separate connected nuclei. Set parameters for watershed: WATERSHED_CONN (neighbor- hood connectivity), WATERSHED_COMPACTNESS (com-pactness of segmented objects), WATERSHED_MIN_SZ (minimum size of segmented objects).

5. Detect and remove clumped nuclei from the sparse segmentation result. Clumped nuclei are detected based on both size and shape. Set parameters for clump detection: SEG_SINGLE_-MIN_SZ (minimum size of single nuclei. Objects below this threshold are considered single nuclei), SEG_SINGLE_- MAX_SZ (maximum size of single nuclei. Objects above this threshold are considered clumps of nuclei), SEG_CLUMP_- SOLIDITY (threshold for object

irregularity to classify objects between the minimum and maximum nuclear sizes as clumps), SEG_CLOSE_HOLES (maximum size of holes to remove in clump objects).

6. Detect locations of nuclei in clumped regions using a multiscale LoG method parameterized for small, densely packed nuclei. Set parameters for dense segmentation under LOG_DENSE. These parameters are the same as LOG_SPARSE in step 3 above.

7. Segment using watershed to separate connected nuclei. The same parameters as step 4 above are used. No additional parameters are needed for this step.

8. Combine sparse and dense segmentation outputs for the final nuclear segmentation. No parameters are needed for this step.

9. Set path to image in the enteroidseg/nuclear_segmentation.py file. The path is already set for the provided sample image.

10. Navigate to the enteroidseg folder and make sure the enteroidseg conda environment is activated. Run nuclear segmentation using the following command.

```
python nuclear_segmentation.py
```

The output results will be stored in the output folder.

EdU+ Nuclear Segmentation

We detect proliferating (S phase) cells by staining for EdU incorporation. EdU+ nuclei can be identified using a similar method to 'Nuclear segmentation'. The pipeline for segmenting EdU+ objects using the nuclei segmentation method is provided. To skip parameter tuning and to run the script on the provided sample image, go to step 3.

NOTE: EdU+ nuclei can also be identified using the EdU staining intensity in previously identified nuclear objects.

1. Set parameters for EdU segmentation under EdU Segmentation in seg_params.yaml. The parameters are the same as nuclear segmentation.

2. Set path to image in the edu_segmentation.py file. The path is already set for the provided sample image.

3. Navigate to the enteroidseg folder and make sure the enteroidseg conda environment is activated. Run the EdU segmentation using the following command.

```
python edu_segmentation.py
```

The output results will be stored in the output folder.

Goblet Cell Segmentation

Cell types in enteroid monolayers can be detected by staining with cell type–specific antibodies or by deriving enteroids from transgenic mice expressing cell-type markers. We identify goblet cells using anti-Mucin-2 (Muc2) antibody. The staining pattern encompasses cytoplasmic regions above the nuclear plane that may overlap multiple nearby nuclei. Thus, goblet objects are identified solely based on the Muc2 staining pattern. All parameters are set in the seg_params.yaml file under Goblet Segmentation. To skip parameter tuning and to run the script on the provided sample image, go to step 6.

1. Smooth image using a median filter. Set parameters for smoothing filter: MEDIAN_FILTER_SZ (radius of median filter).

2. Threshold image using a modified Otsu threshold method. Objects in thresholded image are expanded to the convex hull to create whole objects from partial membrane stains. Set parameters for thresholding: THRESHOLD_FACTOR (adjustment factor on Otsu threshold).

3. Detect goblet cell-object locations using a multiscale Laplacian of Gaussian method. Set parameters for segmentation under LOG_BLOB. These parameters are the same as LOG_SPARSE in step 3 of 'nuclear segmentation'.

4. Segment connected objects using watershed. Set parameters for watershed. The same parameters are used as in step 4 of 'nuclear segmentation'.

5. Set path to image in the goblet_segmentation.py file. The path is already set for the provided sample image.

6. Navigate to the enteroidseg folder and make sure the enteroidseg conda environment is activated. Run the goblet segmentation pipeline using the following command.

```
python goblet_segmentation.py
```

The output results will be stored in the output folder.

Stem Cell Segmentation

Stem cells are labeled by staining with anti-GFP antibodies in enteroid monolayers derived from Lgr5-eGFP-DTR mice (Tian et al., 2012). In enteroid monolayers derived from Lgr5-eGFP-DTR mice, GFP signal localizes to cell membranes (Tian et al., 2012), requiring first segmentation of GFP+ "crypt-base" regions followed by identification of stem cells in crypt-base regions using nuclear segmentation information. Therefore, both Lgr5-GFP and Hoechst stain images are required for stem segmentation. Optionally, for more accurate stem segmentation, Paneth segmentation is used to remove Paneth nuclei in crypt-base regions from the final result. Sample images for Lgr5-GFP stain, Hoechst stain, and Paneth segmentation are provided in the images folder. All parameters are set in the seg_params.yaml file under Stem Segmentation. To skip parameter tuning and to run the script on provided sample images, go to step 5.

NOTE: Enteroids derived from Lgr5-CreERT2 mice have mosaic Lgr5-GFP expression, which makes it impossible to segment all stem cells. Therefore, we greatly prefer enteroids derived from Lgr5-eGFP-DTR mice for stem cell segmentation purposes.

1. Threshold image to detect crypts. Set parameters for thresholding: DNA_FACTOR (removes any bleed through into GFP channel from Hoechst channel using Hoechst stain image), THRESH (manual threshold for Lgr5 stain).

2. Thresholded image is further processed using morphological operations to connect holes in the crypt base-like regions. Set parameters for morphological operations: MORPH_CLO- SING_SZ (radius of closing filter), MORPH_OPENING_SZ (radius of opening filter), MIN_SZ (minimum size of crypt-base regions in pixels).

3. Stem segmentation is finalized by identifying nuclei in the crypt regions and then (optionally) filtering out nuclei associated with Paneth cells. Set parameters for identification of nuclei: PARTIAL_RATIO (minimum ratio of nuclear area outside the crypt to the nuclear area inside the crypt to qualify as residing in the crypt).

4. Set path to image in the stem_segmentation.py file. The path is already set for the provided sample images.

5. Navigate to the enteroidseg folder and make sure the enteroidseg conda environment is activated. Run the stem segmentation pipeline by calling the stem_segmentation.py script using the following command.

```
python stem_segmentation.py.
```

The output results will be stored in the output folder.

CHAPTER 2

Transit-Amplifying Cells Coordinate Changes in Intestinal Epithelial Cell-Type Composition

INTRODUCTION

A central question in the study of complex tissues is how diverse signals are integrated to regulate cell-type composition. Dissection of mechanisms underlying the mapping from signals to tissue composition is complicated by the heterogeneous makeup of interconnected cell types, which exert influences upon one another through lineage structure and cell-cell interactions. Furthermore, due to the challenges of investigating combinatorial signal integration mechanisms, most studies have focused on the effects of individual signals on individual cell types. What are the tissue-wide effects of common microenvironmental signals on cell-type composition? How do multiple signals modify each other's effects? Finally, are there intrinsic tissue properties that shape response to diverse signals?

Here, we address these questions in the context of the intestinal epithelium, an ideal model for continuously renewing tissue (Beumer and Clevers, 2016; Cheng and Leblond, 1974a; Tian et al., 2016). The intestinal epithelium is particularly remarkable in that it maintains a stereotypic tissue composition despite a rapid 3- to 5-day turnover. During renewal of the intestinal epithelium, Lgr5+ crypt-base stem cells differentiate into proliferating transit-amplifying (TA) progenitors, which in turn adopt absorptive (enterocyte) or secretory (Paneth, goblet, enteroendocrine [EE]) cell fates (Cheng and Leblond, 1974a). The confluence of proliferation and differentiation decision processes establishes tissue composition, which guides overall tissue function. Much progress has been made in identifying individual

factors that guide intestinal epithelial renewal (Beumer and Clevers, 2021; Clevers, 2013; van der Flier and Clevers, 2009; Yin et al., 2014; Zhan et al., 2019). However, it is unclear how these factors—and combinations of them—are integrated by the tissue during maintenance and in response to perturbations.

To quantitatively measure intestinal epithelial cell-type composition and study its changes in response to microenvironmental signals, we utilized an enteroid monolayer culture system that recapitulates key features of the intestinal epithelium (Sanman et al., 2020; Thorne et al., 2018). Enteroid monolayer cultures maintain characteristics of intestinal epithelial architecture, including spatial organization into crypt-like proliferative and differentiated compartments and apical-basolateral polarization. Differentiated cell types (e.g., enterocyte, goblet, EE, and Tuft cells) surround proliferative compartments, within which stem and Paneth cells are juxtaposed and surrounded by TA cells (Thorne et al., 2018). Importantly, these cultures also preserve core tissue processes ex vivo, generating all major intestinal epithelial cell types (Lgr5+ stem, TA, and differentiated secretory and absorptive cells) with a turnover rate similar to the in vivo renewal rate. Due to their two-dimensional nature, enteroid monolayer cultures are amenable to high-throughput image-based assays in microwell format, which enables large numbers of tissue perturbations to be performed and analyzed. In this work, enteroid monolayers are used as a primary platform for hypothesis generation with key observations further evaluated in 3D organoids and in vivo.

Here, we present a systems approach for investigating signal integration and lineage processes in the intestinal epithelium. We expand the capabilities of the enteroid monolayer platform to monitor and quantify major proliferating progenitor and differentiated intestinal epithelial cell types. We profiled changes in stem, TA, and secretory cell types in response to a

diverse set of combinatorial treatment conditions. We identified conditions that enrich for stem and EE cells and elucidate an unexpected interaction between epidermal growth factor receptor (EGFR) and interleukin 4 (IL-4) signaling. Finally, we propose a model of intestinal epithelial lineage control in which modulation of TA proliferation can alter the balance of secretory to absorptive cell lineages, which is supported through experiments in enteroid monolayers, 3D organoids, and in vivo, as well as mathematical modeling.

RESULTS

A Quantitative Microscopy Platform to Study Regulation of Intestinal Cell-Type Composition

Here, we build on a previously described enteroid monolayer system for monitoring intestinal epithelium (Sanman et al.,2020; Thorne et al., 2018). We first expanded the computational pipeline to automatically quantify major intestinal cell types from images of enteroid monolayers. Specifically, we developed algorithms to detect cells expressing markers for stem (Lgr5+), proliferating (EdU+), Paneth (Lyz+), goblet (Muc2+), and EE (ChgA+) cells as well as to identify cell nuclei (Hoechst) (Figure 2.1 A–F). When evaluated against expert manual counting, the algorithms exhibited high quantification accuracy across the cell types measured (Table 2.1).

We then assessed recapitulation of relevant in vivo intestinal epithelial properties. First, we selected a crypt seeding density (10%–20% initial confluency) where there was relatively low inter-replicate variability and no relationship between initial seeding density and cell-type composition after 48 h of culture (Figure 2.1 G). Next, we confirmed that jejunal enteroid monolayers exhibited a cell-type composition comparable to the composition of in vivo jejunal

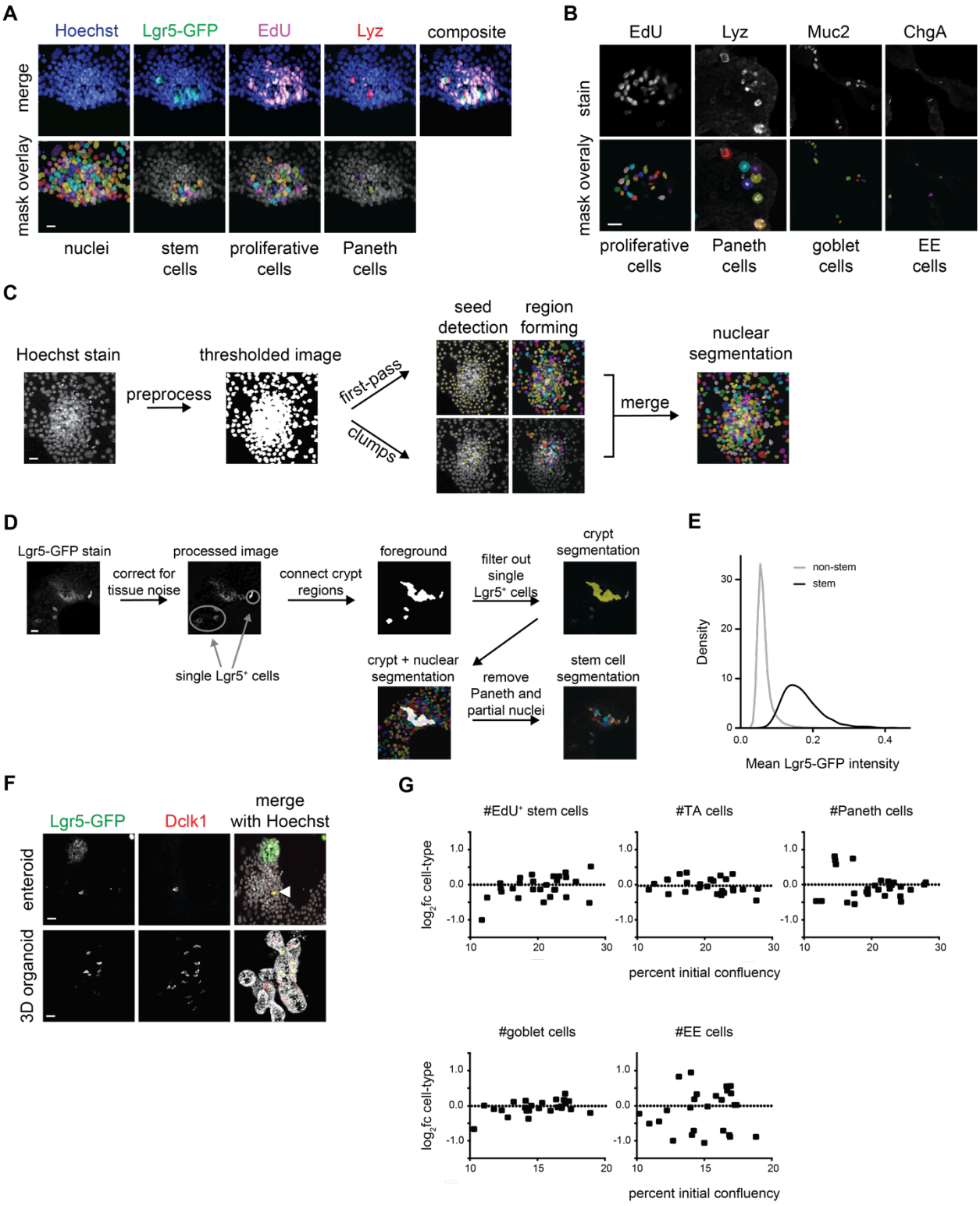

Figure 2.1: Quantification of intestinal epithelial cell types in immunofluorescence images of enteroid monolayers. (A) Example of crypt segmentation with pseudocolor overlay for each cell type readout. Scale bar 10μm. (B) Example of segmentation of proliferating, Paneth, goblet, and enteroendocrine (EE) cells. Top: raw stain image for the indicated marker. Bottom: pseudocolor overlay of each identified cell type. Scale bar 10μm. (C) Schematic of nuclear

(caption continued from previous page) segmentation steps. Thresholded Hoechst stain images were segmented in two passes. The first pass segmented sparse nuclei and the second pass segmented clumped nuclei. Sparse and clumped segmentation were merged into the final nuclear segmentation. Yellow dots indicate identified markers of nuclear object locations, multi-pseudocolor overlay depicts individual nuclei segmented using a watershed algorithm. Scale bar 10μm. (D) Schematic of stem cell segmentation. The Lgr5-GFP stain was first corrected for tissue noise and then thresholded. Size filtering was used to separate multi-cell membrane GFP regions (crypt regions) from single Lgr5-GFP+ cells. All nuclei in crypt regions (nuclei identified from Hoechst image segmentation of same region), with the exception of Paneth cell-associated nuclei, were counted as stem cells. Scale bar 10μm. (E) Distribution of mean Lgr5-GFP intensity for segmented stem and non-stem cells. Mean intensity of max-projected Lgr5-GFP stain images was quantified in stem and non-stem cell nuclear segmentation regions. The distributions are well separated, indicating identification of distinct Lgr5+ stem cells and Lgr5- non-stem cells. (F) Single Lgr5-GFP+ cells are also Dclk1+ in enteroid monolayers (top; scale bar 10μm) and 3D organoids (bottom; scale bar 15μm) and are thus excluded from stem cell counts. (G) Percent initial confluency was measured from brightfield images taken after crypt seeding and 48 h cell type composition was quantified from immunofluorescence images. Y axis: log2fc computed relative to the average of all wells. No relationship is observed between initial confluency and cell type frequencies.

epithelium (Table 2.2) (Cheng and Leblond, 1974b). Finally, we observed that enteroid monolayers recapitulate progenitor proliferation and production of differentiated cell types. By labeling cycling cells with EdU upon initial plating, we observed that the initial population of ~25% proliferative (EdU+) cells produced the vast majority (79.2 ± 2.2%) of enteroid monolayer cells by 48 h of culture (Figure 2.2 A; Tables 2.2 and 2.3). Further, we observed EdU+ cells that co-localized with markers of Paneth (Lyz), goblet (Muc2), and EE (ChgA) cells (Figure 2.2 B). Taken together, enteroid monolayers preserve important characteristics of the intestinal epithelium and provide a robust platform for capturing tissue-wide responses to perturbations and for generating hypotheses on control of intestinal epithelial cell-type composition.

Systematic Survey of Cell-Type Composition Changes in Response to Single and Pairwise Signaling Modulators

To map a wide range of tissue composition phenotypes, 13 epithelial-intrinsic and microenvironmental modulators that target eight core intestinal epithelial signaling pathways

(Wnt, bone morphogenetic protein [BMP], Notch, histone deacetylase [HDAC], Janus kinase [JAK], p38 mitogen-activated protein kinase [MAPK], transforming growth factor beta [TGF-b], and EGFR (Basak et al., 2017; van der Flier and Clevers, 2009; Houde et al., 2001; Richmond et al., 2018; Rodrıguez-Colman et al., 2017; Yin et al., 2014; Lukonin et al., 2020)) and that are known to have diverse effects on tissue-cell-type composition were selected (Table 2.4) (Batlle et al., 2002; Farin et al., 2016; Flentjar et al., 2007; van der Flier et al., 2009; Li et al., 2018; VanDussen et al., 2012). In previous reports, combinations of perturbations have been shown to be more effective than single perturbations in enriching for particular cell types (Basak et al.,

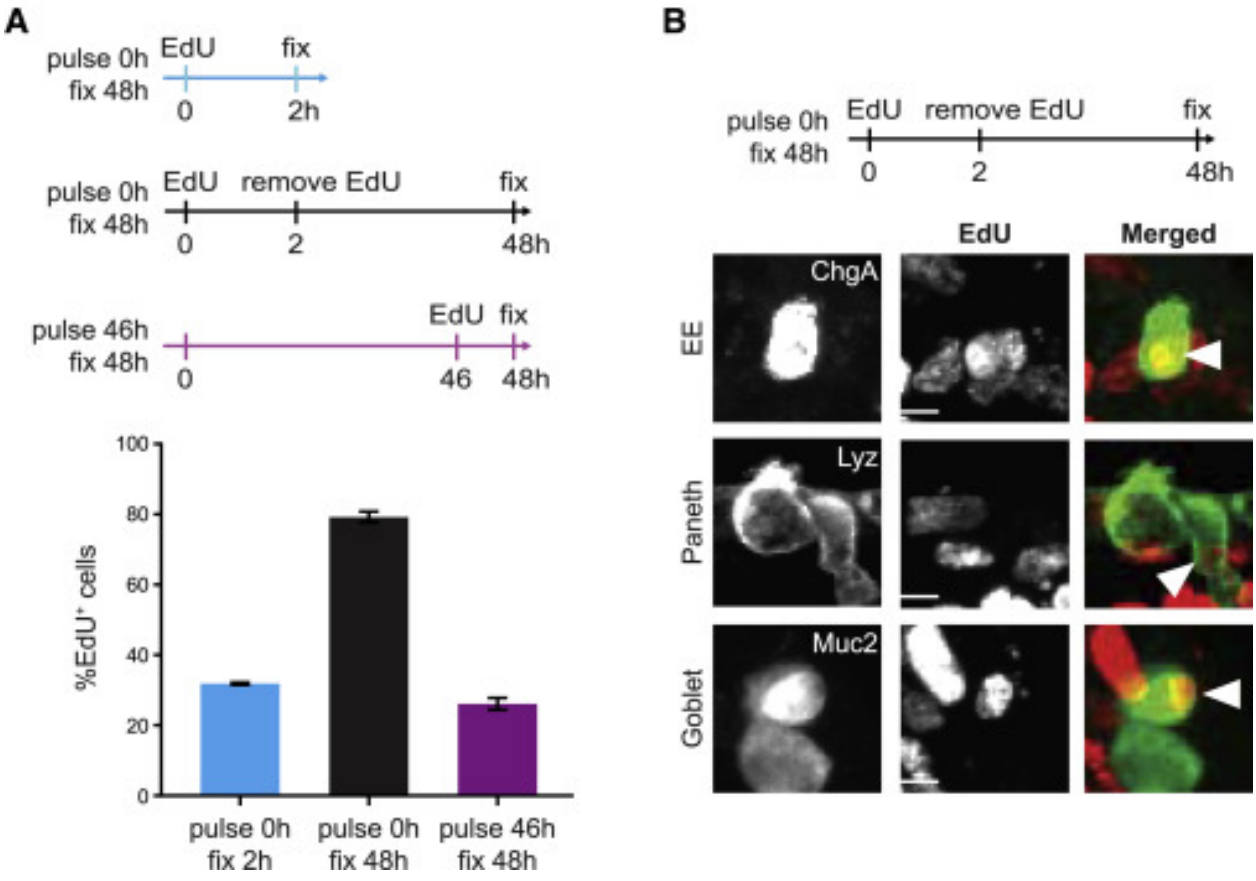

Figure 2.2: Enteroid monolayers provide a model for renewing intestinal epithelium. (A) Top: schema for EdU pulse chase. Bottom: quantification of %EdU+ cells in tissue at different time points. n = 3 wells. Error bars, mean±SEM. (B) Top: schema for EdU pulse chase. Bottom: representative images show co-localization between EdU and secretory cell-type markers (Lyz, Paneth; Muc2, goblet; and ChgA, EE). Arrowheads indicate cells that co-stain for EdU and the indicated cell type marker. Scale bars, 5μm.

2017; van der Flier and Clevers, 2009; Houde et al., 2001; Richmond et al., 2018; Rodrıguez-Colman et al., 2017; Yin et al., 2014). Thus, to survey a broad range of tissue states, modulators were applied to enteroid monolayers individually (13 conditions) and in all possible pairwise combinations (78 conditions). Perturbation concentrations were selected based on literature reports and dose-response experiments in enteroid monolayers (Table 2.4; Figure 2.3 A) (Basak et al., 2017; Dames et al., 2015; Han et al., 2014; Hong et al., 2017; von Moltke et al., 2016; Sato et al., 2011; Yin et al., 2014). A 48 h final time point was selected for our studies, as we observed strong and expected responses to well-characterized perturbations (Figure 2.3 B).

For our survey, we focused on changes to the proliferative progenitor and differentiated secretory subpopulations. We chose to report absolute numbers of the proliferative subpopulations (#stem and #TA) and fractions of secretory cell types within the measured secretory lineage (#Paneth/#secretory, #goblet/#secretory, and #EE/#secretory; Figures 2.3 C and 2.4 A). The number of proliferating stem cells was estimated by counting EdU+ Lgr5+ cells, and the number of TA cells—defined as non-stem proliferating cells—was estimated by counting EdU+ Lgr5 cells. The number of secretory cells was estimated by the sum of Paneth (Lyz), goblet (Muc2), and EE (ChgA) cells, which is a reasonable approximation, as they make up the majority of secretory cells (Cheng and Leblond, 1974a; Haber et al., 2017). While there are many possible features to report, focusing on absolute numbers of proliferating progenitor cells and relative fractions within the secretory lineage allowed us to disentangle changes within different tissue compartments from overall changes in tissue mass.

In total, the survey of single and pairwise perturbations allowed us to measure the effects of diverse perturbations on intestinal epithelial cell-type composition (546 measurements = 91

conditions 3 6 cell-type readouts), with a focus on progenitor and secretory cell regulation (Figure 2.4 B, single summary heatmap; Figure 2.3 D, alternative visualization and total cell numbers). These measurements allowed us to generate hypotheses about how microenvironmental signals interact with each other and regulate tissue-cell-type composition.

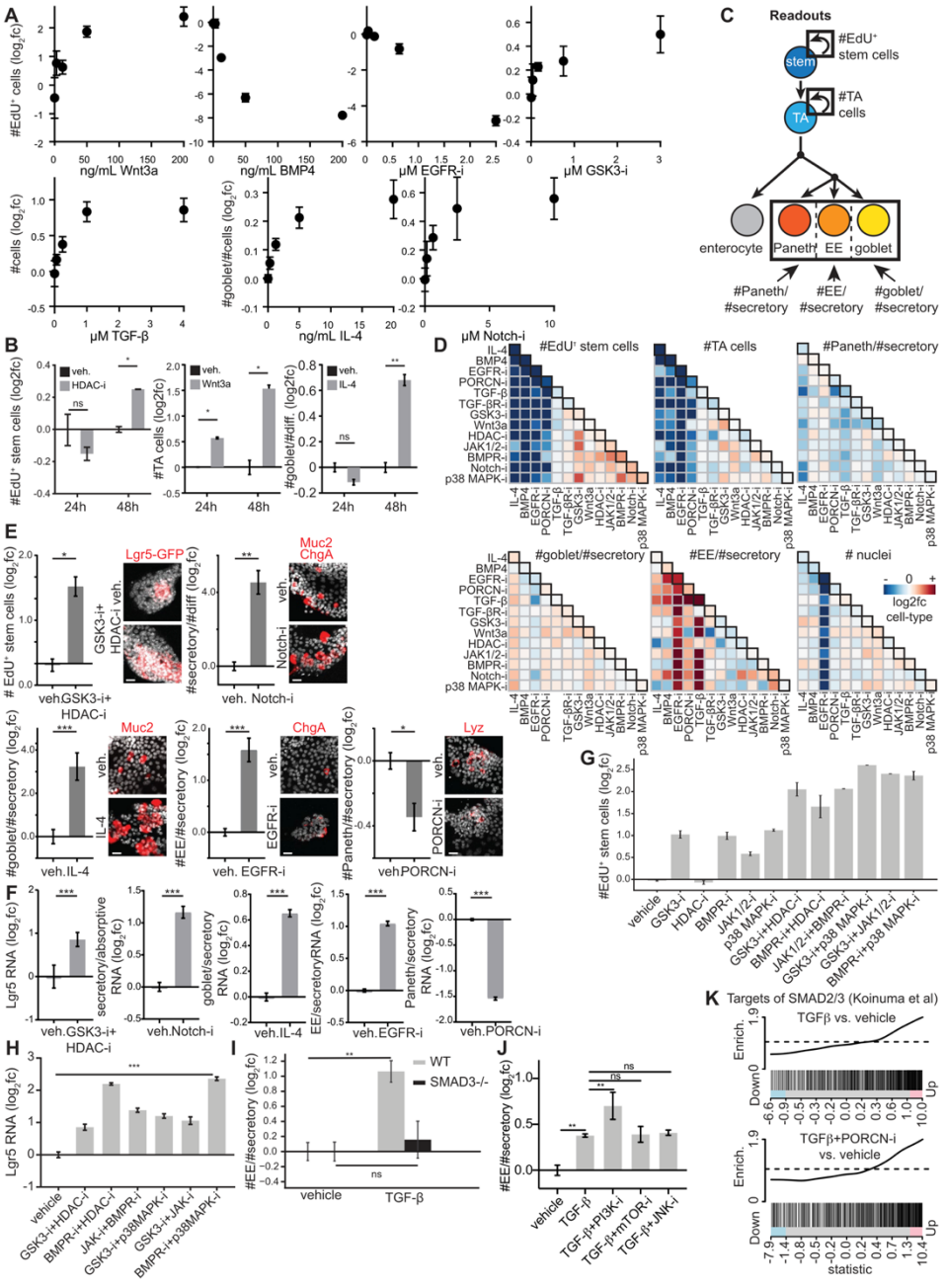

Figure 2.3: Dose optimization, feature design, and benchmarking for combinatorial perturbation screen. (A) Quantification of cell numbers and prevalence after perturbation with

(caption continued from previous page) increasing doses of Wnt3a, BMP4, EGFR-i, GSK3-i, TGF-β, IL-4, or Notch-i. All data are represented as the log2 fold-change effect relative to control. Fraction of goblet cells was calculated as a percentage of all cells for comparison with previous studies. n=4 (0μM, all conditions), 2 (Notch-i), or 3 (other conditions) wells. Error bars mean +/- SEM. (B) Quantification of cell type numbers for perturbations with known effects at 24 and 48 h. n= 2 wells. Error bars mean +/- SEM. (C) Schema of readouts. Proliferating progenitors: #EdU+ stem or #TA cells. Secretory lineage: #goblet/#secretory, #Paneth/#secretory, or #EE/#secretory. (D) Alternative visualizations of single and pairwise perturbation data. Quantification of progenitor readouts (#EdU+ stem and #TA cells), secretory cell type readouts (#Paneth/#secretory, #goblet/#secretory, #EE/#secretory), and total cell number (# nuclei). Single perturbation effects are depicted along the diagonal (black boxes). n=28 (controls), 6-8 (single perturbations), or 2 (pairwise perturbations) wells. (E) Enteroid monolayers respond as expected to modulators of stemness (GSK3-i + HDAC-i) and secretory cell prevalence (Notch-i, IL-4, EGFR-i, PORCN-i). Top: quantification of replicate wells. Bottom: representative images. Error bars mean +/- SEM. Scale bars 10μm. n=28 (vehicle), 4 (Notch-i), 8 (IL-4), 6 (EGFR-i), or 4 (PORCN-i) wells. (F) Similar changes to (E) in cell type composition are observed at the RNA level. Enteroid monolayers were treated as indicated for 48 h. Secretory/absorptive RNA= Atoh1/Hes1, Paneth RNA=Lyz, goblet RNA=Muc2, EE RNA=ChgA, secretory RNA=Lyz+Muc2+ChgA. Error bars mean +/- SEM. Veh=vehicle. n=9 (vehicle, Lgr5), 6 (vehicle, all other markers) or 3 (all perturbations) wells. (G) Single-compound controls for Lgr5 inducers in enteroid monolayers. Pairwise perturbations significantly increased ($p<0.05$) #EdU+ stem cells compared to vehicle or either single perturbations (except BMPR-i + HDAC-i). Error bars mean +/- SEM. n=28 (control), 6 (GSK3-i, BMPR-i, JAK1/2-i), 8 (HDAC-i, p38 MAPK-i) or 2 (pairwise perturbations). (H) Recapitulation of Lgr5+ stem cell-inducing conditions by qRT-PCR in enteroid monolayers. Enteroid monolayers were treated as indicated for 48 h. Pairwise perturbations significantly increased #EdU+ stem cells compared to vehicle. RNA levels were measured by qRT-PCR. Error bars mean +/- SEM. n=9 (vehicle) or 3 (perturbations) wells. (I) SMAD3 deletion abrogates TGF-β-mediated induction of EE cells. Enteroid monolayers derived from SMAD3-/- mice were treated for 48 h as indicated. Error bars mean +/- SEM. n=3 wells. (J) Inhibitors of non-canonical TGF-β effectors do not abrogate TGF-β induction of EE cells in enteroid monolayers. 48 h treatment. Error bars mean +/- SEM. n=3 wells. (K) TGF-β and TGF-β + PORCN-i upregulate SMAD2/3 target genes in 3D organoids ($p=0.02$) for both TGF-β and TGF-β + PORCN-i vs. vehicle) (Methods). * indicates p-values < 0.05; ** indicates p-values < 0.01; *** indicates p-values < 0.001; ns: not significant

Identification of Signaling Perturbations that Enrich for Specific Cell Types

Our survey recapitulated known effects on intestinal epithelial cell-type composition (glycogen synthase kinase 3-inhibitor [GSK3-i] + HDAC-i, Notch-i, IL-4, EGFR-i, and PORCN-i). In these cases, changes in enteroid monolayer cell type readouts were in agreement with previous studies (Basak et al., 2017; Beumer and Clevers, 2016; van Es et al., 2005; von Moltke et al., 2016; Qi

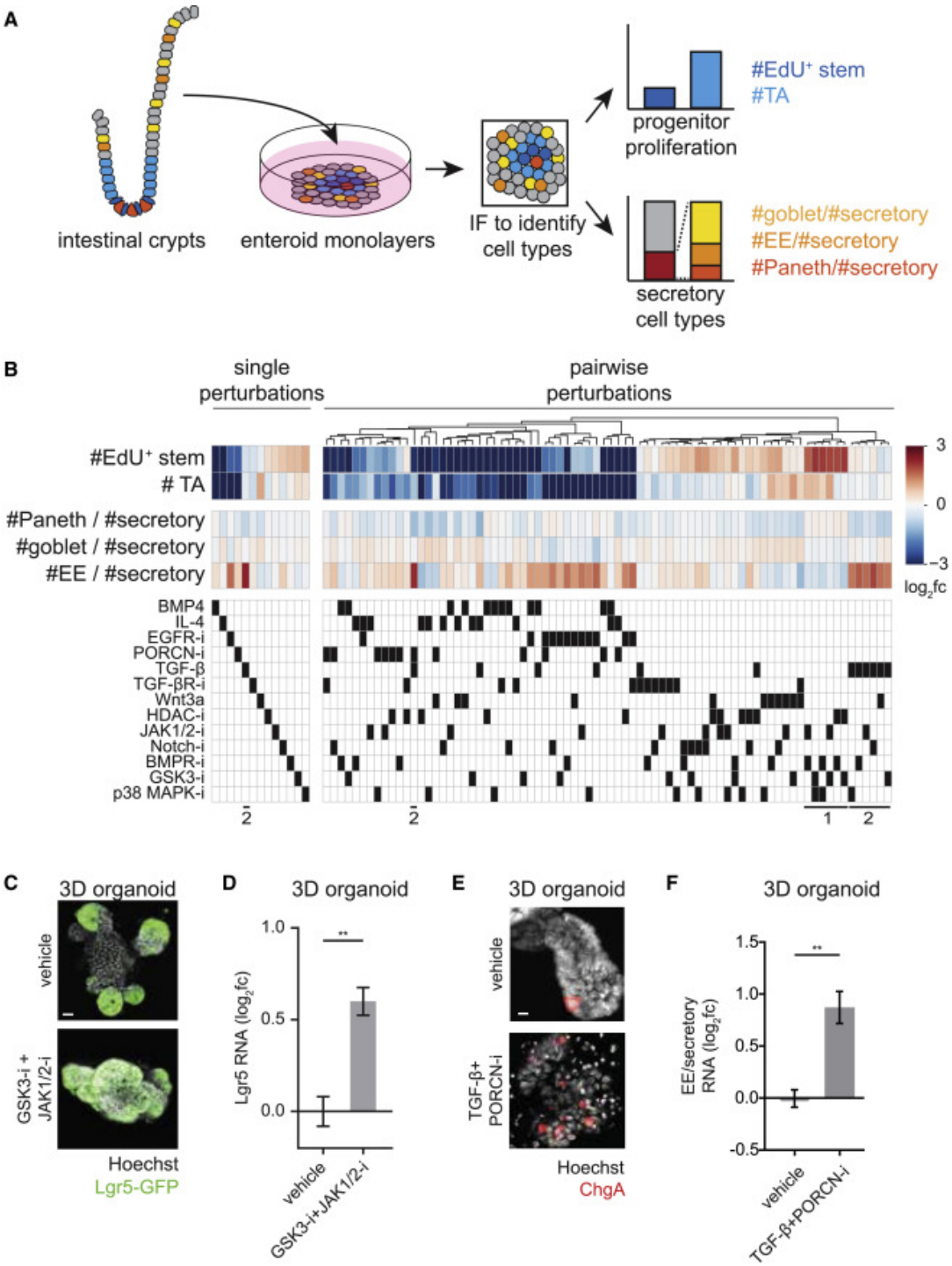

Figure 2.4: Systematic characterization of perturbation effects on intestinal epithelial cell-type composition reveals cell-type-specific regulators. (A) Schema for characterization of perturbation effects on cell-type composition within enteroid monolayers. (B) Heatmaps of single (left) and pairwise (right) perturbation effects to enteroid monolayers. Top: perturbation effects are represented as log2-fold change (fc) relative to vehicle-treated wells. Bottom: matrix of used perturbations. Single perturbations are sorted by #EdU+ stem cells; pairwise perturbations are clustered based on similarity of tissue-wide effects. Callouts (1) and (2) at

(caption continued from previous page) bottom are referred to in text. n = 28 (controls), 6–8 (single perturbations), or 2 (pairwise perturbations) wells. (C and D) Co-treatment of 3D organoids with GSK3-i + JAK1/2-i enriches for Lgr5+ stem cells. (C) Representative IF images of Lgr5-GFP-DTR 3D organoids show an increased proportion of cells expressing Lgr5 in GSK3-i + JAK1/2-i co-treatment (48 h). Scale bar, 15μm. (D) Lgr5 RNA levels measured by qRT-PCR are increased in 3D organoids co-treated with GSK3-i + JAK1/2-i for 48 h. n = 3 wells. Error bars, mean+/-SEM. (E and F) Co-treatment of 3D organoids with TGF-b + PORCN-i enriches for EE cells. (E) Representative IF images of 3D organoids show increased EE (ChgA+) cell numbers with TGF-b + PORCN-i co-treatment (24 h). Scale bar, 5μm. (F) qRT-PCR analysis of EE (ChgA) RNA relative to secretory (ChgA+Muc2+Lyz) RNA levels in 3D organoids treated with TGF-b + PORCN-i for 48 h. n = 3 wells. Error bars, mean+/- SEM. ** indicates p values < 0.01

et al., 2017; Yin et al., 2014) (Figure 2.3 E; Table 2.4) and were further confirmed at the RNA level using quantitative reverse transcriptase PCR (qRT-PCR) (Figure 2.3 F). However, most measurements obtained from our survey were previously uncharacterized, with several conditions strongly modulating different aspects of tissue composition (Table 2.5). Next, we highlight conditions that were previously unknown to enrich for stem or EE cells.

Pairwise combinations of inhibitors of GSK3, p38MAPK, BMPR, HDAC, and JAK1/2 (Figure 2.4 B, bottom callout 1; Figure 2.3 G) increased the number of Lgr5+ stem cells. Notably, these conditions caused similar, if not increased, enrichment for Lgr5+ stem cells compared with the current benchmark condition (GSK3-i + HDAC-i (Yin et al., 2014)). Lgr5+ stem-cell enrichment from these conditions was also observed at the RNA level, as indicated by qRT-PCR analysis of Lgr5 RNA in enteroid monolayers (Figure 2.3 H). We chose the pairwise combination of GSK3-i + JAK1/2-i to re-test in 3D organoids, as JAK1/2 had not been connected with stemness in the mammalian intestinal epithelium in the absence of inflammation (Richmond et al., 2018), and again observed enrichment of Lgr5+ stem cells (immunofluorescence and qRT-PCR; Figure 2.4 C,D).

The number of EE cells—relative to other secretory cell types—was also observed to increase under several conditions (Table 2.5). Notably, perturbations containing TGF-b generally

enriched for EE cells (Figure 2.4 B, bottom callout 2). The strongest inducer of EE cell fraction relative to secretory cells, TGF-b + PORCN-I co-treatment, was confirmed in 3D organoids (immunofluorescence and qRT-PCR; Figure 2.3 E,F; note that TGF-b treatment causes 3D organoids to decrease in size and lose their 3D architecture [Hahn et al., 2017]). To investigate possible signaling mechanisms for TGF-b enrichment of EE cells, we examined both canonical (SMAD2/3) and non-canonical (PI3K, mechanistic target of rapamycin kinase [mTOR], JNK) TGF-b downstream signaling components (Feng and Derynck, 2005; Massague, 1998; Zhang, 2009). Deletion of SMAD3, but not inhibition of non-canonical TGF-b signaling effectors, abrogated EE cell upregulation induced by TGF-b (Figure 2.3 I,J). This enrichment was accompanied by an increase in SMAD2/3 target gene expression, as demonstrated by RNA sequencing of 3D organoids (Figure 2.3 K). Thus, the EE enrichment by TGF-b that we identified in our survey occurs through canonical SMAD2/3 signaling.

Identification of a Mutually Antagonistic Signaling Interaction

Next, we searched for perturbation interactions that regulate cell-type composition (Figure 2.5 A,B). We recapitulated known interactions, such as between perturbations that modulate the same signaling pathway (e.g., the synergistic effect of Wnt3a + GSK3-i, Figure 2.5 C). We also identified unexpected interactions, particularly a mutual antagonism between IL-4 and EGFR-i in co-regulation of TA cell numbers. Individually, IL-4 or EGFR-i reduced the number of TA cells by ~4 or ~6 log-fold relative to control, respectively, while co-treatment reduced the number of TA cells by only ~1.5 log-fold relative to control (Figure 2.6 A). This effect was surprising, as IL-4 and EGFR-i are not known to interact. A similar result was also observed with the EGFR inhibitor, gefitinib, and the IL-4-related cytokine, IL-13, on proliferating cells (Figure 2.5 D,E), indicating the mutual antagonism is not due to off-target or perturbation-specific effects.

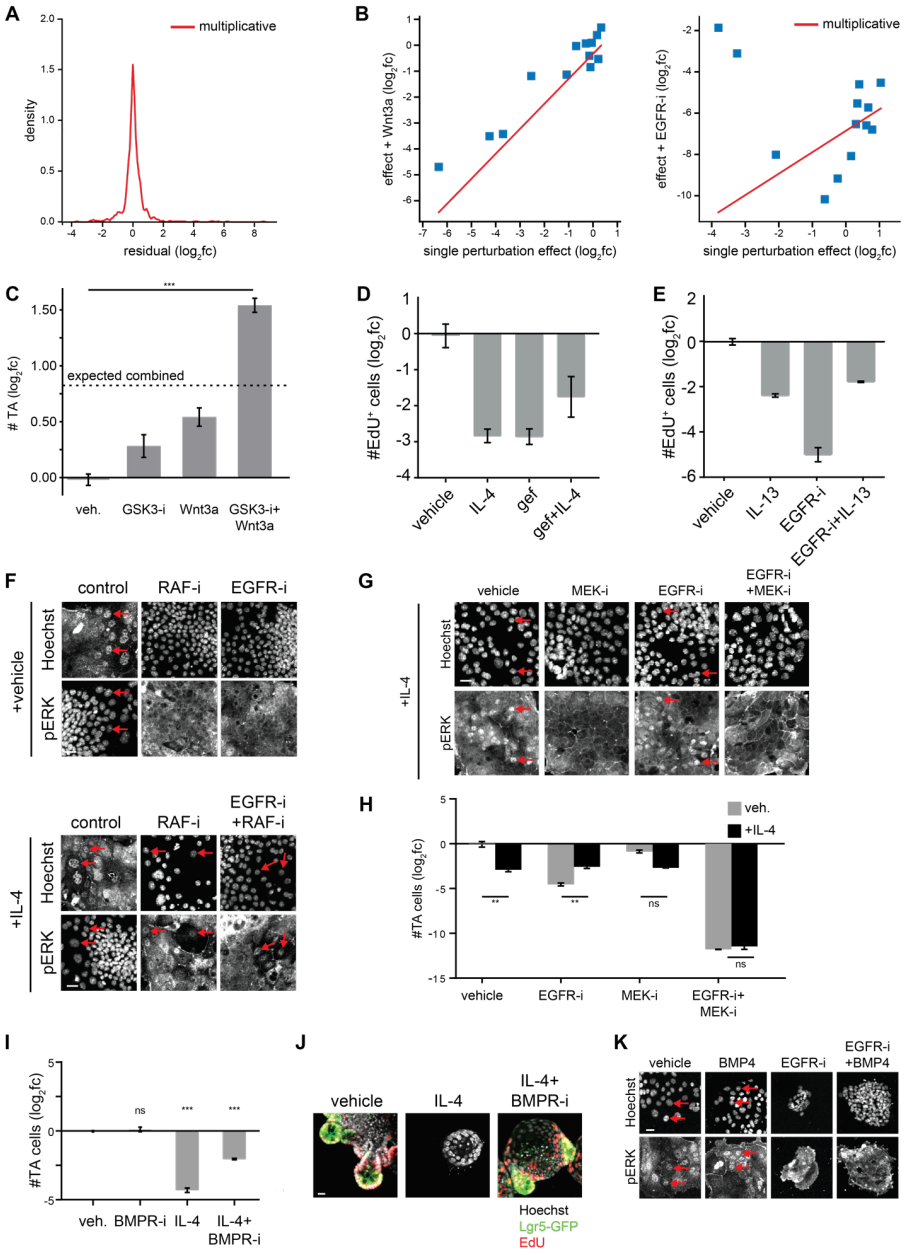

Figure 2.5: Evaluation of the multiplicative model and dissection of mutual antagonism between EGFR-i and IL-4. (A) Perturbation effects are generally similar to the predictions of the multiplicative model. Distribution of residual between predicted and observed values across all cell type readouts is shown. (B) Examples of well-predicted (Wnt3a) and divergent (EGFR-i) perturbations are shown. Effects shown are on #TA cells. (C) The combination effect of Wnt3a and GSK3-i is much higher (effect size > 2, $p<0.01$) than would be expected under the multiplicative model (dashed line). Error bars mean +/- SEM. n=28 (vehicle), 6 (GSK3-i and Wnt3a), or 2 (Wnt3a + GSK3-i) wells. (D) EGFR inhibitor gefitinib (gef) antagonizes the effect of IL-4 on #EdU+ cells. Error bars mean +/- SEM. n=2 for all conditions. (E) IL-13, a closely related cytokine to IL-4, antagonizes the effect of EGFR-i on #EdU+ cells. Error bars mean +/- SEM. n=2 for all conditions. (F) IL-4 bypasses RAF-i to activate ERK signaling. Enteroid

(caption continued from previous page) monolayers were treated with the indicated compounds for 48 hours and then stained for phospho-Erk1/2. Top: Both RAF-i and EGFR-i treatment inhibit Erk activation. Bottom: Co-treatment of IL-4 with either RAF-i or RAFi + EGFR-i rescues Erk activation (nuclear translocation of phospho-Erk). Red arrows indicate example cells with nuclear phospho-Erk. Scale bars 5μm. (G) MEK inhibition reduces Erk activation even in the context of IL-4 treatment. Enteroid monolayers were treated with the indicated compounds for 24 hours and then stained for phospho-Erk1/2. Red arrows indicate example cells with nuclear phospho-Erk. Scale bar 7.5μm.

How does IL-4 signaling antagonize EGFR inhibition? Prior work suggested that EGFR inhibition decreases proliferation by reducing MEK-Erk activity (Basak et al., 2017). We found that IL-4 treatment can activate Erk even in the context of inhibiting EGFR (Figure 2.6 B) or RAF (Figure 2.5 F). However, IL-4 could neither activate Erk (Figure 2.5 G) nor rescue TA cell numbers (Figure 2.5 H) in the context of inhibiting MEK, whether EGFR was inhibited or not. Together, this indicated that IL-4 antagonizes EGFR inhibition by activating MEK-Erk signaling downstream of the EGFR-Ras-Raf cascade and upstream of MEK.

How does EGFR inhibition antagonize IL-4? Prior work suggested that BMP2 (the epithelial paralog of mesenchymal BMP4) production could reduce TA cell numbers (He et al., 2004; Thorne et al., 2018). We found that IL-4 treatment of enteroid monolayers significantly increases BMP2 production (Figure 2.6 C). BMP receptor inhibition, while having no obvious effect on TA cell numbers on its own, rescued the IL-4-induced decrease in TA cell numbers in enteroid monolayers and 3D organoids (Figure 2.5 I,J). Finally, co-treatment of EGFR-i + IL-4 showed no significant change in production of BMP2 compared with control conditions (Figure 2.6 D). We note that EGFR-i and BMP did not interact through MEK-ERK signaling (Figure 2.5 K). Together, this indicated that EGFR inhibition antagonizes BMP2 production induced by IL-4 and thereby rescues the decrease in TA cells.

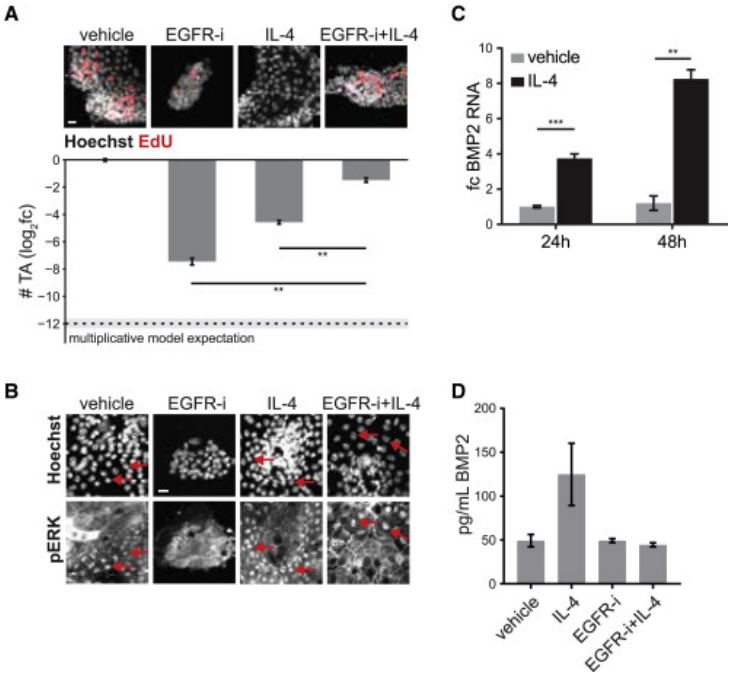

Figure 2.6: Interaction mapping reveals mutual antagonism between EGFR-i and IL-4 on TA cell numbers. (A) Example images (top) and quantification of TA cell numbers (bottom) in enteroid monolayers treated as indicated for 48 h. Co-treatment of IL-4 + EGFR-i strongly deviates from the multiplicative model of perturbation interaction (dashed line; effect size >5, $p < 0.0001$). Error bars, mean ± SEM. n = 28 (vehicle), 6 (EGFR-i), 8 (IL-4), or 2 (IL-4 + EGFR-i) wells. Scale bar, 10 µm. (B) Example images of phospho-Erk staining in enteroid monolayers treated as indicated for 48 h. Nuclear phospho-Erk is observed in all conditions except EGFR-i alone. Red arrows: example cells with nuclear phospho-Erk. Scale bar, 7.5 µm. (C) Enteroid monolayers were treated as indicated and BMP2 RNA levels were measured by qRT-PCR. Error bars, mean ± SEM. n = 3 (vehicle, 24 h), 3 (IL-4, 24 h), 3 (vehicle, 48 h), or 2 (IL-4, 48 h) wells. (D) Enteroid monolayers were treated as indicated for 48 h and levels of BMP2 in the media were measured by ELISA (EGFR−i+IL-4 versus control: ns). n = 2 wells. Error bars, mean ± SEM. ** indicates p values < 0.01; *** indicates p values < 0.001; ns: not significant

Decreasing TA Proliferation Increases the Ratio of Secretory to Absorptive Cells

A fundamental question in renewing tissues is how proliferation regulates differentiated cell-type composition. We searched across our diverse survey of perturbations for global trends between progenitor and secretory cell populations (Figure 2.7 A and Figure 2.8 A,B). Few correlations were observed, with one striking exception: TA cell numbers were anticorrelated with the fraction of differentiated (EdU^-) cells that express secretory markers (Figure 2.7 A). Further analysis showed that the EdU^- population was largely composed of secretory and absorptive

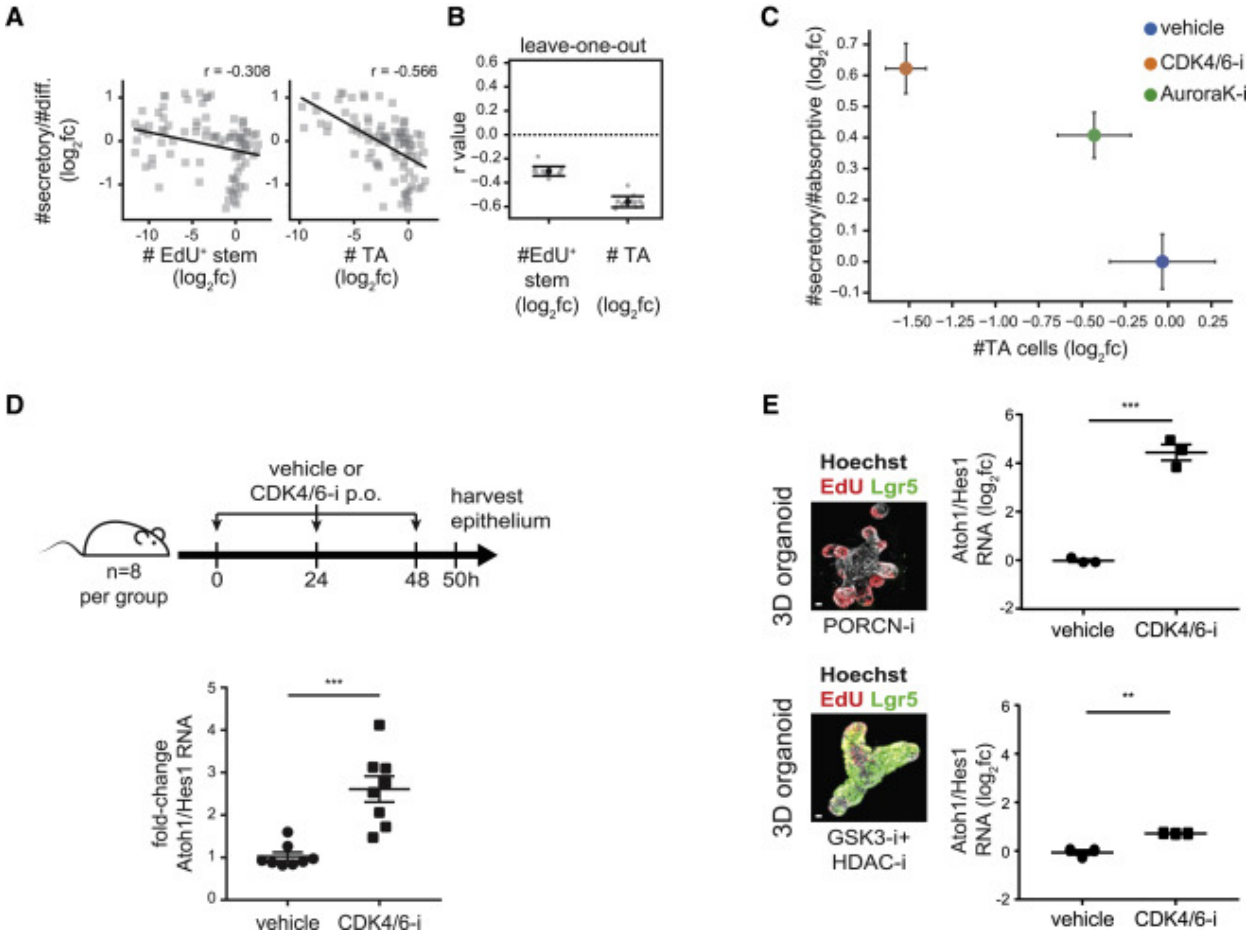

Figure 2.7: Inhibition of proliferation increases secretory cell prevalence in enteroid monolayers, in 3D organoids, and *in vivo*. (A) Numbers of TA cells but not EdU^+ stem cells correlate with secretory cell fractions. Perturbation effects (log_2fc) are plotted pairwise for each feature. R: correlation coefficient (r). Diff: $\#EdU^-$ cells. (B) The TA to secretory cell correlation is not driven by a specific perturbation. Each of the 13 perturbations was sequentially dropped from the dataset and correlation coefficients (r value) were calculated. Error bars, mean ± SD. (C) Inhibition of cell-cycle progression increases secretory cell fractions. Enteroid monolayers were treated as indicated for 48 h, after which #TA cells and #secretory/#absorptive cells were quantified. n = 3 wells. Error bars, mean ± SEM. (D) Impairing proliferation increases the secretory to absorptive (Atoh1:Hes1) ratio *in vivo*. Mice were treated with CDK4/6-i (palbociclib) or vehicle every 24 h for 48 h. At 50 h, intestinal crypts were harvested and gene expression was measured by qRT-PCR. n = 8 mice/group. Error bars, mean ± SEM. (E) TA cells alter secretory fractions in response to cell-cycle inhibitors. 3D organoids were enriched for stem (GSK3-i + HDAC-i) or TA (PORCN-i) cells, then treated with a CDK4/6 inhibitor (palbociclib) for 48 h. The secretory to absorptive (Atoh1:Hes1) ratio was measured by qRT-PCR. n = 3 wells. Scale bars, 10 μm. Error bars, mean ± SEM. ** indicates p values < 0.01; *** indicates p values < 0.001

(FABP1$^+$) cells (Figure 2.1 F and Figure 2.8 C-E), indicating that altering TA cell numbers may modulate the balance between secretory and absorptive cells. Importantly, this anticorrelation was not driven by any specific perturbation (Figure 2.7 B), suggesting that it reflects a tissue-intrinsic property.

We also observed this anticorrelation upon directly modulating proliferation using cell-cycle inhibitors in enteroid monolayers, 3D organoids, and *in vivo*. In enteroid monolayers, the cell-cycle inhibitors CDK4/6-i (palbociclib) and AuroraK-i (AT9283) decreased TA cell numbers (estimated using either EdU or Ki67 staining) and increased the secretory to absorptive ratio in a dose-dependent manner (Figure 2.7 C and Figure 2.8 E-J). We note that, while progenitor cell numbers were reduced under cell-cycle-inhibitor treatments, the tissue spatial organization into crypt-like foci and differentiated regions was maintained (Figure 2.8 E). To validate this correlation *in vivo*, mice (n = 8 per group) were treated with CDK4/6-i or vehicle. After 50 h of treatment, intestinal crypts were harvested and RNA levels of proliferative (Ki67), secretory (Atoh1), and absorptive (Hes1) cell markers were measured. Consistent with the enteroid monolayer experiment, CDK4/6-i treatment decreased proliferation (Figure 2.8 K) and increased the secretory to absorptive ratio (Figure 2.7 D). Finally, we used 3D organoids to test whether the anticorrelation is specific to TA cells but not stem cells. 3D organoid cultures, enriched for either stem or TA cells (Figure 2.7 E and Figure 2.8 L), were treated with CDK4/6-i. Strikingly, CDK4/6-i increased the secretory to absorptive ratio in 3D organoids enriched for TA cells ~10-fold more than in 3D organoids enriched for Lgr5$^+$ stem cells (Figure 2.7 E). Together, these results demonstrate that a decrease in TA proliferation causes the relative fraction of secretory to absorptive cells to increase in the intestinal epithelium.

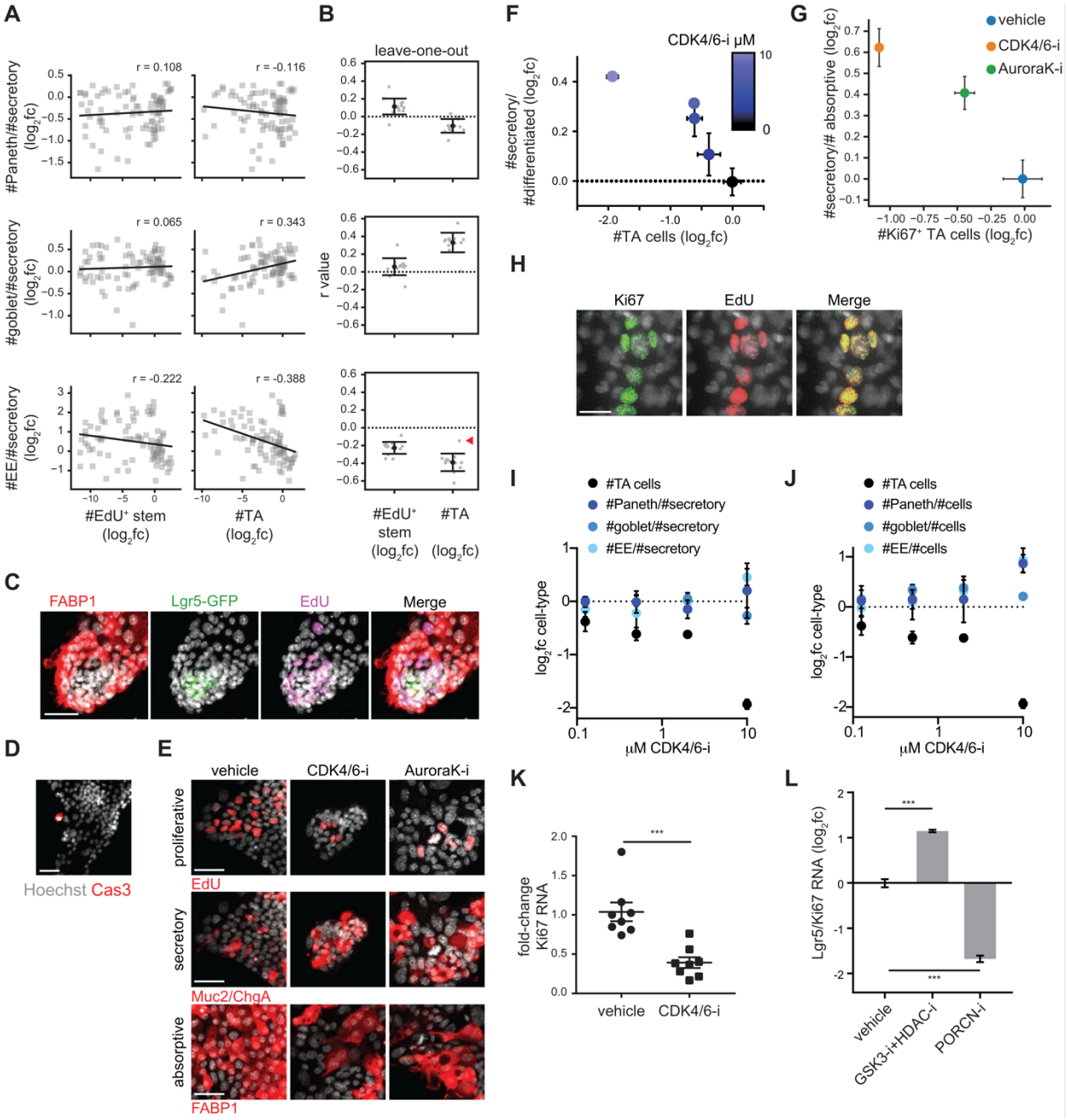

Figure 2.8: TA cell proliferation causes an anti-correlated change in secretory cell prevalence. (A) Numbers of TA cells anti-correlate with EE cell fractions. Perturbation effects (log2fc) are plotted pairwise for each feature. Correlation coefficient (r) as indicated. (B) Each of 13 perturbations was individually dropped from the dataset and correlation coefficients (r value) were calculated. Red arrowhead indicates loss of correlation between #TA cells and #EE/#secretory after dropping EGFR-i. Error bars mean +/- SD. (C) Enterocytes (FABP1) surround crypts, and do not colocalize with proliferative (EdU+) cells. Enteroid monolayers were cultured for 48 hours and then stained with indicated cell type markers. Scale bar 40 µm. (D) Few apoptotic cells are visualized in enteroid monolayers. Enteroid monolayers were cultured for 48 hours and then stained with Active-Caspase3 to visualize apoptotic cells. Scale bar 40 µm. (E) Effect of cell cycle inhibitors on the number of proliferative, secretory, and absorptive cells.

(caption continued from previous page) Enteroid monolayers were treated as indicated for 48 hours, and then proliferative (EdU+) cells, secretory (Muc2+ and ChgA+) cells, and absorptive (FABP1+) cells were visualized. Representative images are depicted. Scale bar 40 μm. (F) CDK4/6-i (palbociclib) increased the secretory cell fraction and decreased TA cell numbers in a dose-dependent manner. Increasing concentrations of CDK4/6-i were applied (concentrations indicated by color bar) to enteroid monolayers for 48 hours. Changes in the TA cells (#TA cells log2fc) and secretory cell prevalence amongst differentiated cells (#secretory/#differentiated log2fc) were quantified. The color of each point indicates the concentration of CDK4/6-i applied. Error bars mean +/- SEM. n=4 (0 μM CDK4/6-i) or 2 (all other concentrations) wells. (G) Inhibiting cell cycle progression increases secretory cell fractions. Enteroids were treated as indicated for 48 hours, after which #Ki67+ TA cells, and #secretory/#absorptive cells were quantified. n = 3 wells. Error bars mean +/- SEM.

Differential Amplification as a Model for Proliferation-Based Control of Tissue Composition

How does alteration of TA cell proliferation affect the abundance of secretory cells relative to absorptive cell types? Lineage structures have been modeled in the past, such as the branching of progenitors in enabling robust feedback control (Lander et al., 2009). Previous studies suggest that secretory progenitors are less proliferative compared with absorptive progenitors. In particular, commitment to a secretory fate (specifically expression of the Notch ligand Dll1) coincides with cell-cycle exit (Stamataki et al., 2011), and lineage tracing showed that secretory cell clones are on average smaller than absorptive cell clones (Bjerknes and Cheng, 1999).

We confirmed that secretory progenitors undergo fewer divisions—and thus have less amplification—than absorptive progenitors. An EdU dilution experiment in enteroid monolayers indicated that the overall population of intestinal epithelial cells was amplified more than the secretory cell types (Figure 2.9 A). Next, we made use of clonal lineage tracing experiments to investigate the observed differential amplification between absorptive and secretory progenitors. Enteroid monolayers from transgenic mice (Atoh1-CreER;R26R-tdTomato or Notch1-CreER;R26R-tdTomato) were treated with 4-hydroxytamoxifen for 24 h to induce sparse labeling of secretory (Atoh1^{+}) or absorptive (Notch1^{+}) clones (Figures 2.9 B,C). We observed

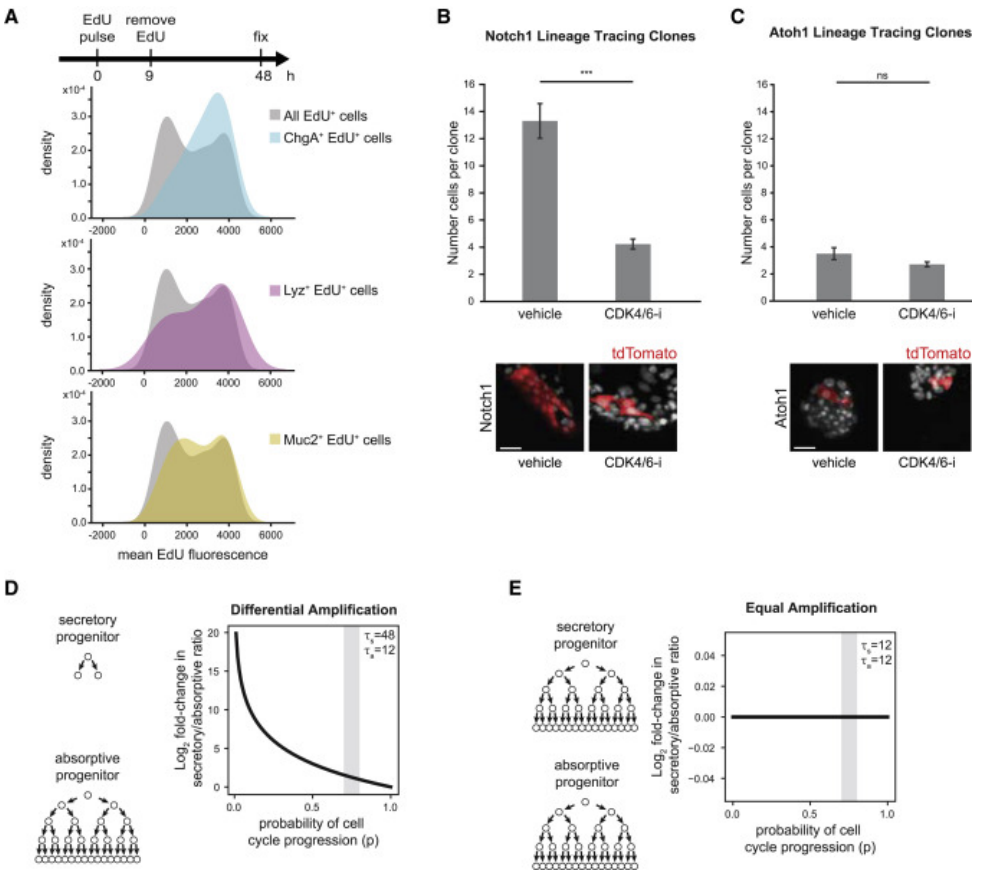

Figure 2.9: Differential amplification of secretory progenitors connects proliferation with differentiated cell-type composition. (A) Secretory progenitors divide fewer times than other progenitors. Top: enteroids were pulsed with EdU (0–9 h), then fixed and stained (at 48 h). Mean EdU signal intensity was quantified in all EdU$^+$ cells and in EdU$^+$ cells that also stained positive for markers of Paneth (Lyz), goblet (Muc2), and EE (ChgA) cells. Distribution of EdU intensities is represented as a kernel density plot. Cells with higher EdU intensity divided fewer times than those with lower EdU. (B and C) Enteroid monolayers were derived from (B) Notch1-CreER;R26R-tdTomato mice or (C) Atoh1-CreER;R26R-tdTomato mice. 4-hydroxytamoxifen was added to cultures for 24 h, followed by 48 h of vehicle or CDK4/6-i (palbociclib). CDK4/6-i reduced the average number of cells in absorptive (Notch1) clones but had little effect on the average number of cells in secretory (Atoh1) clones. Representative images of clones under *(caption continued from previous page)* vehicle or CDK4/6-i treatment are shown. Error bars, mean ± SEM. n = 78 (Notch1 vehicle), 74 (Notch1 CDK4/6-i), 30 (Atoh1 vehicle), or 38 (Atoh1 CDK4/6-i) clones. Scale bar, 50 μm. (D and E) Model output of secretory to absorptive differentiated cell ratio as a function of probability of cell cycling (p). Gray bands indicate experimentally observed range for parameter p. (D) Secretory progenitors divide fewer times than absorptive progenitors (τ_s = 48 h, τ_a = 12 h). Inhibition of the cell cycle (increasing p) increases the secretory to absorptive ratio. (E) Secretory progenitors divide the same number of times as absorptive progenitors (τ_s, τ_a = 12 h). Inhibition of the cell cycle (increasing p) does not change the secretory to absorptive ratio. *** indicates p values < 0.001; ns: not significant

that, on average, absorptive progenitors amplified 3.8-fold more than secretory progenitors (secretory: 3.5 cells per clone; absorptive: 13.3 cells per clone). This suggested that absorptive progenitors undergo ~2 more rounds of cell division than secretory progenitors. In contrast, Cdk4/6-i treatment caused absorptive progenitors to amplify only 1.6-fold more than secretory progenitors (secretory: 2.7 cells per clone; absorptive: 4.2 cells per clone). Thus, inhibition of proliferation impairs amplification of absorptive cells to a greater extent than secretory cells.

Finally, we mathematically modeled the lineage expansion process from TA to differentiated cells (Figure 2.9 D,E and Figure 2.10 A,B). A fit of parameters to the clonal lineage tracing data suggests that the effects of cell-cycle inhibitors on division probabilities were roughly the same for both lineages. Moreover, the model recapitulates the anticorrelation between proliferation and the ratio of secretory to absorptive cell types (Figures 2.9 D,E). In summary, differential amplification of TA progenitors in the intestinal epithelium provides a mechanism for controlling the secretory to absorptive bias through proliferation.

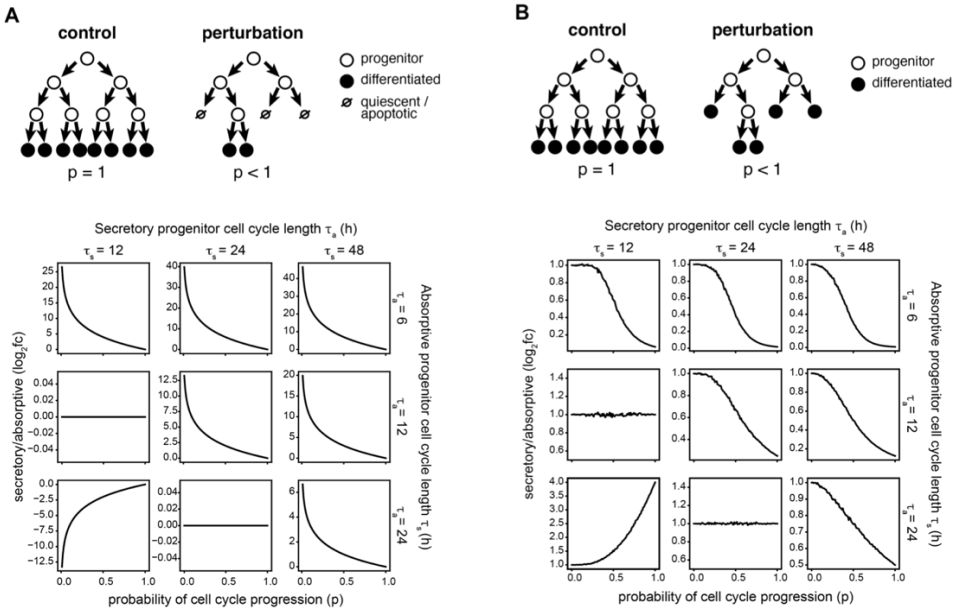

Figure 2.10: Cell cycle modulators affect the secretory to absorptive ratio due to differential amplification of secretory and absorptive progenitors. (A) Diagram and output of quiescence probability model (Model 0). (B) Diagram and output for the stochastic model in which TA cells differentiate upon quiescence (10000 runs, Model 2).

DISCUSSION

The intestinal epithelium is a constantly renewing tissue that maintains a precise cell-type composition throughout life. To investigate how signals combine to regulate tissue renewal, we conducted a systematic survey of single and paired perturbations on enteroid monolayers. Our survey revealed conditions that enrich for specific cell types, including $Lgr5^{+}$ stem cells (combinations of GSK3, p38MAPK, BMPR, HDAC, and JAK1/2 inhibitors) and EE cells (TGF-β ± PORCN-i). These results highlight potential convergent effects of these pathways in regulating stemness and EE cell maturation, respectively. We also identified perturbations that have unexpected combined effects on tissue growth, including an unexpected mutual antagonism between IL-4 and EGFR-i that regulated the TA cell population. Investigation of this antagonism led us to identify functions of IL-4, namely its ability to bypass an EGFR blockade and to induce BMP production.

Our survey further suggested a general anticorrelation between progenitor cell proliferation and the ratio of secretory to absorptive cells (observed in enteroid monolayers, 3D organoids, and *in vivo*). We found fewer rounds of cell division for secretory than absorptive progenitors and that this difference was diminished under cell-cycle inhibition (observed in enteroid monolayer in both EdU-dilution and lineage-tracing studies), leading to an increase in the ratio of differentiated secretory cells to absorptive cells. These results suggest a "differential amplification model" by which modulation of TA cell proliferation (such as during times of injury, infection, or calorie restriction) can control tissue-cell-type composition (Koch and Nusrat, 2012; Yilmaz et al., 2012).

A limitation of our current study is that we did not take into account the spatial arrangements or dynamics of TA cell spatial localization in the niche. Future studies will be

needed to dissect the interplay among TA cell location, microenvironmental signals, and amplification. Furthermore, while our study identified and focused on differential amplification, probabilistic fate decisions from stem cells also play a role in controlling cell-type composition (Balázsi et al., 2011). It will be interesting in future studies to identify how these two mechanisms co-exist and whether they play different roles in homeostatic control of tissue.

Our study points to a crucial and overlooked role for TA cells in guiding tissue function. TA cells can coordinate tissue responses to changing microenvironments (e.g., worm infections; Birchenough et al., 2016) and thereby insulate stem cells from extreme, transient changes. TA cell intermediates between stem and differentiated cell populations are present in numerous organs, including skin and the hematopoietic system, and differential amplification may play a general role in the regulation of cell-type composition.

METHODS

Mice

All animal care and experimentation was conducted under protocol AN-179937 agreed upon by the Administrative Panel on Laboratory Animal Care at the University of California, San Francisco. All our animal studies are performed in full accordance with UCSF Institutional Animal Care and Use Committee (IACUC). 5- to 6-week-old male C57BL/6 mice (C57BL/6NHsd) were purchased from Envigo. Lgr5$^{eGFP\text{-}DTR}$ mice were a kind gift from Frederic de Sauvage, Genentech under MTA #OM-216813 (Tian et al., 2011). Intestinal epithelium-specific SMAD3 null mice (SMAD3 fl/fl;Villin-Cre/wt) were generated by crossing SMAD3 fl/fl mice (kind gift from Tamara Alliston) with Villin-Cre mice. Secretory and absorptive progenitor cell labeled enteroid monolayers were generated from Atoh1-CreER;R26R-tdTomato

and Notch1-CreER;R26R-tdTomato mice, respectively. Mice were housed with ad libitum food and water on a 12 hour light cycle at the UCSF Preclinical Therapeutics Core vivarium.

Enteroid Monolayer Cultures

Enteroid monolayers were derived as previously described (Thorne et al., 2018; Sanman et al., 2020). Briefly, jejunum was isolated from male mice between 6-12 weeks of age. Mice used were either from the C57BL/6 strain or, when indicated, the $Lgr5^{eGFP\text{-}DTR}$ strain. Epithelium was released from jejunal tissue by incubation in ice-cold PBS with 3 mM EDTA in PBS (Ambion #9260). Released epithelial tissue was washed 3x with OBM, after which crypts were separated from villus material using 100 and 70 μm cell strainers (BD Falcon) in succession. Crypts were resuspended in seeding media and plated on Matrigel (Thermo Fisher #CB-40234C)-coated 96-well optical bottom plates (BD Biosciences #353219 and Greiner #655090). Typically, 300 crypts were seeded per well. We identified this seeding density because, at this density, we did not observe an effect of variations in initial confluency on cell outgrowth (#cells) or cell type composition (Figure 2.1 G). Four hours after seeding, cells were washed with OBM and incubated in control media containing other perturbations of interest. At the 48 h time point, ~30,000-40,000 cells were typically observed per well under control conditions.

3D Organoid Cultures

3D organoids were cultured as previously described (Sato et al., 2009). Organoids were derived from male mice between 6-12 weeks of age. Mice used were either from the C57BL/6 strain or, when indicated, the $Lgr5^{eGFP\text{-}DTR}$ strain. For imaging experiments, 3D organoids were seeded in 10 μL of Matrigel in 96-well optical bottom plates.

Media

Organoid basal media (OBM) consists of Advanced DMEM/F12 with non-essential amino acids and sodium pyruvate (Fisher Scientific #12634-028) containing 1x N-2 (Fisher Scientific #17502-048), 1x B-27 (Invitrogen #17504-044), 10 mM HEPES (Invitrogen #15630080), 1x GlutaMAX (Invitrogen #35050-061), 1 μM N-acetylcysteine (Sigma Aldrich #A9165), 100 U/mL penicillin and 100 μg/mL streptomycin (Corning #30-002).

For initial seeding, enteroid monolayers were maintained in OBM supplemented with 3 μM CHIR-99021 (Sigma Aldrich #SML1046), 50 ng/mL murine EGF (Invitrogen #PMG8043), 1 μM LDN-193189 (Sigma Aldrich #SML0559), 500 ng/mL murine R-spondin-1 (Peprotech #315-32), and 10 μM Y-27632 (Selleck Chemicals #S1049).

4 hours after initial seeding, media was changed into OBM supplemented with 50 ng/mL murine EGF, 100 ng/mL murine Noggin, and 500 ng/mL murine R-spondin-1. Perturbations applied in the studies described here were all applied in the background of this medium.

Growth Factors and Chemical Compounds

All growth factors and chemical compounds were purchased from suppliers and used as designated without further purification. Unless otherwise indicated, perturbations were used as listed in Table 2.6.

CDK4/6-i administration to mice and tissue harvest

To test the effects of cell cycle inhibition on the secretory to absorptive ratio, palbociclib (LC Laboratories #P-7744) at 150 mg/kg in 50 mM sodium lactate buffer pH 4.4 was administered to mice by oral gavage every 24 hours for 48 hours (at 0 hours, 24 hours, and 48 hours). At 50 hours, the small intestine was harvested, and intestinal crypts were harvested as described in the

enteroid monolayer culture section above. Crypts were lysed in Buffer RLT (RNEasy Kit, Qiagen) for subsequent RNA purification.

3D Organoid Enrichment for Stem and TA Cells

3D organoid cultures were enriched for stem cells by treating with GSK3-i + HDAC-i for 48 hours (Yin et al., 2014). 3D organoid cultures were enriched for TA cells by treatment with PORCN-i for 24 hours.

Immunofluorescence Assay

Enteroid Monolayer

Enteroid monolayers were washed 1x with warm D-PBS and then fixed with 4% paraformaldehyde in PBS for 15 minutes at room temperature. Cells were then washed with PBS and permeabilized with 0.5% Triton-X-100 in PBS at room temperature for 10 minutes. Cells were washed, blocked with 3% BSA in PBS for 30 minutes, and then incubated in primary antibody in antibody buffer (PBS with 0.3% Triton-X-100, 1% BSA) overnight at 4C. The next day, cells were washed and incubated with secondary antibodies and Hoechst 33342 (5 μg/mL; Invitrogen #H3570) in antibody buffer for 2 hours at room temperature. After this, cells were washed with PBS and imaged in TBS-T (0.1% Tween in 1x TBS pH 7.4).

3D Organoids

Media was carefully aspirated from around Matrigel domes containing 3D organoids using a P100 pipette. 4% paraformaldehyde in PBS was immediately added for 15 minutes at room temperature. Cells were then washed 2x with PBS and permeabilized using 0.5% Triton-X-100 in PBS for 20 minutes at room temperature. Cells were then rinsed 3x10 minutes with 100 mM glycine in PBS with gentle agitation. Cells were blocked in 3% BSA in PBS for 40 minutes and then incubated with primary antibody in antibody buffer overnight at room temperature. The next

day, cells were washed 3x20 minutes in antibody buffer and then incubated with fluorescent secondary antibodies and Hoechst in antibody solution for 1 hour at room temperature. Cells were then rinsed in PBS and stored and imaged in TBS-T.

Antibodies

All antibodies were purchased from suppliers and used as designated without further purification. Unless otherwise indicated, antibodies were used as indicated in Table 2.7.

EdU Pulse and Visualization

To visualize proliferating cells (specifically, those in S phase), enteroid monolayers were incubated with 10 μM EdU (Thermo Fisher #A10044) in media (containing indicated perturbations or vehicle) for 2 hours prior to fixation. After immunofluorescence staining, EdU^+ cells were visualized using Click chemistry as previously described (Salic and Mitchison, 2008). Briefly, cells were incubated with a reaction mixture containing 1 mM $CuSO_4$ (VWR International #470300-880), 5 μM sulfo-Cyanine5 azide (Lumiprobe #B3330) or 5 μM BDP-FL azide (Lumiprobe #11430), and 100 mM sodium ascorbate (Sigma Aldrich #A4034) in PBS for 30 minutes at room temperature.

EdU Dilution Experiment

An EdU pulse was administered for the first 9 hours of culture (less than one TA cell cycle length (Matsu-Ura et al., 2016)), followed by a chase of 39 hours. EdU is initially incorporated into proliferating cells and then subsequently diluted with each cell division. Thus, EdU intensity in differentiated cells serves as a proxy for division number. Cells were fixed and stained for secretory cell markers Lyz, Muc2, and ChgA as well as EdU.

RNA Sequencing

RNA was harvested using an RNEasy Plus Mini Kit (Qiagen) according to manufacturer's instructions. Libraries were prepared using a QuantSeq 3' mRNA-Seq Library Prep Kit FWD for Illumina. Samples were quantified by Qubit prior to pooling and library size and integrity confirmed by Agilent Bioanalyzer with the high-sensitivity DNA kit. RNA sequencing was performed using 50 bp single-end sequencing on the Illumina HiSeq 4000 in the UCSF Center for Advanced Technology. A PhiX control library was used as an in-run control, spiked in at 5%.

BMP2 ELISA

Supernatant levels of BMP2 were quantified using a BMP-2 Quantikine ELISA kit (R&D Systems #DBP200), without significant deviations from manufacturer's instructions. We note that the measured concentration may be lower than the actual concentration due to the presence of Noggin, which binds BMP, in the culture media.

qRT-PCR

RNA was harvested from enteroid monolayers using an RNEasy Plus Mini Kit (Qiagen #74136). Reverse transcription was performed using iScript Reverse Transcription kit (Bio-Rad #1708841). Quantitative PCR was performed using SsoAdvanced Universal SYBR Green Supermix (Bio-Rad #1725272) on a BioRad CFXConnect. RNA levels were determined using the primers listed in Table 2.8.

Automated Brightfield Microscopy

Upon initial plating, enteroid monolayers were imaged in the brightfield channel using the 10x objective of a Nikon TE200-E epifluorescence microscope. These data were used as a control to determine whether enteroid monolayers were seeded at an optimal and consistent confluency.

Automated Confocal Microscopy

Enteroid monolayers were imaged on the 10x objective of a Nikon A1 confocal with Ti2-E microscope. The area of each well was covered by 24 individual scans. In each field of view, 4-8 z planes were collected at 1024x1024 resolution. Importantly, the nuclear stain was used to autofocus in each new field of view. Images in the paper are maximum projection images.

Lineage Tracing

Enteroid monolayers were derived from Atoh1-CreER;R26R-tdTomato and Notch1-CreER;R26R-tdTomato mice. After initial plating in 96-well imaging plates, 4-hydroxytamoxifen (Sigma) was added to cultures for 24 hours. After this, 4-hydroxytamoxifen was removed and vehicle or cell cycle inhibitors were added. Enteroid monolayers were cultured for a further 48 hours after which cultures were fixed and stained with Hoechst. The Atoh1 enteroid monolayers were imaged on an Operetta CLS High Content Imaging System (Perkin Elmer) at 20x resolution; the area of each well was covered by 61 individual scans and four z-planes were collected for each field of view. The Notch1 enteroid monolayers were imaged on the Nikon A1 confocal with Ti2-E microscope as described above (Automated confocal microscopy; images of Notch1 enteroids shown in Figure 2.9 were imaged on the Operetta).

Quantification and Statistical Analysis

Quantifying % Confluency

% Confluency (percent of image which is occupied by enteroid monolayer cultures) was quantified from brightfield images using a previously reported algorithm (CellularRegionsFromBrightField function in Supplementary Software 1 from reference (Ramirez et al., 2016)).

Immunofluorescence Image Segmentation and Analysis

Image segmentation was performed using a custom Python analysis pipeline. Starting with maximum intensity projections of Hoechst, EdU, Lgr5-GFP, Muc2, Lyz, and ChgA fluorescent images, we segmented and then quantified numbers of nuclei, EdU^+ cells, stem cells, goblet cells, Paneth cells, and enteroendocrine cells, respectively. The general segmentation process for each object type consisted of two major steps: a thresholding step to identify image foreground, and a segmentation step to generate location and boundary of objects. Specific details are detailed below.

Segmenting Nuclei and EdU^+ Nuclei: Hoechst stain (for nuclei) or EdU (for EdU^+ nuclei) images were smoothed through convolution with a bilateral filter. The foreground was identified using a modified Otsu threshold method. Sparse nuclei were first segmented using a multi-scale Laplacian of Gaussian (LoG) detector followed by watershed algorithm. Clumps of nuclei in the sparse segmentation were detected based object size and shape irregularity thresholds. The clumps were then further segmented using a differently parameterized LoG detector followed by watershed (also see Figure 2.1 C).

Segmenting Stem Cells: Lgr5-GFP stain images were processed to remove tissue background and thresholded to identify crypt regions. Holes and gaps in crypt regions were filled using morphological operations and small objects (typically $Lgr5^+/Dclk1^+$ cells, see Figure 2.1 E) were dropped. Nuclei within crypt regions not associated with Paneth cells were segmented as stem cells (Figure 2.1 A).

Segmenting Goblet Cells: Mucin-2 (Muc2) stain images were smoothed by convolution with a median filter. Foreground was identified using a convex hull of objects in each Otsu-thresholded

Muc2 immunofluorescence image. Goblet cells were segmented using a LoG detector to generate markers of goblet object locations followed by watershed to create object boundaries.

Segmenting Paneth Cells: Lysozyme (Lyz) immunofluorescence images were smoothed through convolution with a bilateral filter then a tophat filter. Foreground was identified using the Otsu-thresholded Lyz immunofluorescence image. A LoG detector was then used to generate markers of Paneth object locations.

Segmenting Enteroendocrine (EE) Cells: ChgA stain images were processed using the same steps as Paneth cell identification, only with different parameters.

Quantifying Lgr5-GFP Intensity

Lgr5-GFP stain images were max projected. Mean intensities were quantified in nuclear segmentation, which captures cytoplasmic and membrane staining present across z-stacks in the segmentation regions.

Evaluation of Image Segmentation

Each cell type object (e.g., each nucleus, each goblet cell, each Paneth cell) was identified in raw immunofluorescence images by hand by an expert and, in parallel, using the customized algorithms described above. The expert-generated segmented images (where each mask represents an individual object) were compared to algorithm-generated segmented images to determine algorithm performance. 'Precision' was quantified by dividing the number of true positives (expert-identified objects also identified by the algorithm) by the number of total positives (all algorithm-identified objects). 'Recall' was quantified by dividing the number of true positives by the total number of expert-identified objects. F1 scores were calculated as the harmonic mean of precision and recall. See Table 2.1 for results.

Lineage Tracing Clone Analysis

For analysis we made use of the following images: Notch1 - 2 conditions (control, palbociclib) x 72 images; Atoh1 - 2 conditions (control, palbociclib) x 61 images. Clones were identified as regions of continuous staining with > 1 cell. The number of nuclei in each clone was counted manually.

RNA Expression Analysis

RNA reads were mapped and counted using the Integrated QuantSeq data analysis pipeline on BlueBee (BlueBee, now Illumina). One sample (one replicate of TGF-β + PORCN-i treatment) was removed from downstream analysis due to small library size and not passing other QC metrics. Filtering and normalization was performed using edgeR. Camera gene set enrichment analysis (camera function in R) was performed to assess significance of gene set changes under TGF-β and TGF-β + PORCN-i treatments.

Extracting Numbers of Each Cell Type

The numbers of EdU^+, stem, goblet, Paneth, and EE cells were quantified from respective cell type segmentation masks. The number of EdU^+ stem cells was quantified from the combination of EdU^+ and stem cell segmentations. The number of TA cells was quantified as #EdU^+ cells minus #EdU^+ stem cells. The number of EdU^- cells were used to approximate the number of differentiated (#diff.) cells. The number of enterocytes was quantified as the number of cells with mean FABP1 intensity above the Youden index (EdU^+ vs EdU^- cells). The number of $Ki67^+$ cells was quantified as the number of cells with mean Ki67 intensity above the Otsu threshold. The number of $Ki67^+$ TA cells was quantified as #$Ki67^+$ cells minus # $Ki67^+$stem cells. Due to limitations of conventional fluorescence microscopy, the number of secretory cells was

quantified by combining goblet, Paneth, and EE cell numbers from two stain sets (Hoechst, EdU, Lgr5-GFP, Lyz; Hoechst, EdU, Muc2, ChgA).

Replicates and Error Estimation

In-plate replicate control wells (2-6 wells per plate) were used to estimate mean and error. For replicate plates, mean and error were pooled. For across stain-set readouts, error was propagated.

Fold Change

We calculated fold-change effects relative to in-plate controls for readouts within each stain set (#EdU^+ stem cell, #TA cells). Fold-changes for readouts calculated across both stain sets (#goblet/#secretory, #Paneth/#secretory, #EE/#secretory) were calculated to a pooled control baseline measurement.

Statistical Testing

To compare samples, two-sided Student's t tests were used if equality of variance can be confirmed (Levene's test). Otherwise, two-sided Welch's t-tests were used.

Perturbation Effect Visualization

For Figure 2.4 B, double perturbation phenotypes were sorted into similar phenotypes using hierarchical clustering (clustermap function in seaborn) with a euclidean distance metric. Single perturbation phenotypes were sorted based on the number of EdU^+ stem cells in each row.

Distribution Visualization

For Figure 2.1 E and Figure 2.9 A, distributions were visualized as kernel density estimation plots.

Identifying Perturbation Interactions

1) Multiplicative Model

Under a conventional multiplicative model (van Hasselt and Iyengar, 2019; Mani et al., 2008), perturbations that do not interact combine as the multiplicative (or log-additive) of the individual perturbations:

$$log_2fc(AB_{pred}) = log_2fc(A_{obs}) + log_2fc(B_{obs})$$

For our analysis, features with a count of 0 are assigned a pseudocount of 1.

2) Effect Size

The deviation of each combinatorial perturbation from the prediction of the multiplicative model is quantified using effect size (Cohen's d):

$$effect\ size = \frac{|\mu_{obs} - \mu_{pred}|}{\sigma_{pooled}}$$

Where μ_{obs} and μ_{pred} are the observed and predicted means for the combination effect and σ_{pooled} is the pooled standard deviation from $\sigma_{obs}$and σ_{pred}.

Cell Type Correlations

1) Leave-One-Out

Perturbations were dropped one at a time from the dataset (dropping all single and pairwise conditions containing the perturbation) and correlations were re-calculated for each data subset (Figure 2.7 B and 2.8 B).

2) Population Growth Model and Variants

In our modeling of differentiated tissue from initial TA cell populations, we assumed: 1) stem cells give rise to TA cells, which are either secretory or absorptive progenitors; 2) the initial ratio

of absorptive to secretory TA progenitors produced by stem cells is equal; and 3) the progenitors are locked into either secretory or absorptive fates after the initial commitment, an assumption supported by previous studies (van Es et al., 2012; Stamataki et al., 2011). Further, we did not consider the effects of dedifferentiation as we are focused on the initial 48 h response to perturbation and dedifferentiation occurs over a longer period of time (Murata et al., 2020). The model describes the theoretical output of differentiated cells from populations of initial secretory or absorptive TA progenitors.

Control Conditions

Under normal growth (control condition), the number of absorptive, A, and secretory, S, cells generated from an initial number of absorptive, A_0, and secretory, S_0, TA progenitors is given by:

$$A = A_0(2)^{\frac{T}{\tau a}}$$

$$S = S_0(2)^{\frac{T}{\tau s}}$$

Here, T is the total model time, set to be 48 hours. By assumption (2) above, $A_0 = S_0$. Finally, t_a and t_s are the cell cycle lengths of absorptive and secretory progenitors, respectively. From past studies, absorptive progenitors are generally found to divide 4-5 times while secretory progenitors only divide 1-2 times (van Es et al., 2012; Potten, 1998; Stamataki et al., 2011). In line with these studies, we found from our lineage tracing experiments that absorptive progenitors divide around 4 times while secretory progenitors divide around 2 times. This corresponds to t_a and t_s values of around 12 and 24 hours in control conditions (Figure 2.9 D,E). Progenitors that divide fewer times are not considered differentiated cells.

Cell Cycle Inhibition Conditions

We next consider the effects of cell cycle inhibition. This can be connected to the exponential growth model in a number of ways (Table 2.9). Transformations of parameters that relate these models are given in (Table 2.9, column 4).

Model 0: In this model, cell cycle inhibitor drugs change the probability p that progenitor cells continue to cell cycle ($0< p< 1$ in the case of cell cycle inhibition conditions, or $p = 1$ in the control condition). Cell cycle arrested progenitors prematurely stop dividing (e.g., become quiescent or die) and do not contribute to the final differentiated lineages A or S.

In this stochastic implementation, the expected numbers of differentiated absorptive and secretory cells is determined by averaging over an ensemble of initial progenitor populations. The expectation follows from the observation that the expected number of direct progeny at each generation from a TA cell is $2p$ regardless of the generation. More explicitly, if we let X_i be the number of cells in generation i, then $X_{i+1} = 2pX_i$, and the expectation is given as $E(X_{i+1}) = 2pE(X_i)$. Starting from a single initial progenitor, the expected number of progeny at time T is:

$$E(X) = (2p)^{\#divisions} = (2p)^{\frac{T}{\tau}}$$

The final secretory to absorptive ratio in the differentiated population is given as:

$$f(p) = \frac{S}{A} = 2p^{\left(\frac{T}{\tau a} - \frac{T}{\tau s}\right)}$$

Since $f'(p)$ is always negative if $t_s > t_a$, inhibiting proliferation (increasing p) corresponds to an increase in secretory to absorptive ratio whenever secretory progenitors divide fewer times than absorptive progenitors.

We estimated the values of p for absorptive and secretory progenitors based on experimental data (Figure 2.9 B,C). In the clonal lineage tracing experiment ($A_0 = S_0 = 1$), we quantified the average absorptive (Notch1) and secretory (Atoh1) clone size ($E(A) = 13.31$, $E(S) = 3.50$) under control ($p = 1$) to obtain number of divisions ($T/t_a = 3.73$; $T/t_s = 1.81$). We additionally quantified the average clones sizes under cell cycle inhibition ($E(A) = 4.23$; $E(S) = 2.71$) to estimate $p = 0.736 \pm 0.0231$ for absorptive progenitors and $p = 0.868 \pm 0.0658$ for secretory progenitors (bootstrapped error). This parameter range is highlighted in Figure 2.9 D,E.

Model 1: In the first model variant, based on Lander et al. (2009), the cell cycle inhibitor drug deterministically affects the probability p_1 of cell cycling. ($0 < p_1 < 1$ in the case of cell cycle inhibition condition and $1 - p_1$ in the control condition.) This model can be related to the expectation of Model 0 through a change of parameters (Table 2.9, column 4). Since the derivative of the transformation function is positive, the output of Model 1 shares the same sign of change as the output of Model 0.

Model 2: In the second model variant, we consider the alternative mechanism that the cell cycle inhibitors lengthen the cell cycle duration. This deterministic model is parametrized by c, a cell cycle lengthening factor ($c > 1$ in the case of cell cycle inhibition conditions and $c = 1$ in the untreated condition). In this variant, we do not lose progenitors to quiescence and all progenitors are considered differentiated at the end of the experiment time T. Here, inhibiting proliferation (increasing c) also corresponds to an increase in secretory to absorptive ratio whenever secretory progenitors divide fewer times than absorptive progenitors.

Model 3: In the third model variant, we consider the possibility that progenitor cells differentiate when they are cell cycle arrested. In the previous model variants, cell cycle arrested progenitor cells were not included in final counts as they were neither proliferative nor

differentiated. Here, we modified the first stochastic model such that cell cycle arrested progenitor cells become differentiated cells of the same lineage, thus contributing to the final progeny size. The simulation output for this model variant produces the same trend as Model 0.

Taken together, these models consider three alternative mechanisms for cell cycle. All model behavior trends were consistent with

the experimental observation.

qRT-PCR Measurements

Test gene values were normalized to β-actin values. To quantify the Atoh1/Hes1 ratio, both Atoh1 and Hes1 fold-changes relative to control were calculated and then the Atoh1 fold-change was divided by the Hes1 fold-change.

TABLES

Table 2.1: Evaluation of the performance of cell type identification algorithms.

Cell type	Marker	Precision	Recall	F1 Score
nuclei	Hoechst	0.9965	0.9936	0.9951
goblet cells	Muc2	1	0.8998	0.9473
EE cells	ChgA	0.8551	0.9248	0.8886
Paneth cells	Lyz	0.9018	0.9642	0.9319
EdU^+ cells	EdU	1	0.9557	0.9774
crypt regions	Lgr5-GFP	0.9816	0.9877	0.9846
stem cells	Lgr5-GFP	0.9724	0.9756	0.9740
$Lgr5^+/Dclk1^+$ cells	Lgr5-GFP	0.8208	0.9087	0.8625

Table 2.2: Comparison of enteroid monolayer cell type composition with literature reports of small intestine cell type composition.

Cell Type	*In Vivo* (%)	Enteroid Monolayer (% of all cells)
Paneth	7.5% of crypt cells(Cheng and Leblond, 1974b)	3.1
Goblet	4-6% (Cheng and Leblond, 1974b)	3.8
EE	0.6% (Cheng and Leblond, 1974b)	0.4
Enterocyte	86% (Cheng and Leblond, 1974b)	63.3

Table 2.3: Enteroid monolayer differentiated cell type composition after culture establishment (4 hours after seeding).

Cell Type	Enteroid Monolayer (%)
Paneth	1.5
Goblet	6.1
EE	3.0
Enterocyte	5.0

Table 2.4: Selection of cell type perturbations for study. For each perturbation, the specific pathway and target are indicated, as is the expected effect on the pathway and tissue. Designation is the code with which the perturbation is referred to in figures and text.

Pathway	Perturbation	Target	Designation	Pathway Effect	Published Effect(s) on Intestinal Epithelium	Dose Ref.
EGFR	erlotinib	EGFR	EGFR-i	inhibit	Reduced proliferation, increased EE cell (Basak et al., 2017)	(Basak et al., 2017a)
Wnt	Wnt3a	Frizzled	Wnt3a	activate	Increased proliferation (Clevers, 2013)	(Thorne et al., 2018)
	IWP-2	PORCN	PORCN-i	inhibit	Decreased proliferation, stem cells, Paneth cells (Basak et al., 2017; van Es et al., 2005; Farin et al., 2016; Rodríguez-Colman et al., 2017)	(Yin et al., 2014)
	CHIR99021	GSK3	GSK3-i	activate	Increased proliferation, stem cells (Yin et al., 2014)	(Yin et al., 2014)
BMP	BMP4	BMPR	BMP4	activate	Decreased proliferation and stem cells (Qi et al., 2017)	(Thorne et al., 2018)
	LDN-193189	ALK2/3	BMPR-i	inhibit	Increased proliferation and stem cells (Li et al., 2018)	(Thorne et al., 2018)
TGF-β	TGF-β	TGF-βR	TGF-β	activate	Important for differentiation *in vivo* *(Flentjar et al., 2007; van der Flier et al., 2009; Li et al., 2018)*	(Han et al., 2014)
	EW-7197	ALK4/5	TGF-βR-i	inhibit	?	(Hong et al., 2017)
Notch	DAPT	γ-secretase	Notch-i	inhibit	Increased secretory cell types (VanDussen et al., 2012)	(Yin et al., 2014)
IL-4-JAK	IL-4	IL-4R	IL-4	activate	Increased goblet cells (von Moltke et al., 2015)	(von Moltke et al., 2015)
	baricitinib	JAK1/2	JAK1/2-i	inhibit	Altered stem cell numbers (Batlle et al., 2002; Richmond et al., 2018)	(Dames et al., 2015)
HDAC	valproic acid	HDAC1/2	HDAC-i	inhibit	Increased stem cells (von Moltke et al., 2015; Yin et al., 2014)	(Yin et al., 2014)
p38 MAPK	SB202190	p38 MAPK	p38 MAPK-i	inhibit	Increased proliferation (Houde et al., 2001; Sato et al., 2011)	(Sato et al., 2011)

Table 2.5: Top perturbations in modulating cell type composition.

	Downregulating		Upregulating	
	Perturbation	**Log_2fc**	**Perturbation**	**Log_2fc**
EdU^+ stem number	BMP4 + JAK1/2-i	-11.380	GSK3-i + p38 MAPK-i	2.602
	BMP4	-11.080	GSK3-i + JAK1/2-i	2.405
	BMP4 + Wnt3a	-10.380	BMPR-i + p38 MAPK-i	2.363
TA number	EGFR-i + HDAC-i	-9.476	GSK3-i + Wnt3a	1.541
	IL-4 + PORCN-i	-9.437	GSK3-i + JAK1/2-i	1.415
	EGFR-i + TGF-βR-i	-8.512	BMPR-i + Wnt3a	1.240
Secretory fraction (of differentiated cells)	TGFβ + Wnt3a	-1.544	GSK3-i + EGFR-i	1.109
	BMP4 + TGFβ	-1.509	EGFR-i + BMPR-i	1.096
	TGFβ + HDAC-i	-1.452	EGFR-i + JAK1/2-i	1.062
Paneth fraction (of secretory cells)	IL-4 + TGF-β	-1.651	BMPR-i + HDAC-i	0.307
	PORCN-i + TGF-β	-1.466	GSK3-i + HDAC-i	0.305
	IL-4 + p38 MAPK-i	-1.417	EGFR-i + TGF-β	0.270
Goblet fraction (of secretory cells)	EGFR-i + TGF-β	-1.209	IL-4 + p38 MAPK-i	0.724
	Notch-i + EGFR-i	-0.880	TGF-βR-i + Wnt3a	0.611
	EGFR-i + PORCN-i	-0.558	IL-4 + TGF-β	0.604
EE fraction (of secretory cells)	TGF-βR-i + Wnt3a	-1.525	PORCN-i + TGF-β	2.885
	IL-4 + HDAC-i	-1.419	Notch-i + TGF-β	2.542
	GSK3-i + HDAC-i	-1.098	TGF-β	2.282

Table 2.6: Concentrations of perturbations used in study.

Perturbation	Vendor and Catalog #	Concentration
DAPT (Notch-i)	Stemgent #04-0041	10 μM
CHIR-99021 (GSK3-i)	Sigma Aldrich #1046	3 μM
Valproic acid (HDAC-i)	Sigma Aldrich #P4543	1 mM
IWP-2 (PORCN-i)	Selleck Chemicals #S7085	2 μM
Wnt3a	R&D Systems #5036-WN-500	200 ng/mL
TGF-β	PeproTech #100-21C	4 ng/mL
EW-7197 (TGF-βR-i)	Selleck Chemicals #S7530	1 μM
BMP4	R&D Systems #314-BP-010	200 ng/mL
LDN-193189 (BMPR-i)	Sigma Aldrich #SML0559	1 μM
Baricitinib (JAK1/2-i)	Selleck Chemicals #S2851	2 μM
SB202190 (p38MAPK-i)	Sigma Aldrich #S7067	10 μM
IL-4	PeproTech #214-14	20 ng/mL
Erlotinib HCl (EGFR-i)	Selleck Chemicals #S1023	2.5 μM
PD0325901 (MEK-i)	Selleck Chemicals #S1036	1 μM
Palbociclib (PD-0332991) (CDK4/6-i)	Selleck Chemicals #S1116 (organoid studies) or LC Laboratories #-7744 (*in vivo* studies)	10 μM
Flavopiridol (CDK-i)	Selleck Chemicals #S2679	0.3 μM
AT9283 (AuroraK-i)	Selleck Chemicals #S1134	1 μM

Table 2.7: Concentration of antibodies used in study.

Epitope	Vendor and Catalog #	Dilution
Lysozyme (Lyz)	Dako	1:2000
Mucin-2 (Muc2)	Santa Cruz Biotechnology #15334	1:100
Chromogranin A (ChgA)	Santa Cruz Biotechnology #393941	1:100
GFP	Abcam #5450	1:2000
Dclk1	Abcam #31704	1:1000
Erk1 (pT202/pY204) + Erk2 (pT185/ pY187) (pErk)	Abcam #50011	1:200
Cyclin D1	Life Technologies #MA5-14512	1:200
Active Caspase-3	BD Pharmingen #559565	1:500

Table 2.8: Primers used in study

Target mRNA	Forward Primer	Reverse Primer
Atoh1	5'-TCCCCTTCCTCCTACCTTCTCC-3'	5'-CAACACGCAAGGATGAACTCCC-3'
Hes1	5'-AGAAGAGGCGAAGGGCAAGAAT-3'	5'-TGGAATGCCGGGAGCTATCTTT-3'
Lyz	5'-AAGAATGCCTGTGGGATCAA-3'	5'-CGGTTTTGACATTGTGTTCG-3'
Muc2	5'-ACCCCAAGCCCTTCTCCTACTA-3'	5'-AGTGGATTGAGAGGTCACAGGC-3'
ChgA	5'-GCAACACAGCAGCTTTGAGGAT-3'	5'-GTTAGGCTCTGGAAAGGCCTGA-3'
Bmp2	5'-GCTTCTTAGACGGACTGCGG-3'	5'-GCAACACTAGAAGACAGCGGGT-3'
β-actin	5'-CGCCACCAGTTCGCCATGGA-3'	5'-TACAGCCCGGGGAGCATCGT-3'
Lgr5	5'-ACCCGCCAGTCTCCTACATC -3'	5'-GCATCTAGGCGCAGGGATTG -3'
Ki67	5'-GTCAGCAAGAGGCAGCAAGGGG -3'	5'-CTGGGTCTTTGCCACTGGCTGG -3'

Table 2.9: Model variants for incorporating cell cycle inhibition.

Model	Absorptive	Secretory	Relation to Model 0
0	$E(A) = A_0(2p)^{\frac{T}{\tau_a}}$	$E(S) = S_0(2p)^{\frac{T}{\tau_s}}$	-
1	$A = A_0(2)^{\frac{(2p_1-1)T}{\tau_a}}$	$S = S_0(2)^{\frac{(2p_1-1)T}{\tau_s}}$	$p_1 = \frac{1}{2}(log_2 p + 2)$
2	$A = A_0(2)^{\frac{T}{c\tau_a}}$	$S = S_0(2)^{\frac{T}{c\tau_s}}$	$c = \frac{1}{log_2 p + 1}$
3	Same as model 0, except cell cycle arrested TA cells differentiated		Same p

CHAPTER 3

Differential Toxicity to Murine Small and Large Intestinal Epithelium Induced by Oncology Drugs

INTRODUCTION

The leading cause of attrition in drug development is toxicity (Waring et al., 2015; Cook et al., 2014). Drug-induced toxicity is first assessed through acute toxicology studies in animals, which are conducted as a precursor to clinical trials (Denny et al., 2017). By this stage, much effort has already been expended in drug candidate optimization, and drug failures are extremely costly. Animal studies are low-throughput and expensive, and it is currently infeasible to screen compounds for toxicity earlier in development when there are hundreds of candidates. Development of scalable models for predicting drug-induced toxicity can guide decisions early in drug development, reduce pre-clinical failures and enable the progression of safer drug candidates (Carr et al., 2017).

The gastrointestinal (GI) tract is one of the most common sites of toxicity both in drug development and in the clinic (Cook et al., 2015; Boussios et al., 2012; Al-Saffar et al., 2015). Several in vitro intestinal models have been recently developed that enable systematic investigation of intestinal drug absorption, drug metabolism, and anticancer efficacy (Kwon et al., 2021; Brandenberg et al., 2020; Yamashita et al., 2021). These systems either utilize cancer-derived cells, lack both proliferative and differentiated cell types, or do not model both the small and large intestines. Current evaluation of drug-induced GI toxicity continues to rely heavily on histological analysis of rodent intestinal epithelia. These studies describe the types of drug-induced damage to the intestinal epithelium, including villus stunting, crypt dysplasia, and mucin

hypersecretion (Pereira et al., 2016; Sangild et al., 2018; Ribeiro et al., 2016), yet it remains a challenge to pinpoint biological mechanisms of GI toxicity.

Further, there are differences in the physiology and biology between the small and large intestine which may cause drugs to target parts of the GI tract differently. For example, the primary function of the small intestine is nutrient absorption, while the large intestine is responsible for water absorption (Kiela et al., 2016); to optimally perform these tasks, a gradient in transporter expression exists across the GI tract. It remains unclear if biological differences in the small and large intestine, such as transporter expression, metabolism, or cell type composition, cause drugs to exhibit differential toxicity to the small and large intestine. Current in vitro intestinal models and in vivo histological studies tend to be limited to one part of the GI tract, which prevents differential toxicity from being identified.

Here, we built a scalable murine intestinal monolayer system to provide assessment of toxicity to both the small and large intestines. To help maintain in vivo properties essential for modeling drug-induced toxicity, these intestinal monolayers are derived directly from freshly harvested murine crypts. As a proof-of-concept, we screened 48 clinically used oncology drugs for both small and large intestinal toxicity, revealing that many oncology drugs display differential toxicity across the murine GI tract.

RESULTS

Characterizing Gastrointestinal Toxicity Utilizing Intestinal Monolayers

We had three main considerations for our toxicity screen (Figure 3.1 A): drug set, experimental model, and toxicity readout. For our drug panel, we focused on clinically used oncology drugs, which are known to induce widespread GI toxicity (Andreyev et al., 2012; Wardill et al., 2014;

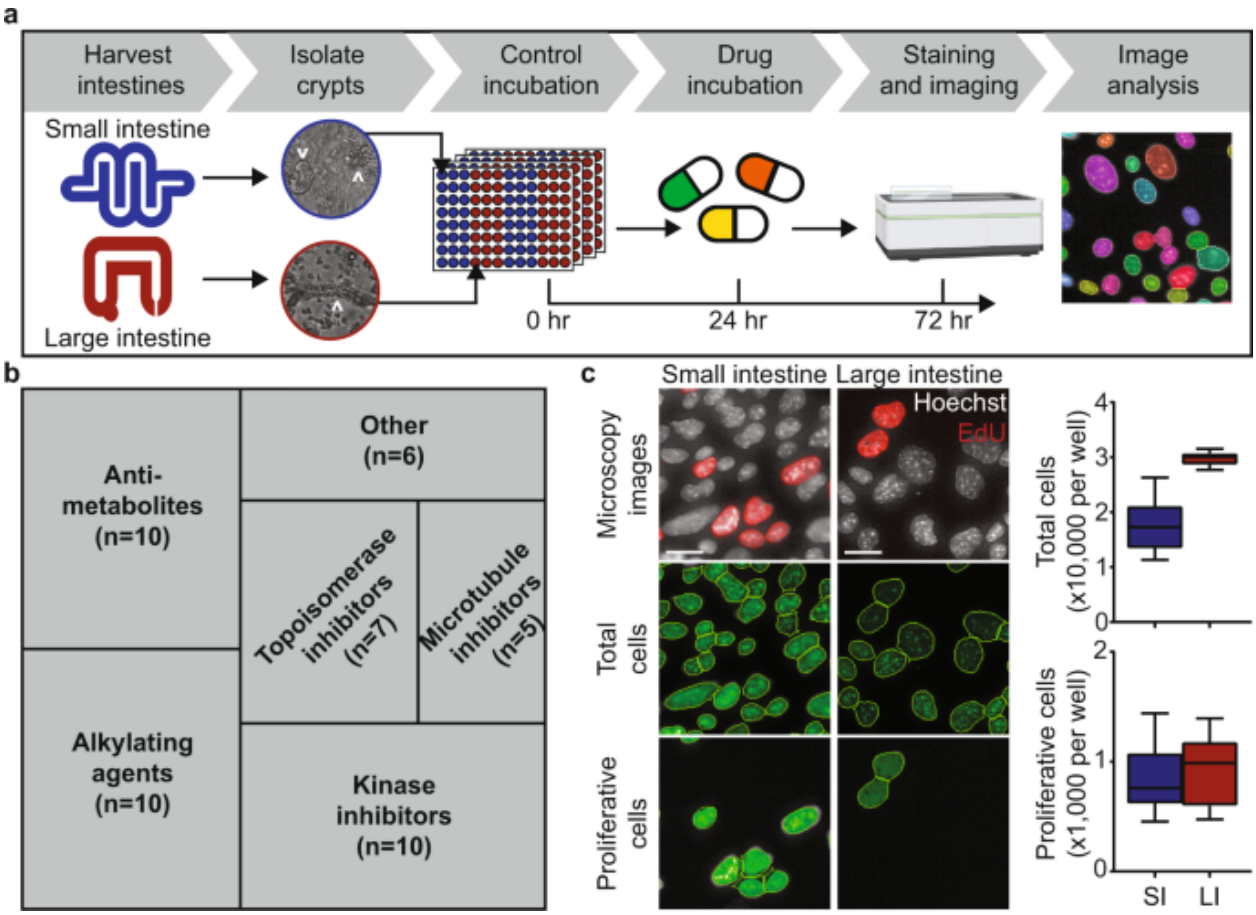

Figure 3.1: Experimental setup to screen small and large intestine-derived monolayers for drug toxicity. (A) Workflow for culturing and characterizing the effect of oncology drugs in small and large intestine-derived monolayers. Crypts isolated from harvested murine small and large intestines (white arrowheads) are cultured as intestinal monolayers. Intestinal monolayers are grown in control media for 24 h, followed by drug incubation for 48 h. Total and proliferative cell numbers are measured from images of stained intestinal monolayers. Microscope cartoon was created with BioRender.com. (B) Tree plot of the drug classes included in the drug panel. n: number of drugs per class. (C) Images of small and large intestine-derived monolayers grown in control media for 72 h. Scale bars, 20 µm. The total number of cells per well were determined via nuclei segmentation (Hoechst stain) and the number of proliferative cells per well were determined via EdU+ nuclei segmentation. Boxplot showing median value, whiskers showing lower 10th and upper 90th percentiles. n = 72 wells.

Rubenstein et al., 2004; Elting et al., 2003). We selected 48 FDA-approved oncology drugs that encompass multiple drug classes and diverse treatment indications (Figure 3.1 B, Figure 3.2, and Table 3.1). We chose two concentrations for each drug: a high concentration (typically greater than the reported cellular IC_{50}, Table 3.1) and a low concentration (100-fold lower than the high

concentration) (Yang et al., 2013). We note that the selected low concentration for most drugs is lower than its clinically observed maximum plasma concentration (C_{max}, Table 3.1) (Liston & Davis, 2017).

For our experimental model, we chose to make use of monolayers derived from both the murine small and large intestine. First, intestinal monolayers are 2D and thus are amenable to quantitative high-throughput microscopy (Sanman et al., 2020). This allowed us to survey the effects of many drugs on both the small and large intestine. Second, intestinal monolayers recapitulate many properties of the intestinal epithelium (Thorne et al., 2018; Sanman et al., 2021). These properties include apical-basolateral polarization, presence of the major differentiated cell types, cell-cell junctions, and continuous self-renewal (Figure 3.3 A,B)(Beumer & Clevers, 2016; Cheng & Leblond, 1974; Gehart & Clevers, 2019). Third, intestinal monolayers recapitulate specific properties of the organ they are derived from. Large intestine-derived monolayers have a greater proportion of goblet (Muc2+) cells, lack Paneth (Lyz+) cells, and have nuclear expression of special AT-rich sequence-binding protein 2 (SATB2), while small intestine-derived monolayers possess Paneth cells and an increased proportion of proliferative (EdU+) cells (Figure 3.3 A,C,D)(Bowcutt et al., 2014; Munera et al., 2017). Fourth, intestinal monolayers are ideal for investigating toxicity intrinsic to the GI epithelium, as they lack mesenchymal cells (Figure 3.3 E) (Thorne et al., 2018). Fifth, intestine-derived monolayers have similar gene expression to their in vivo counterparts (Figure 3.4 A,B). Finally, intestinal monolayers are derived from primary tissue rather than cancer cell lines. For these reasons, we made use of intestinal monolayers to broadly survey collateral damage of oncology drugs to healthy intestinal epithelial tissue.

To assess cytotoxicity of these oncology drugs to the GI tract, we chose two readouts of tissue health, measuring changes in cell numbers to the whole tissue (differentiated plus active-cycling cells) as well as changes specifically to the proliferative compartment (active-cycling cells only). Intestinal monolayers were cultured in 96-well imaging plates with control media for 24 h, followed by drug incubation for 48 h (Figure 3.1 A). EdU was incorporated two hours before fixation to label proliferative cells; Hoechst was added after fixation to identify cells' nuclei. Plates were imaged with an automated confocal microscope and the total number of nuclei and the number of proliferative cells per well were quantified (Figure 3.1 C). In summary, our image-based screen encompassed: 2 organs (small and large intestine) × 48 oncology drugs × 2 concentrations (100-fold range) × 2 toxicity readouts (total and proliferative cell numbers) × 3 replicates.

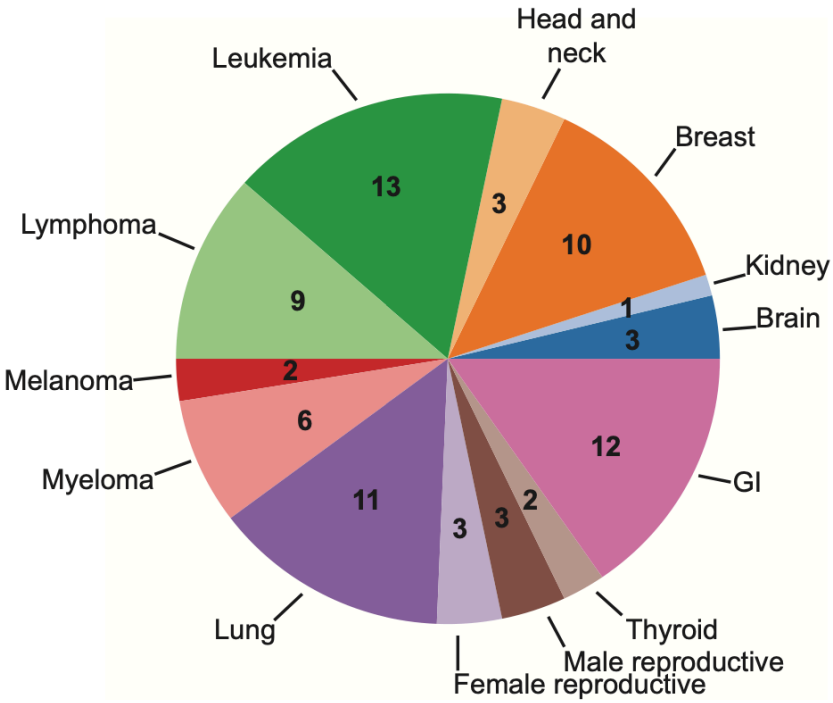

Figure 3.2: Cancer indications encompassed within the drug panel. Pie chart showing the number of drugs in the drug panel used to clinically treat each cancer indication.

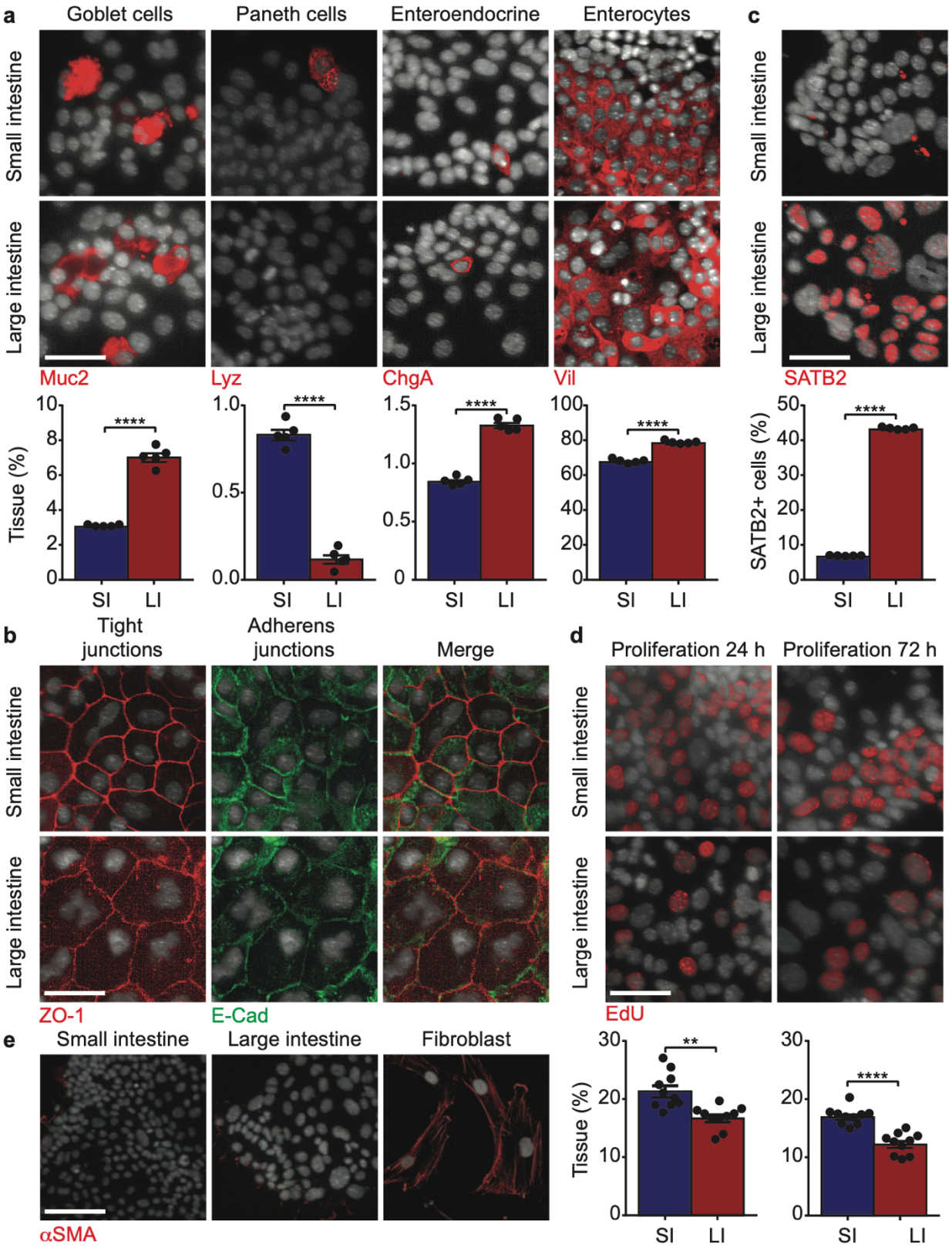

Figure 3.3: Characterization of small and large intestine-derived monolayers. (A) Top: Representative images of cell types in small and large intestine-derived monolayers grown in

(caption continued from previous page) control media for 24 h. Nuclei (Hoechst), goblet cells (Muc2), Paneth cells (Lyz), enteroendocrine cells (ChgA), and enterocytes (Vil) are visualized. Scale bars, 40 μm. Bottom: Quantification of the percent of cells in each well that have the indicated cell type marker (#marker+ cells/#total nuclei * 100%). n=5 wells. (B) Representative images of cell-cell junctions in small and large intestine-derived monolayers grown in control media for 72 h. Nuclei (Hoechst), tight junctions (ZO- 1), and adherens junctions (E-Cad) are visualized. Scale bars, 40 μm. (C) Top: Representative images of SATB2+ nuclei in small and large intestine-derived monolayers grown in control media for 24 h. Scale bars, 40 μm. Bottom: Quantification of the percent of cells that have nuclear SATB2 (#SATB2+ nulclei/#total nuclei * 100%). n=5 wells. (D) Top: Representative images of proliferative cells in small and large intestine-derived monolayers grown in control media for 24 or 72 h. Scale bars, 40 μm. Bottom: Quantification of the percent of cells that are proliferative (#EdU+ nuclei/#total nuclei * 100%). n=10 wells. (E) Small and large intestine-derived monolayers grown in control media for 48 h do not display alpha-smooth muscle actin staining (aSMA). Fibroblasts cultures were stained and imaged in parallel as a positive control for mesenchymal cells (aSMA+). Scale bars, 80 μm. Error bars mean +/- SEM. SI: small intestine; LI: large intestine. ** indicates p-values < 0.01; **** indicates p-values < 0.0001.

Identification of Oncology Drugs that Differentially Target Small or Large Intestine-Derived Monolayers

As expected, many of the screened oncology drugs decreased both total and proliferative cell numbers in intestinal monolayers (Figure 3.5 A and Figure 3.6 A). Overall, small intestine-derived monolayers were generally more sensitive to oncology drugs (Figure 3.5 B (blue circles) and Table 3.2). This is consistent with the observation that small intestine-derived monolayers have an increased proportion of proliferative cells compared to large intestine-derived monolayers (Figure 3.3 D).

Based on our survey, we chose to investigate cyclophosphamide (CP), methotrexate (MTX), and erlotinib (ERL), which were all toxic to the small intestine, but affected the large intestine in varying degrees, ranging from no toxicity, to intermediate toxicity, to strong toxicity, respectively (Figure 3.5 B (vertical axis)). We retested intestinal monolayers across multiple concentrations for these and several mechanistically related drugs. Consistently, small intestine-derived monolayers exhibited dose-dependent toxicity to CP, while large intestine-derived

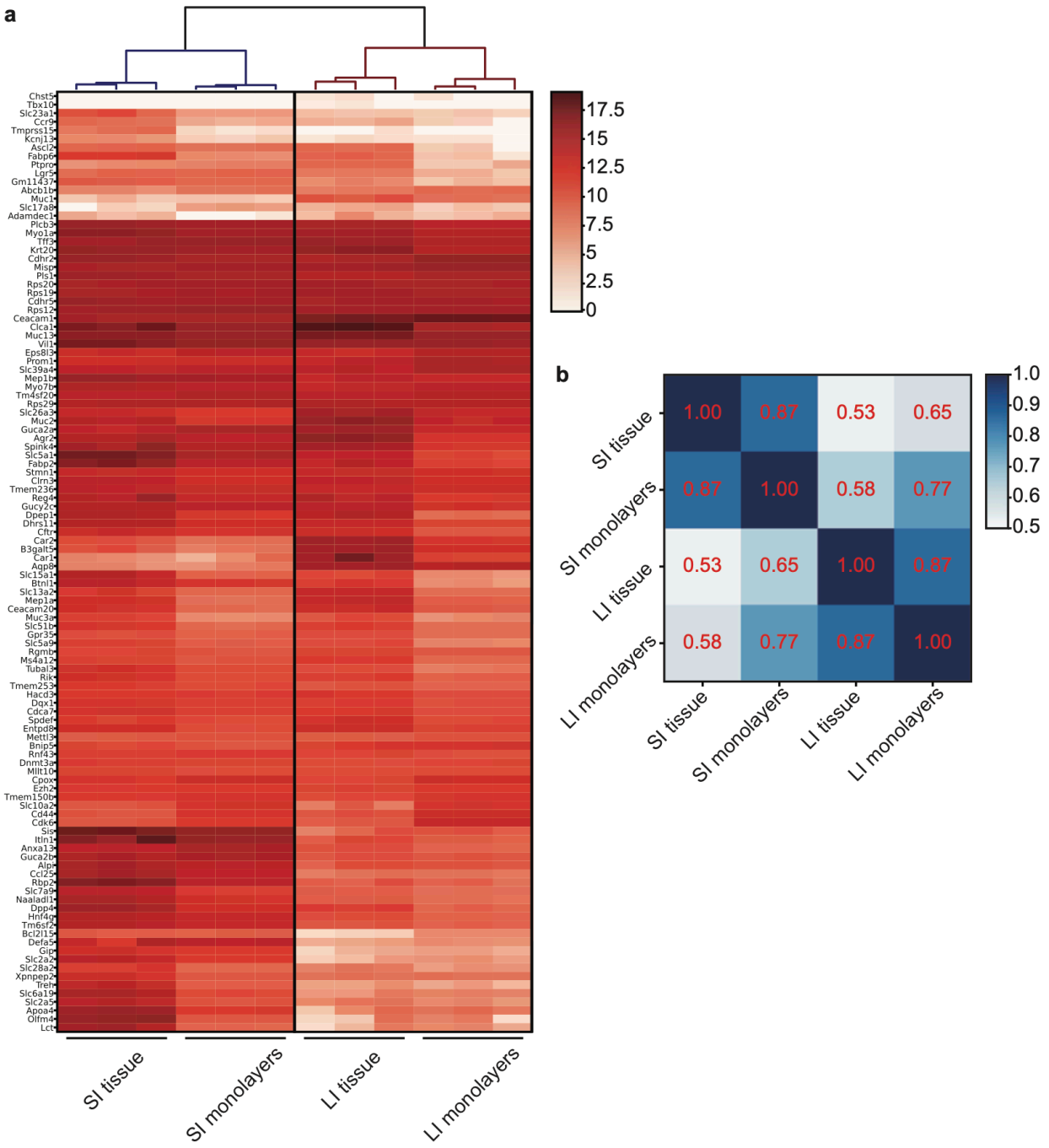

Figure 3.4: Comparison of transcriptome profiles of small and large intestines and cultured intestinal monolayers. (A) Dendrogram (top) and gene expression heatmap (bottom) based on hierarchical clustering of 110 intestine marker genes from RNA sequencing data. RNA was extracted from freshly harvested murine intestines (SI/LI Tissue) or from intestine-derived monolayers (SI/LI Monolayers) grown for 24 h. Scale bar represents the log transformed range of normalized gene expression. n=3 mice or n=3 pooled wells. (B) Pearson's correlation plot visualizing the correlation (*r*) values for the 110 intestine marker genes between samples. Scale bar represents the range of the correlation coefficients displayed.

a

Drug hits from toxicity screen

	Total cell number	Proliferative cell number
Small intestine	87.5% (42/48)	64.6% (31/48)
Large intestine	72.9% (35/48)	47.9% (23/48)

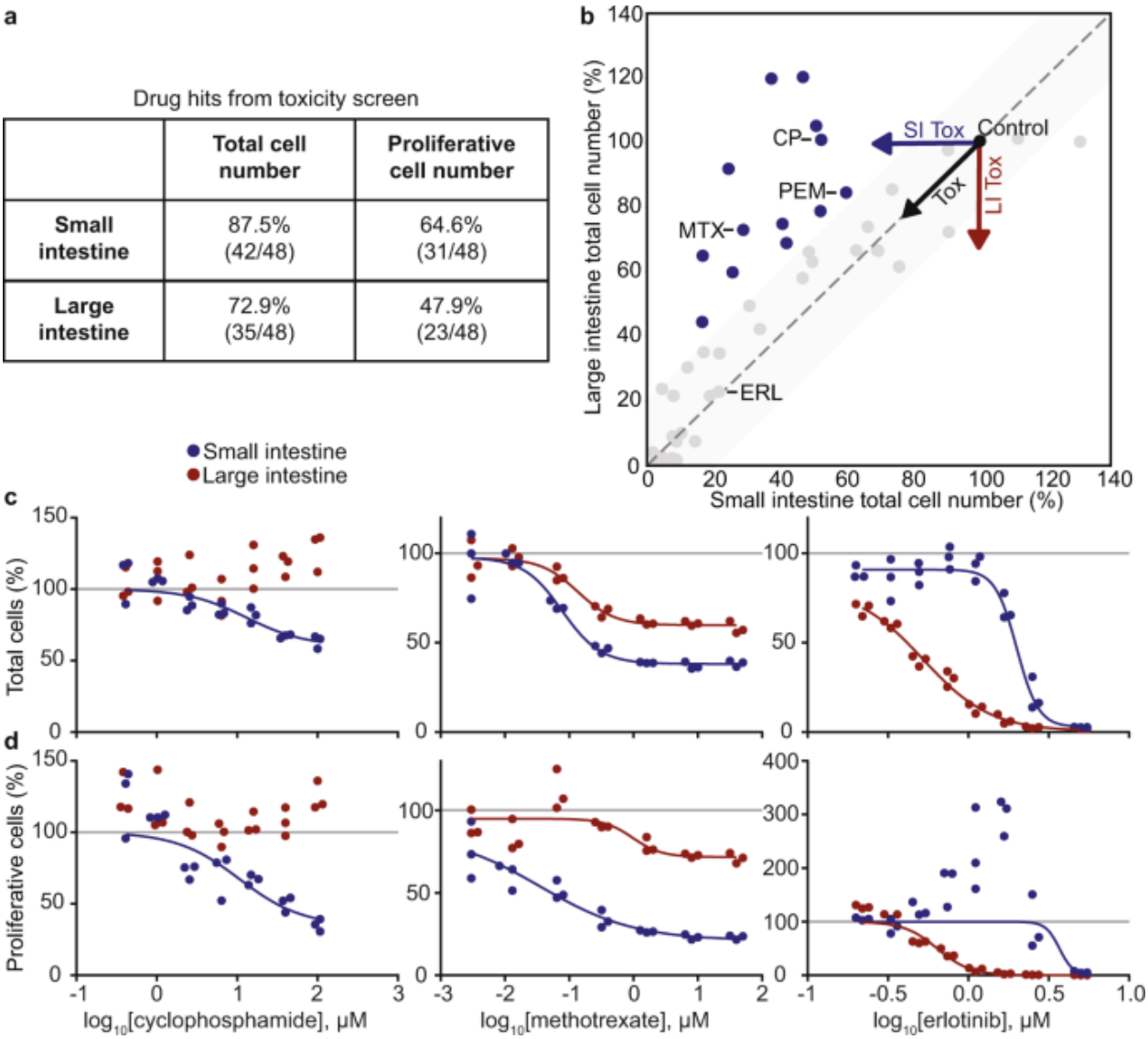

Figure 3.5: Identification of oncology drugs that differentially target small or large intestine-derived monolayers. (A) Number of drug hits from toxicity screen. (B) Selectivity of the high concentration of each drug in decreasing total cell number. Shaded region represents a selectivity <20%. Each circle is a drug, and blue circles are drugs selective (>20%) for the small intestine. Labeled compounds: MTX, methotrexate; PEM, pemetrexed; CP, cyclophosphamide; ERL, erlotinib. SI: small intestine; LI: large intestine; Tox: toxicity. (C,D) Small and large intestine-derived monolayers were treated with a 7–8 point dose-response of cyclophosphamide, methotrexate, and erlotinib, and change in cell number (C) or number of proliferative cells (D) relative to untreated cells are depicted. n = 3 wells. Fitted curves were used to calculate the LC_{50}, concentration required to kill 50% of cells, listed in Table 3.3.

monolayers were completely resistant (Figure 3.5 C,D and Table 3.3). The antifolates MTX and pemetrexed (PEM) induced stronger toxicity to the proliferative compartment in small intestine compared to large intestine-derived monolayers (Figure 3.5 D. Figure 3.6 B, and Table 3.3).

Interestingly, a dose-response of the epidermal growth factor receptor (EGFR) inhibitors erlotinib, gefitinib, and osimertinib revealed selective toxicity to large intestine-derived monolayers at intermediate concentrations (Figure 3.5 C,D, Figure 3.6 B,C, and Table 3.3). In summary, these dose responses revealed that antifolates and CP exhibited increased toxicity to small intestine-derived monolayers, while EGFR inhibitors displayed increased toxicity to large intestine-derived monolayers.

What could account for these differential toxicities? With respect to antifolates and CP, previous work suggests that increased uptake and metabolism (respectively) may be responsible for selective small intestine toxicity (Visentin et al., 2014; Qiu et al., 2006; Fleming, 1997; Xie et al., 2016). For these two cases, we focused on determining if these mechanisms are preserved in intestine-derived monolayers and testing whether differential toxicity is observed in vivo, which has surprisingly not been shown. With respect to EGFR inhibitors, a recent study has observed increased toxicity in the human large intestine (Pfau et al., 2020). In this case, we focused on elucidating mechanisms of EGFR inhibitor differential toxicity, which are poorly understood.

Differential Antifolate Toxicity is due to Increased Drug Uptake in the Small Intestine

We investigated whether selective antifolate toxicity towards small intestine-derived monolayers (Figure 3.7 A,B) is due to differences in antifolate uptake. It has been shown that the intestinal epithelium uptakes MTX and PEM via folate transporters, and that the small intestine exhibits increased folate absorption compared to the large intestine (Visentin et al., 2014; Que et al., 2006). First, we performed an MTX uptake assay in intestinal monolayers and confirmed the small intestine indeed uptakes more tritiated MTX (H^3-MTX) than the large intestine; MTX uptake plateaued in the large intestine by 15 min but increased roughly linearly for an hour in the small intestine (Figure 3.7 C). Second, treatment of intestinal monolayers with a potent folate

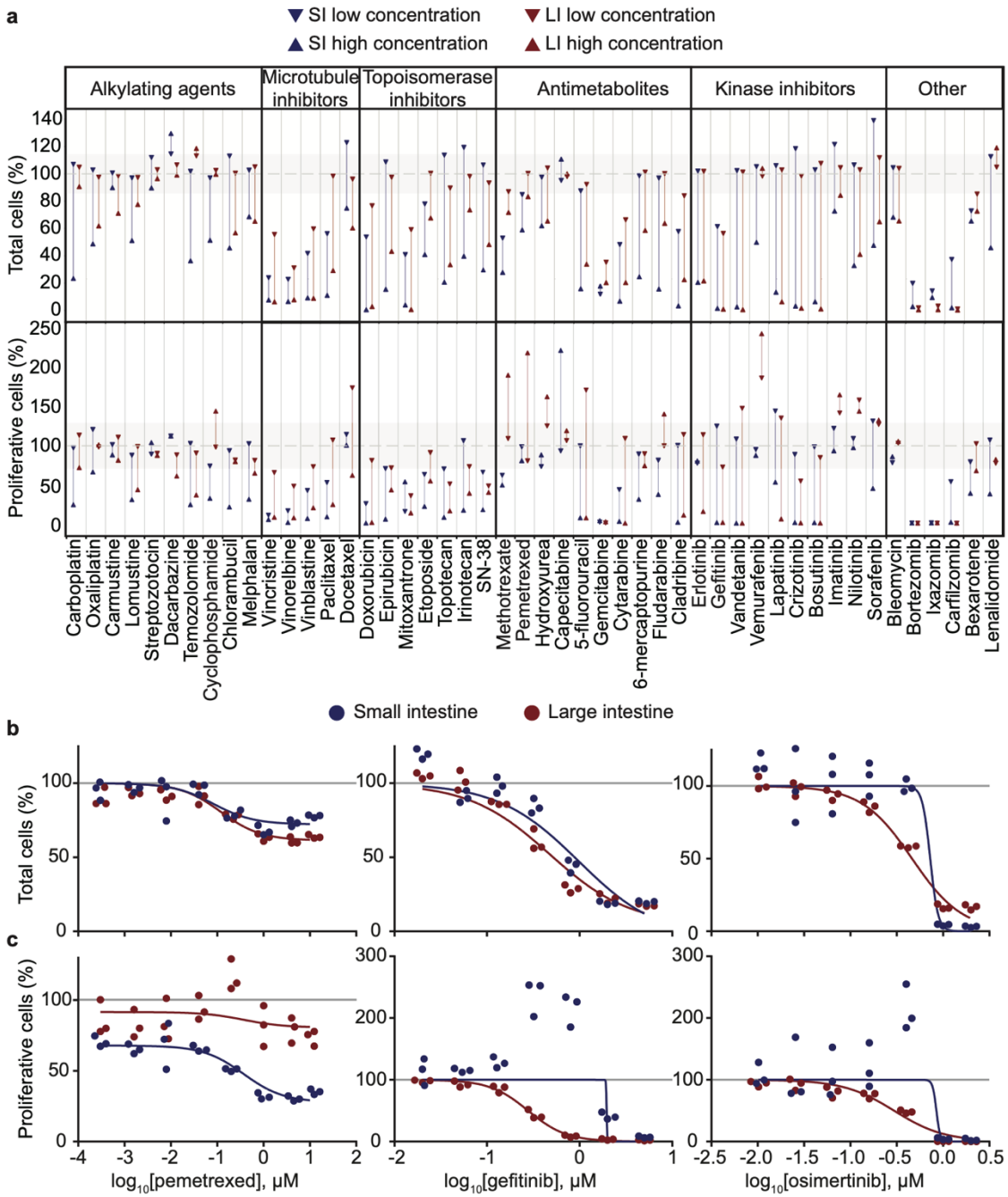

Figure 3.6: Toxicity screen summary and validation of differential toxicity for select drugs. (A) Effect of oncology drugs on total cell number (top) and proliferative cells (bottom) in small and large intestine-derived monolayers. Y-axis shows percent of total or proliferative cells in drug treatment normalized to untreated cells. X-axis shows each drug screened and is sorted by drug class. Blue lines depict small intestine and red lines depict large intestine response. Shaded region is one standard deviation of the plate-to-plate variability between control wells. n=3 wells. (B,C) Small and large intestine-derived monolayers were treated with a 7-8 point dose-response of pemetrexed, gefitinib, and osimertinib, and (b) change in cell number or (c) number of proliferative cells relative to untreated cells are depicted. n=3 wells. Fitted curves were used to calculate the LC50, concentration required to kill 50% of cells, shown in Table 3.3.

transporter inhibitor, sulfasalazine (SSZ), significantly decreased H^3-MTX uptake in the small intestine (Figure 3.8 A) (Jansen et al., 2004). As expected, folate transporters had significantly greater expression in the small intestine compared to the large intestine (reduced folate carrier (RFC) in intestinal monolayers; proton-coupled folate transporter (PCFT) in murine tissue; Figure 3.8 B). Third, we found that the cell-soluble antifolate trimetrexate, which can enter cells without the use of folate transporters (Marshall & DeLap, 1994), reduced the number of proliferative cells in both small and large intestine-derived monolayers (Figure 3.8 C). Taken together, these data show that small intestine-derived monolayers uptake more MTX, that MTX uptake is folate transporter dependent, and that bypassing transporters eliminates differential toxicity.

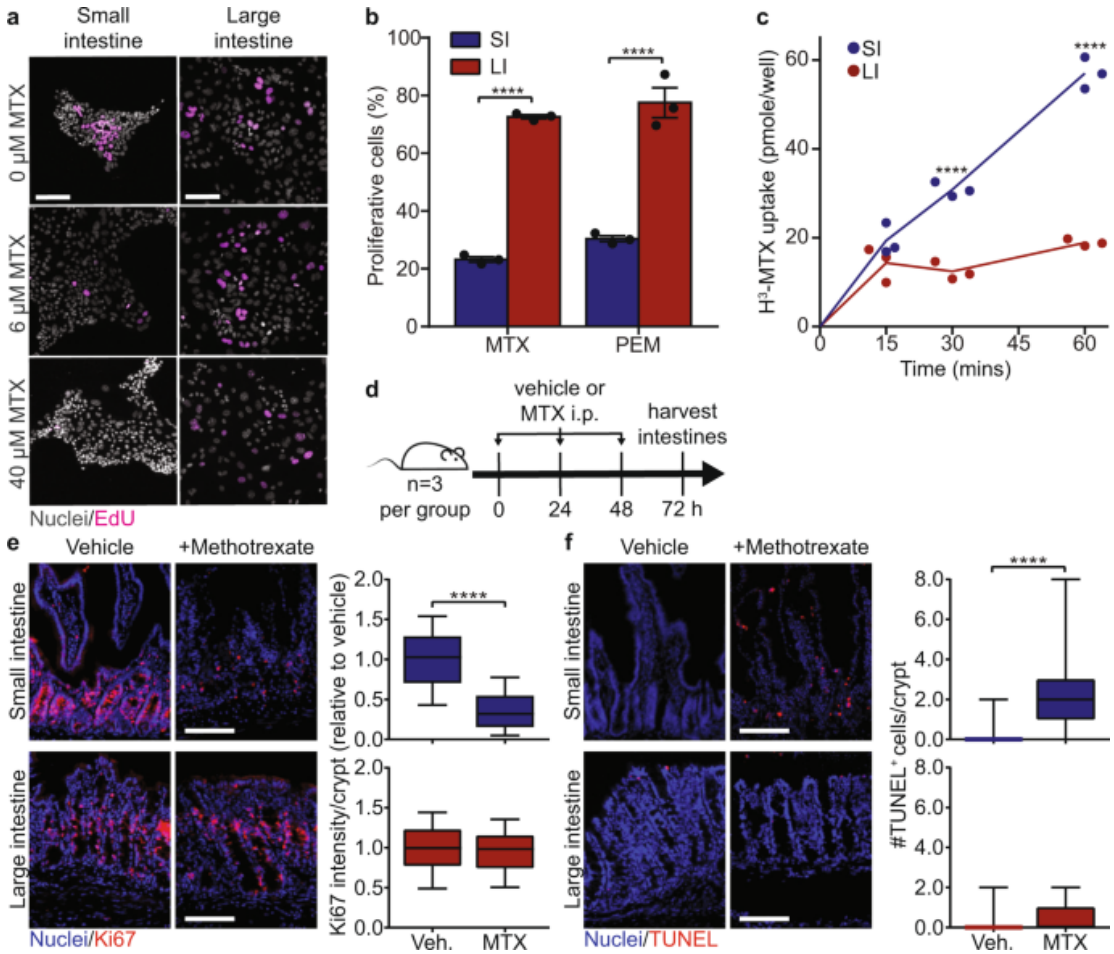

Figure 3.7: Differential antifolate toxicity is due to increased drug uptake in the SI.

(caption continued from previous page) (A) Representative images of small and large intestine-derived monolayers treated with the indicated methotrexate (MTX) concentration. Nuclei were stained with Hoechst and proliferative cells were stained with EdU. Scale bars, 100 μm. (B) Quantification of the percent change in proliferative cells relative to untreated cells in small and large intestine-derived monolayers treated with 8 μM MTX and 5 μM pemetrexed (PEM) for 48 h. n = 3 wells. (C) Small and large intestine-derived monolayers were incubated with 125 nM tritiated methotrexate (H^3-MTX) for 15, 30 or 60 min, then the amount of H^3-MTX per well was measured. n = 3 wells. (D) Schema for MTX in vivo treatment. (E) Changes in proliferation in small and large intestines from mice treated with MTX or vehicle. Representative images of small and large intestines stained for Ki67 and Hoechst. Scale bars, 100 μm. Quantification of the average Ki67 intensity per crypt. Boxplot showing median value, whiskers showing lower $10^{th}$and upper 90^{th} percentiles. n = 180 crypts from 3 mice (small intestine, blue bars) or n = 110 crypts from 3 mice (large intestine, red bars). (F) Changes in apoptosis in small and large intestines from mice treated with MTX or vehicle. Representative images of small and large intestines stained for TUNEL and propidium iodide. Scale bars, 100 μm. Quantification of $TUNEL^+$ cells per small (blue bars) and large (red bars) intestinal crypts. Boxplot showing median value, whiskers showing lower 1^{st} and upper 99^{th} percentiles. n = 60 crypts from 3 mice. Error bars mean ± SEM. **** indicates *p*-values < 0.0001.

We next tested whether MTX selectively targets the small intestine in vivo. Mice were treated with MTX or vehicle (Figure 3.7 D). After 72 h of treatment, small and large intestines were harvested for histological analysis of proliferation (Ki67) and apoptosis (terminal deoxynucleotidyl transferase (TdT) dUTP nick-end labeling (TUNEL)). RNA was also extracted from small and large intestines, and Ki67 RNA expression was measured by qRT-PCR. MTX treatment significantly decreased Ki67 RNA (Figure 3.8 D) and protein expression (Figure 3.7 E and Figure 3.8 E) in small intestine crypts, but not in large intestine crypts. MTX treatment also increased the number of apoptotic cells in small intestine crypts, while having no effect on the large intestine (Figure 3.7 F and Figure 3.8 F). These data confirm that MTX selectively targets the small intestine in vivo.

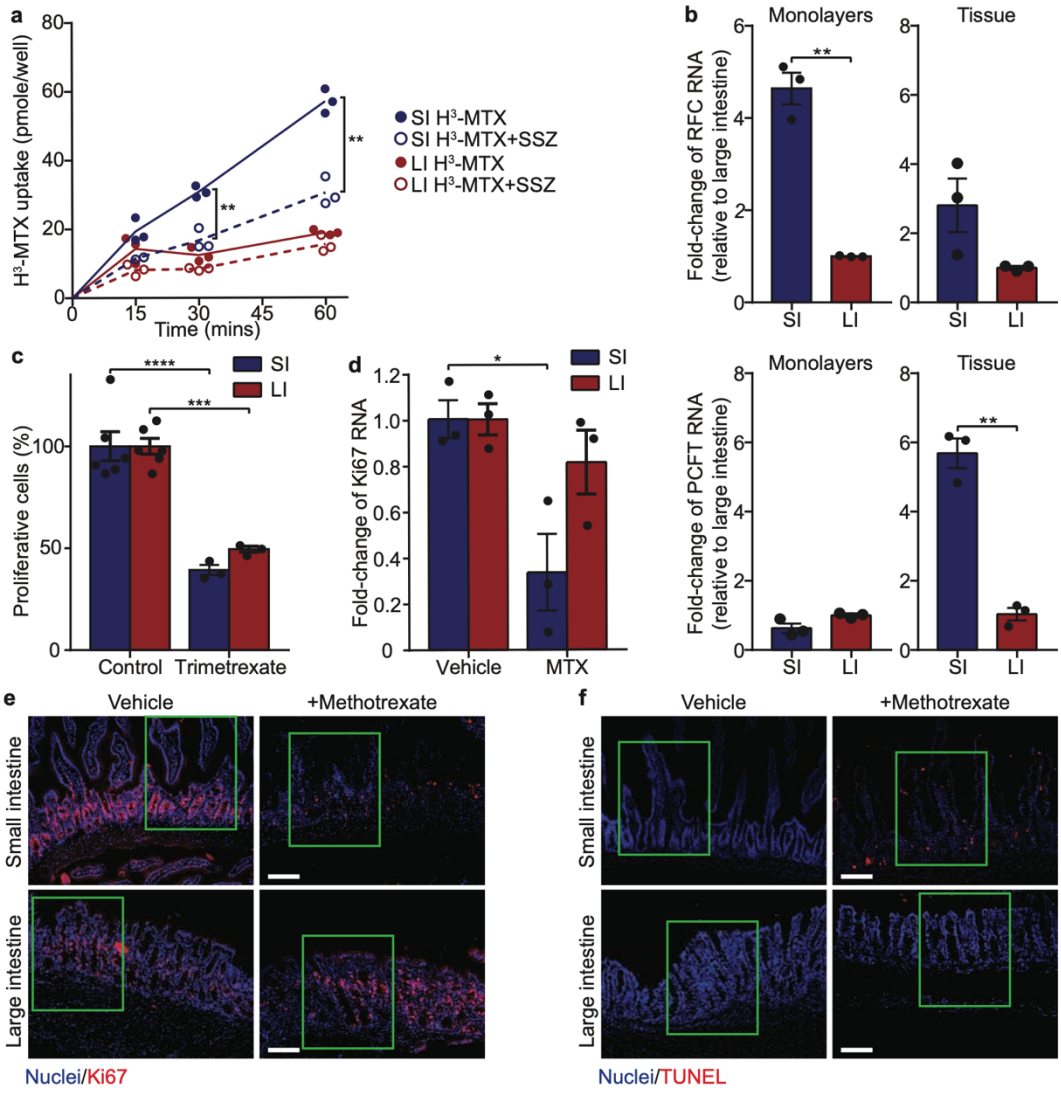

Figure 3.8: Further investigation of differential antifolate toxicity. (A) Small and large intestine-derived monolayers were incubated with 125 nM tritiated methotrexate (H3-MTX) ± 500 µM sulfasalazine (SSZ) for 15, 30 or 60 min, then the amount of H3-MTX per well was measured. n=3 wells. (B) Folate transporter RNA expression measured by qRT-PCR. Top: RFC expression measured in intestinal monolayers cultured for 24 h (left) and harvested murine intestinal tissue (right). Bottom: PCFT expression measured in intestinal monolayers cultured for 24 h (left) and harvested murine intestinal tissue (right). n=3 pooled samples or n=3 mice. (C) Quantification of the percent change in proliferative cells relative to untreated cells in small and large intestine-derived intestinal monolayers treated with 60 µM trimetrexate for 48 h. n=6 wells (control) or n=3 wells (trimetrexate). (D) Ki67 RNA expression measured by qRT-PCR. n=3 mice. (E) Zoomed out representative images of small and large intestines stained for Ki67 and Hoechst. Scale bars, 100 µm. Green inset is shown in Figure 3.7 E. (F) Zoomed out images of small and large intestines stained for TUNEL and propidium iodide. Scale bars, 100 µm. Green inset is shown in Figure 3.7 F. Error bars mean ± SEM. * indicates p-values < 0.05; ** indicates p-values < 0.01; *** indicates p-values < 0.001;**** indicates p-values < 0.0001.

Cyclophosphamide-Induced Small Intestinal Toxicity is due to Increased Drug Metabolism

The alkylating agent CP is a pro-drug that requires metabolic activation to 4-hydroxycyclophosphamide (4-OHCP), which then spontaneously breaks down to the active drug phosphoramide mustard (Figure 3.9 A) (Fleming, 1997). Cytochrome P450s (CYP450) are the main class of enzymes that hydroxylate CP to 4-OHCP (Figure 3.9 A) (Fleming, 1997; Pass et al., 2005), and the small intestine expresses multiple CYP450 genes, specifically CYP3A genes (Xie et al., 2016). First, we treated intestinal monolayers with 4-hydroperoxycyclophosphamide (4-HC), a stabilized analog of 4-OHCP (Low et al., 1982), to determine if hydroxylated CP causes toxicity to both the small and large intestine. Both CP and 4-HC showed toxicity in the small intestine, while only 4-HC showed toxicity in the large intestine (Figure 3.9 B and Figure 3.10 A), confirming hydroxylated CP is toxic to both the small and large intestine. Second, we measured greater expression and activity of CYP3A in small intestine compared to large intestine-derived monolayers (Figure 3.9 C and Figure 3.10 B; increased CYP3A expression is also observed in murine small intestine tissue) (Xie et al., 2016; Nelson et al., 2004). In fact, treatment of intestinal monolayers with dexamethasone, a CYP3A transcriptional activator (Down et al., 2007), increased CYP3A activity ~30 fold in the small intestine but showed no induction in the large intestine (Figure 3.10 C). Finally, we detected 4-OHCP by LC-MS/MS only in media collected from small intestine-derived monolayers incubated with CP (Figure 3.9 D and Figure 3.10 D). These data show that hydroxylated CP (4-HC) causes toxicity to both small and large intestinal monolayers, that small intestinal monolayers have greater CYP3A activity, and that the hydroxylated metabolite (4-OHCP) is only generated in small intestinal monolayers, which indicate that CP-induced small intestinal toxicity is due to metabolism of CP to its active state.

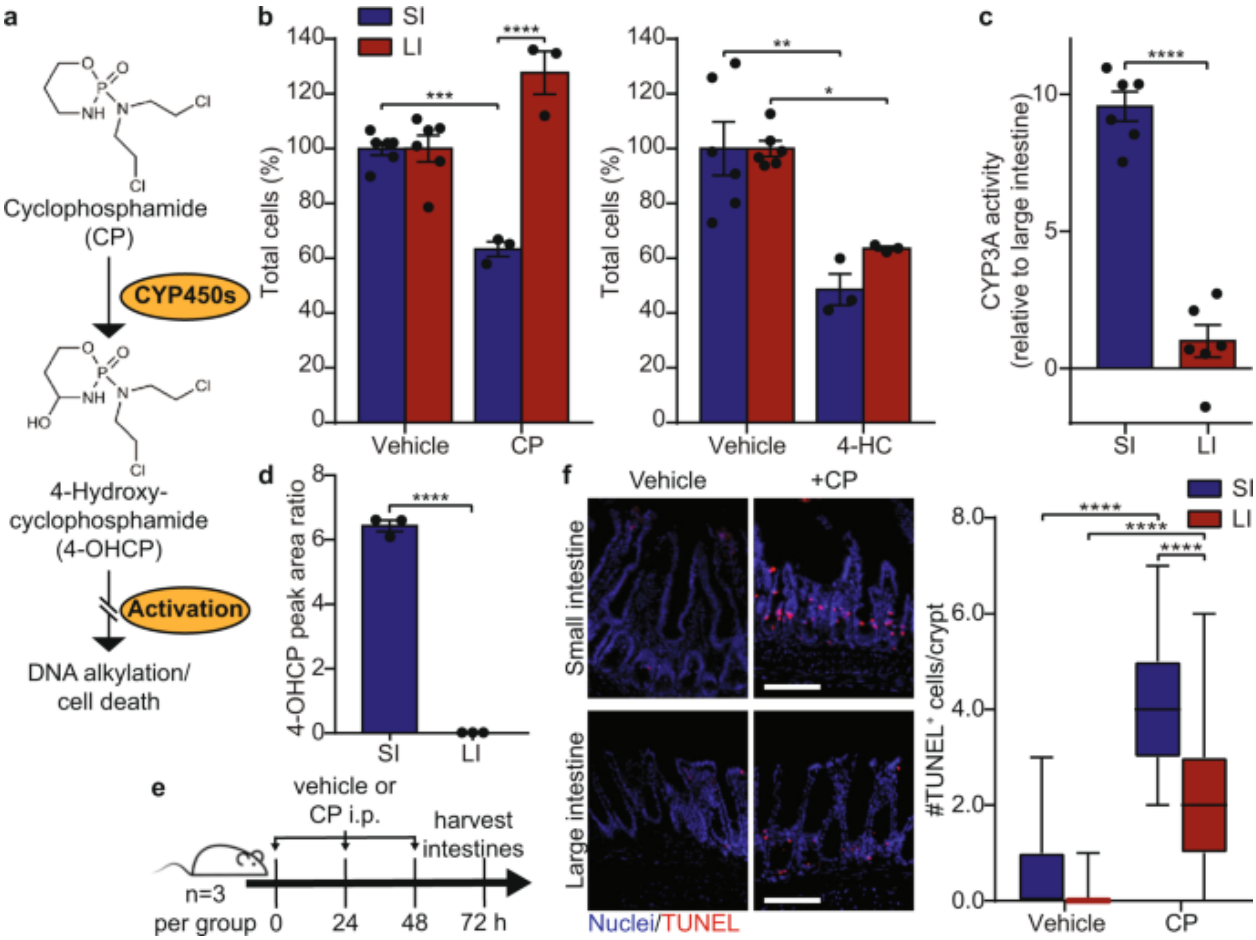

Figure 3.9: Cyclophosphamide-induced small intestinal toxicity is due to increased drug metabolism. (A) Schematic of CP activation. (B) Quantification of the percent change in total cells relative to untreated cells in small and large intestine-derived monolayers treated with 100 µM CP and 100 µM 4-HC for 48 h. n = 6 wells (control) or n = 3 wells (drug treatment). (D) Measured CYP3A activity in small and large intestine-derived monolayers. n = 6 wells. (D) Detection of 4-OHCP in the media of small and large intestine-derived monolayers incubated with 100 µM CP for 24 h by LC–MS/MS. Peak area ratio: sample 4-OHCP peak area/4-OHCP internal standard peak area. n = 3 wells. (E) Schema for CP in vivo treatment. (F) Changes in apoptosis in small and large intestines from mice treated with CP or vehicle. Representative images of small and large intestines stained for TUNEL and propidium iodide. Scale bars, 100 µm. Quantification of TUNEL^{+} cells per crypt. Boxplot showing median value, whiskers showing lower 1st and upper 99th percentiles. n = 60 crypts from 3 mice. Error bars mean ± SEM. * indicates p-values < 0.05; ** indicates p-values < 0.01; *** indicates p-values < 0.001; **** indicates p-values < 0.0001.

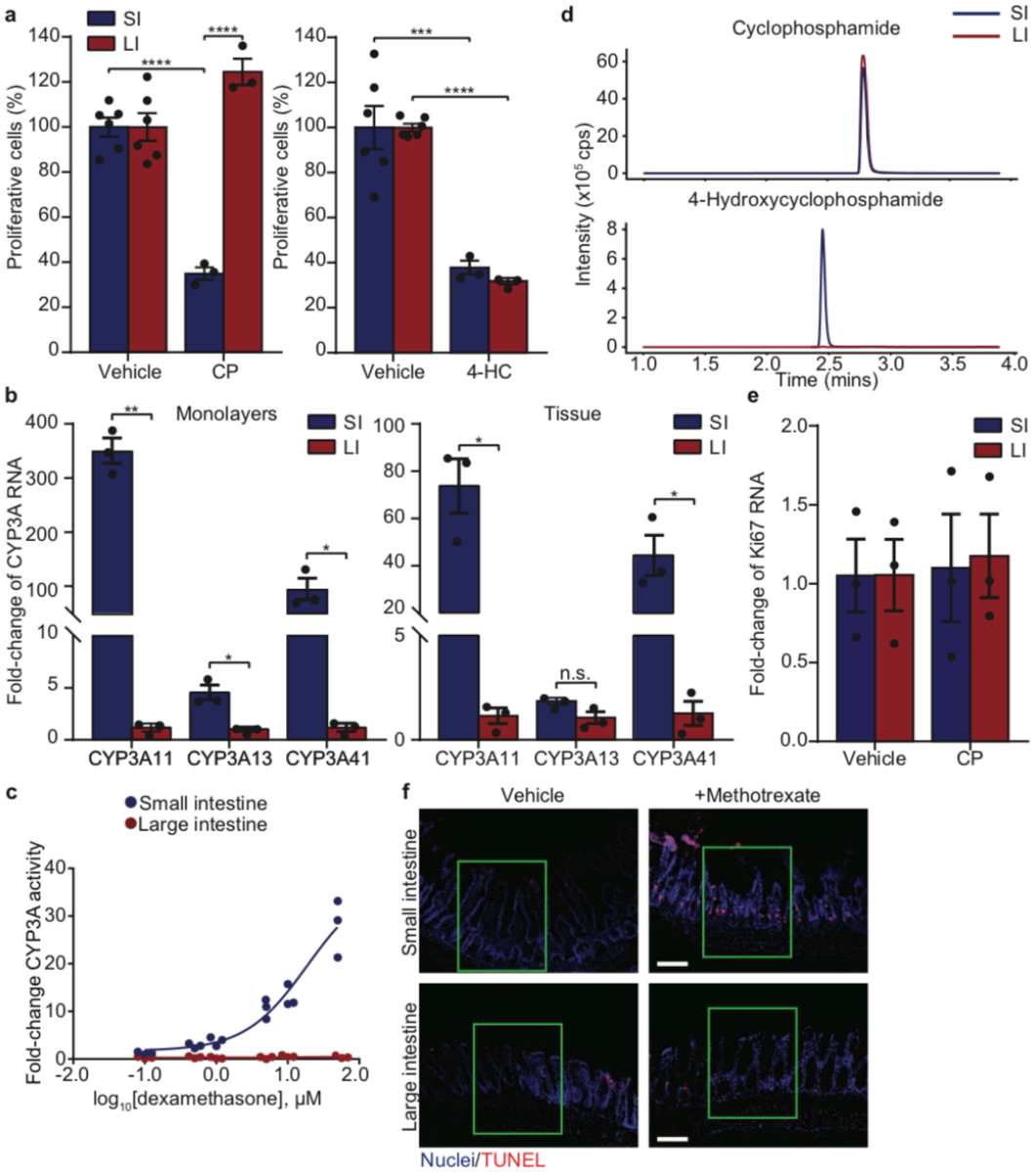

Figure 3.10: Further investigation of differential cyclophosphamide toxicity. (A) Quantification of the percent change in proliferative cells relative to untreated cells in small and large intestine-derived monolayers treated with 100 µM CP (left) and 100 µM 4-HC (right) for 48 hours. n=6 wells (control) or n=3 wells (drug treatment). (B) CYP3A11, CYP3A13, and CYP3A41 RNA expression measured by qRT-PCR. Left: CYP3A RNA expression measured in small and large intestine-derived monolayers cultured for 24 h. n=3 pooled samples. Right: CYP3A RNA expression measured in harvested murine small and large intestine tissue. n=3 mice. (C) CYP3A activity measured in intestinal monolayers treated with indicated concentration of dexamethasone for 48 h. Three parameter fit is shown. n=3 wells. d. Representative chromatogram of cyclophosphamide (top) and 4-HC (bottom) from LC-MS/MS run. (E) Ki67 RNA expression measured by qRT-PCR. n=3 mice. (F) Zoomed out images of small and large intestines stained for TUNEL and propidium iodide. Scale bars, 100 µm. Green inset is shown in Figure 3.9 F. Error bars mean ± SEM. * indicates *p*-values < 0.05; ** indicates p-values < 0.01; *** indicates p-values < 0.001; **** indicates p-values < 0.0001.

Last, we tested whether CP selectively targets the small intestine in vivo. Mice were treated with CP or vehicle (Figure 3.9 E). After 72 h of treatment, intestinal tissue and RNA were collected to measure changes to proliferation and apoptosis. CP treatment did not affect proliferation in either the small or large intestine, as shown by a lack of change in Ki67 RNA (Figure 3.10 E). This could be because the small intestine recovered in the 24 h between the last dose of CP and time of tissue harvest. CP treatment did, however, increase the number of apoptotic cells in both small and large intestine crypts, importantly having a more detrimental effect to the small intestine (Figure 3.9 F and Figure 3.10 F). The detection of low levels of apoptosis in the large intestine in vivo is likely due to the presence of CP metabolites generated in other organs (e.g., the small intestine and liver). These data confirm CP preferentially targets the small intestine in vivo.

Differential EGFR Inhibitor Toxicity is due to Decreased ERK Phosphorylation in the Large Intestine

We investigated how EGFR inhibitors selectively target large intestine-derived monolayers (Figure 3.11 A,B). The epidermal growth factor (EGF) signaling pathway plays a critical role in cell proliferation, as well as maintaining the intestinal stem cell population (Suzuki et al., 2010; Lenz et al., 2006). EGFR signals primarily through the RAS-RAF-MEK-ERK pathway and the PI3K-AKT-mTOR pathway (Wee & Wang, 2017). To determine which of these two pathways are responsible for EGFR inhibitor-induced toxicity, we treated both small and large intestine-derived monolayers with a dose-response of a MEK inhibitor (PD0325901) and an AKT inhibitor (MK2206). MEK inhibition induced toxicity to both the small and large intestine in a dose-dependent manner (Figure 3.11 C), while AKT inhibition had no effect on either the small or large intestine (Figure 3.12 A). Thus, MEK-ERK signaling is required for survival. To

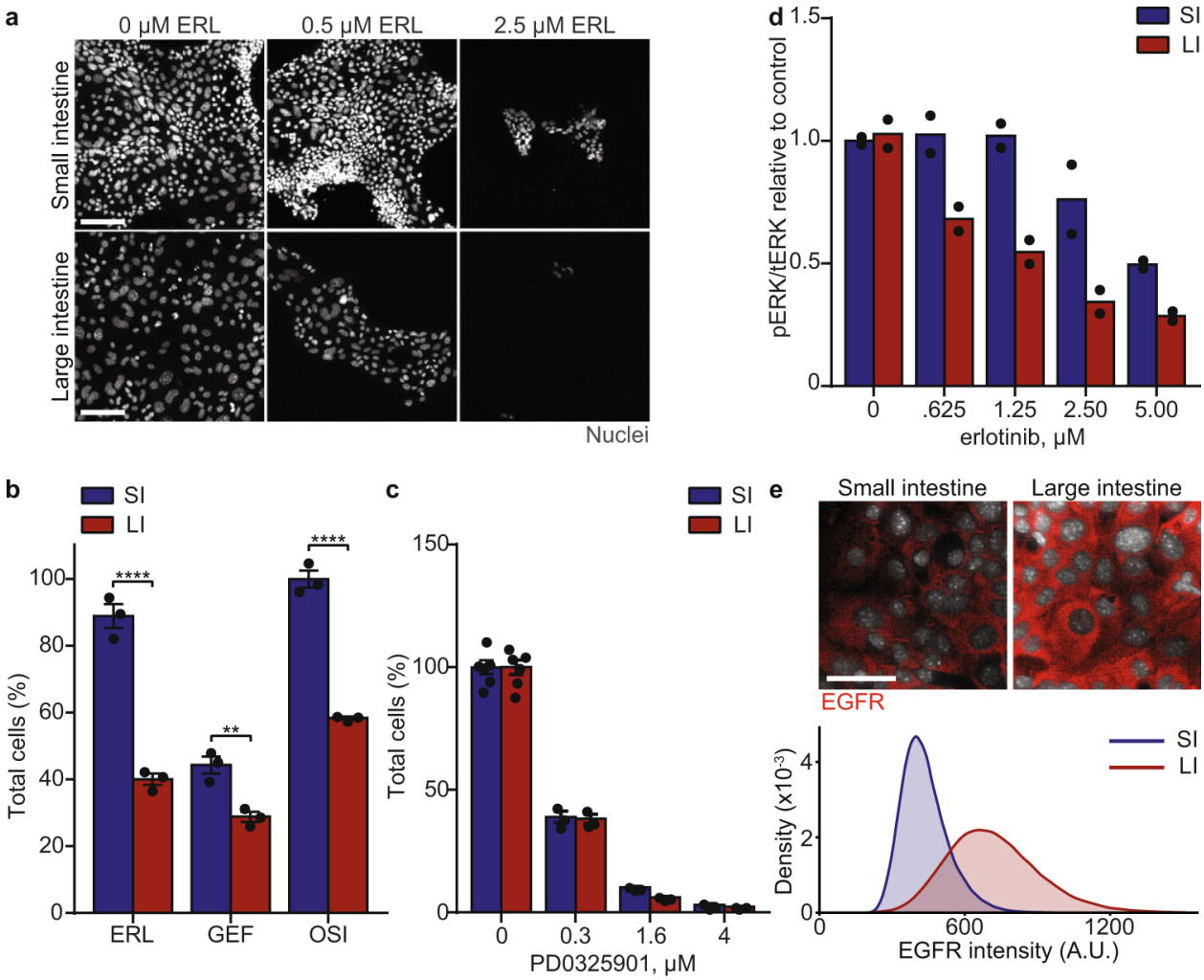

Figure 3.11: Differential EGFR inhibitor toxicity is due to decreased ERK phosphorylation in the large intestine. (A) Representative images of small and large intestine-derived monolayers treated with indicated erlotinib (ERL) concentration. Nuclei are stained with Hoechst. Scale bars, 100 μm. (B) Quantification of the percent change in total cells relative to untreated cells in small and large intestine-derived monolayers treated with 0.5 μM ERL, 0.8 μM GEF, and 0.4 μM OSI for 48 h. n = 3 wells. (C) Quantification of the percent change in total cells relative to untreated cells in small and large intestine-derived monolayers treated with the indicated concentration of PD0325901 for 48 h. n = 6 wells (vehicle) or n = 3 wells (PD0325901). All drug concentrations were statistically significant compared to control (p-value < 0.0001) (D) Quantification of phospho-ERK (pERK) relative to total-ERK (tERK) in small and large intestine-derived monolayers treated with the indicated concentration of erlotinib for 6 h measured by ELISA. n = 2 technical replicates. (E) Representative images of EGFR expression in small and large intestine-derived monolayers grown in control media for 24 h. Scale bars, 40 μm. Density plot of EGFR intensity per cell. A.U.: arbitrary units. n = >50,000 cells pooled from 5 wells. Error bars mean ± SEM. ** indicates p-values < 0.01; **** indicates p-values < 0.0001.

evaluate if ERK is differentially regulated, we measured the ratio of phospho-ERK to total-ERK in both small and large intestine-derived monolayers treated with a dose-response of the EGFR inhibitor erlotinib. These measurements revealed that erlotinib preferentially impairs ERK phosphorylation in the large intestine compared to the small intestine (Figure 3.11 D).

What mechanisms might underly differential regulation of ERK phosphorylation between the small and large intestine? First, we examined expression of EGFR. Quantification of intestinal monolayers revealed both higher EGFR protein (Figure 3.11 E) and RNA expression (also in murine intestinal tissue, Figure 3.12 B) in the large intestine compared to small intestine. Second, we measured higher expression of leucine-rich repeats and Ig-like domains-1 (Lrig1), a ligand that acts as an inhibitor of EGFR (Laederich et al., 2004), in small intestine compared to large intestine-derived monolayers (Figure 3.12 C). Third, we performed an unbiased profiling of phospho-receptor tyrosine kinase activity in small and large intestine-derived monolayers. Interestingly, we identified that the small intestine has increased expression of phospho-human epidermal growth factor receptor 2 (Her2) relative to phospho-EGFR, while these receptors are phosphorylated to similar extents in the large intestine (Figure 3.12 D). This is consistent with prior work, which has shown that Her2 signaling is primarily responsible for maintaining ERK activity in 3-dimensional small intestine organoids (Muta et al., 2018). Together, our data reveal that the large intestine is more reliant on EGFR-induced ERK phosphorylation and point to multiple components upstream of ERK that individually or together can lead to its differential regulation in small and large intestine-derived monolayers.

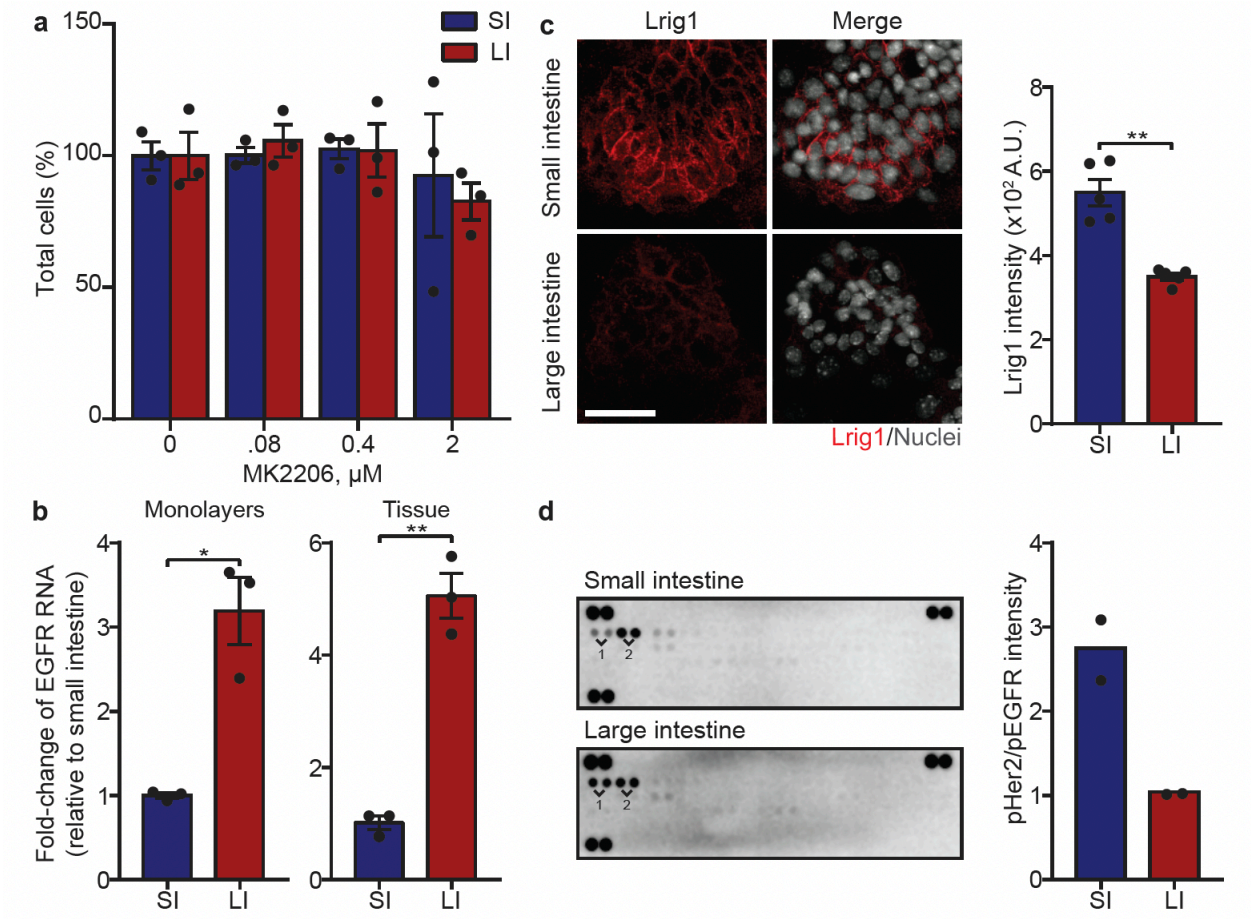

Figure 3.12: Further investigation of differential EGFR inhibitor toxicity. (A) Quantification of the percent change in total cells relative to untreated cells in small and large intestine-derived monolayers treated with the indicated concentration of MK2206 for 48 hours. n=3 wells. (B) EGFR RNA expression measured by qRT-PCR. Left: Expression measured in small and large intestine-derived monolayers cultured for 24 hours. n=3 pooled samples. Right: Expression measured in harvested murine small and large intestine tissue. n=3 mice. (C) Left: Representative images of Lrig1 in small and large intestine-derived monolayers grown in control media for 24 hours. Scale bars, 40 μm. Right: Quantification of Lrig1 intensity in intestinal monolayers. n= 5 wells. A.U.: arbitrary units. (D) Left: Representative images of a mouse phospho-RTK array for small intestine ederived monolayers (top) and large intestine-derived monolayers (bottom). 1: pEGFR; 2: pHer2. Right: Quantification of the relative intensity of phospho-Her2 (pHer2) to phospho-EGFR (pEGFR). n=2 biological replicates. Error bars mean ± SEM. * indicates p-values <0.05; ** indicates p-values < 0.01.

DISCUSSION

In this study, murine-derived intestinal monolayers provided a scalable system to survey drug-induced GI toxicity and a biologically relevant starting point to investigate mechanisms of

toxicity. We identified oncology drugs that cause differential toxicity to the murine small or large intestine and pinpointed biological mechanisms underlying these toxicity differences. Specifically, increased uptake of antifolates in the small intestine led to increased antifolate toxicity, increased metabolism in the small intestine led to increased CP toxicity, and decreased ERK phosphorylation in the large intestine led to increased EGFR inhibitor toxicity. Reassuringly, differential toxicity in intestinal monolayers was predictive of in vivo murine toxicity, as demonstrated by MTX and CP dosing causing increased damage to the murine small intestine.

A natural question is to what degree do murine intestinal models reflect toxicity in human intestines. With respect to EGFR inhibitor-induced differential toxicity, a recent study of non-small cell lung cancer patients treated with erlotinib showed that only the large intestine exhibited signs of erlotinib-induced toxicity (Pfau et al., 2020). With respect to the mechanisms by which antifolates and CP cause differential toxicity, it is well established that folate absorption and drug metabolism are greater in the human small intestine compared to the large intestine (Visentin et al., 2015; Qiu et al., 2006; Fleming et al., 1997; Xie et al., 2016). Thus, differential toxicity observed in murine intestinal monolayers may help predict toxicity in human intestines.

There are several limitations of our current investigation. First, our readouts focused on changes to total and proliferative cell numbers but did not examine other possible markers of tissue toxicity, such as inflammation, cell hyperplasia and barrier integrity (Chelakkot et al., 2018; Milano et al., 2004; Nenci et al., 2007). Second, we focused on acute rather than chronic toxicity, which can be important for medications prescribed over many years, such as NSAIDs (Harirforoosh et al., 2013). Third, our toxicity screening platform was based only on 2D murine-

derived intestinal monolayers. Our study motivates future work to expand cellular readouts of toxicity, as well as to systematically compare 2D vs 3D, and murine- vs human-derived organoid models.

High attrition rates due to drug safety continues to be a key challenge in early drug development (Waring et al. 2015; Cook et al., 2014). Knowing whether a novel therapeutic will induce GI toxicity is essential information for determining if a drug should continue in the development process. Cellular models have been invaluable for assessing pharmacological properties of drug candidates, including permeability and stability. Here, we provide proof-of-concept for using intestinal monolayers derived from fresh murine crypts to study and accurately predict murine GI toxicity of drugs. Moreover, including models of both the small and large intestine revealed biological insights into differences across the gut, enabling better mechanistic understanding of drug-induced GI toxicity.

METHODS

Mice

All animal care and experimentation were conducted under protocol AN-179937 agreed upon by the Administrative Panel on Laboratory Animal Care at the University of California, San Francisco. All our animal studies are performed in full accordance with UCSF Institutional Animal Care and Use Committee (IACUC). 5- to 6-week-old C57BL/6 mice (C57BL/6NHsd) were purchased from Harlan and housed with ad libitum food and water on a 12 h light cycle at the UCSF Preclinical Therapeutics Core vivarium.

Intestinal monolayer media

Organoid basal media (OBM) consists of Advanced DMEM/F12 with non-essential amino acids and sodium pyruvate (Fisher Scientific #12634-028) containing 1x N-2 (Fisher Scientific #17502-048), 1x B-27 (Invitrogen #17504-044), 10 mM HEPES (Invitrogen #15630080), 1x GlutaMAX (Invitrogen #35050-061), 1 μM N-acetylcysteine (Sigma Aldrich #A9165), 100 ug/mL Normocin (Invivogen #ant-nr-1), 100 U/mL penicillin and 100 μg/mL streptomycin (Corning #30-002). For initial seeding, intestinal monolayers were maintained in OBM supplemented with 3 μM CHIR-99021 (Sigma Aldrich #SML1046), 50 ng/mL murine EGF (Invitrogen #PMG8043), 1 μM LDN-193189 (Sigma Aldrich #SML0559), 500 ng/mL murine R-spondin-1 (Peprotech #315-32), 100 ng/mL Wnt3a (R&D Systems #5036-WN-500), and 10 μM Y-27632 (Selleck Chemicals #S1049). 4 h after initial seeding, media was changed into WENR media (OBM supplemented with 100 ng/mL Wnt3a, 50 ng/mL murine EGF, 100 ng/mL murine Noggin, and 500 ng/mL murine R-spondin-1). All drugs were applied in the background of WENR media.

Intestinal monolayer cultures

Small intestine-derived monolayers were cultured from adapted protocols (Sanman et al., 2020; Thorne et al., 2018; Sanman et al., 2021). Specifically, jejunum was isolated from male or female mice between 6–10 weeks of age. Epithelium was released from jejunal tissue by incubation in ice-cold PBS with 3 mM EDTA (Ambion #9260) in phosphate buffered saline (PBS, Gibco #10010049). Released epithelial tissue was washed 3x with OBM, after which crypts were separated from villus material using 100 and 70 μm cell strainers (BD Falcon) in succession. Crypts were resuspended in seeding media and plated on Matrigel (Thermo Fisher #CB-40234C)-coated 96-well optical bottom plates (Perkin Elmer #6055302; Greiner #655090).

Large intestine-derived monolayers were cultured by harvesting the large intestine from the same mice described above. The large intestine was first cut open longitudinally, then into 1–2 mm pieces. Large intestine pieces were placed in a falcon tube containing 4 mL of OBM supplemented with 10 μM Y-27632. Then 1.25 mg/mL Collagenase D (Sigma #11088866001), 1.25 U/mL Dispase (STEMCELL Technologies #07913), and 62.5 mU/mL DNAse (STEMCELL Technologies #07900) were added and the falcon tube was placed in a 37 °C incubator for 15 min. After incubation, 5 mM EDTA was added, and the falcon tube was placed in a 37 °C incubator for a second 15 min incubation. Large intestine crypts were separated from epithelial debris using a 100 μm filter. Crypts were washed 1x with OBM, then resuspend in seeding media and plated on Matrigel-coated 96-well optical bottom plates.

For both the small intestine and large intestine, 300 crypts were seeded per well. 4 h after seeding, cells were washed with OBM and incubated in WENR media for 24 h. After WENR media incubation, cells were washed with OBM and incubated with WENR media containing drugs of interest for indicated time.

Methotrexate and cyclophosphamide administration to mice and tissue harvest

To test for increased toxicity to the small intestine in vivo, MTX (Cayman Chemicals #13960) or CP (Sigma–Aldrich #C3250000) at 100 mg/kg in PBS were administered to mice by intraperitoneal injection at 0, 24, and 48 h. At 72 h, the small and large intestines were harvested for sectioning and intestinal crypts were isolated as described in ‘Intestinal monolayer cultures’. Crypts were lysed in Buffer RLT (RNEasy Kit, Qiagen #74134) for RNA purification.

Methotrexate uptake assay

To measure uptake of tritiated MTX (H3-MTX; American Radiolabeled Chemicals #ART0168), small and large intestine-derived monolayers were cultured in Matrigel-coated 48-well tissue

culture plates (Corning #353296) for 48 h. After 48 h, intestinal monolayers were washed with warm OBM and imaged on the IncuCyte S3 automated imaging system (Essen Biosciences) to calculate the confluence of each well. Intestinal monolayers were then incubated with 250 µL WENR media containing 125 nM H3-MTX for the indicated times at 37 °C. For inhibition studies, intestinal monolayers were incubated with 250 µL of 125 nM H3-MTX in the presence of 500 µM sulfasalazine (SSZ, Cayman Chemicals #15025).

After incubations, intestinal monolayers were washed 3x with 500 µL ice-cold PBS. Intestinal monolayers were then incubated in 300 µL RIPA buffer (Sigma–Aldrich #R0278) for up to 90 min. Then 250 µL of cell lysate was used to measure the amount of H3-MTX. 2.5 mL of Ecolite Liquid Scintillation Cocktail (MP Biomedicals #0188247501) was added, and the radioactivity was measured by liquid scintillation counting on a Beckman LS6500 liquid scintillation counter (Beckman Coulter). The average radioactivity from Matrigel-coated only wells was subtracted from all intestinal monolayer wells. Further, radioactivity measurements were normalized to the average confluence of all small intestine or large intestine-derived monolayer wells. Picomoles of H3-MTX in each well was calculated by normalizing to a measurement containing 2 µL of 125 nM H3-MTX.

Measuring phospho-ERK and total-ERK

To measure relative levels of phospho-ERK (pERK) compared to total-ERK (tERK), we used an enzyme-linked immunosorbent assay ((ELISA), Abcam #176660). Small and large intestine-derived monolayers were cultured in Matrigel-coated 48-well tissue culture plates for 48 h. After 48 h, intestinal monolayers were washed with warm OBM and incubated with indicated concentration of erlotinib for 6 h. After drug incubation, intestinal monolayers were washed 2× with 250 µL ice-cold PBS and lysed for 30 min. Cell lysates were used to quantify the levels of

pERK and tERK according to the manufacturer's protocol. Measured pERK and tERK levels were first normalized by subtracting background intensity, then each sample's pERK intensity was normalized to its tERK intensity. Each sample was measured in duplicate.

Murine phospho-RTK array

The phospho-RTK array was performed according to the manufacturer's protocol (R&D Systems #ARY014) with cell lysates collected from small and large intestine-derived monolayers cultured for 48 h. Two different biological assays were performed, images are representative of both experiments and quantifications include both experiments.

CYP3A activity assay

To measure CYP3A activity, the P450-Glo CYP3A4 assay with luciferin-IPA (Promega #V9001) was used (Lee et al., 2013). We note CYP3A11 is the murine homolog of CYP3A437. Intestinal monolayers were cultured in 96-well imaging plates with WENR media. For induction assay, WENR media containing dexamethasone was added 4 h after seeding. After 48 h, cells were washed with OBM and WENR media containing 3 μM luciferin-IPA was added. Cells were incubated at 37 °C for one hour. After incubation, cleaved luciferin-IPA was detected by aliquoting supernatant and luciferin detection reagent at a 1:1 ratio to an opaque white 96-well plate (Corning #353296). The plate was incubated at room temperature for 20 min, then luminescence was measured on a Biotek H4 plate reader with an integration time of 1 s/well. CYP3A activity was calculated by first subtracting background luminescence measured from wells containing no cells. Then each well was normalized to its cell viability (see 'Cell viability assay').

Cell viability assay

To measure cell viability, the CellTiter-Glo 3D cell viability assay (Promega #G9681) was used. Intestinal monolayers were cultured and at the indicated time-point an equal amount of CellTiter Glo was added to cells. Plates were put on a shaker for 5 min, then incubated at room temperature for 25 min. After incubation, 100 µL supernatant was transferred to a white opaque 96-well plate, then luminescence was measured on a Biotek H4 plate reader with an integration time of 1 s/well.

Liquid chromatography tandem mass spectrometry assay

CP and 4-OHCP detection were performed by culturing small and large intestine-derived monolayers in 48-well tissue culture plates for 24 h. After 24 h, intestinal monolayers were washed with OBM and WENR media containing 100 µM CP was added for 24 h. After drug incubation, 100 µL supernatant was collected and 10 µL of 2 M semicarbazide (SCZ) in 50 mM phosphate buffer (pH7.4) was added to convert 4-OHCP to a more stable semicarbazone derivative. Samples were centrifuged at 16,000 g for 20 min at 4 °C before using a liquid chromatography tandem mass spectrometry (LC-MS/MS; Shimadzu 20AD XR UFLC pumps and Sciex API5000 tandem mass spectrometer) to detect CP and 4-OHCP.

In brief, 10 µL of samples and internal standards (200 ng/mL CP-d4 and 200 ng/mL 4-OHCP-d4 semicarbazone) were loaded into an oasis HLB 96-well µ-elution solid phase extraction plate. Samples were washed 2x with 50 µL water, eluted 2x with 15 µL acetonitrile, and mixed with 70 µL water. 2 µL of processed samples were injected into a poroshell 120 pentafluorophenyl (PFP) column (50 × 2.1 mm, 2.7 µm, Agilent Tech.), eluted with 10 mM ammonium formate at pH 4 (A) and 0.1% formic acid in acetonitrile (B) in gradient mode [B% (t, min): 4-4-47-90-90-4-4 (0-1-3-3.01-3.50-3.51-4.5)], flow rate was 0.6 mL/min). Electrospray

ionization in positive mode and multiple reaction monitoring were used. The ion pairs m/z 261→233 for CP, m/z 267→237 for CP-d4, m/z 334→221 for 4-OHCP-SCZ and m/z 340→114 for the internal standard 4-OHCP-d4-SCZ were selected for quantification. MS parameters: CAD, 11; CUR, 20; GS1, 50; GS2, 45; IS, 2000v; TEM: 600 °C; Resolution, high for Q1 and Q3. The retention times were typically 2.80 min for CP and its internal standard and 2.45 min for 4-OHCP and its internal standard. Total run time was 4.5 min per sample. Due to instability of 4-OHCP, the stock solution for calibration curve was generated from 4-hydroperoxycyclophosphamide assuming 100% conversion, followed by in situ derivatization with 2 M SCZ in 50 mM phosphate buffer (pH7.4). Calibration range was 0.19–47.9 µM for CP and 0.070–17.5 µM for 4-OHCP.

Immunofluorescence assay

Intestinal monolayers were washed 1x with warm D-PBS and then fixed with 4% paraformaldehyde in PBS for 15 min at room temperature. Cells were then washed with PBS and permeabilized with 0.5% Triton-X-100 in PBS at room temperature for 10 min. Cells were washed, blocked with 3% BSA in PBS for 30 min, and then incubated in primary antibody in antibody buffer (PBS with 0.3% Triton-X-100, 1% BSA) overnight at 4 °C. The next day, cells were washed and incubated with secondary antibodies and Hoechst 33342 (5 µg/mL; Invitrogen #H3570) in antibody buffer for 2 h at room temperature.

For histology, intestines were harvested from mice, cut open longitudinally, and incubated in 4% paraformaldehyde in PBS for 2 h at 4 °C. Tissues were then embedded in OCT, frozen, and sectioned at 10 µm. For Ki67 staining, sections were blocked in blocking buffer (0.1 M Tris-HCl, 0.15 M NaCl, 5 µg/mL blocking reagent (Perkin Elmer #FP1020), pH 7.5) containing 5% goat serum (Jackson Labs #005-000-121) for 1 h at room temperature. Sections

were than incubated in primary antibody in blocking buffer for 1 h at room temperature. Sections were washed, then incubated with secondary antibody and Hoechst 33342 in blocking buffer for 40 min at room temperature. For TUNEL assays the FITC-TUNEL Assay Kit (Abcam #66108) was used according to the manufacturer's instructions. Sections were then mounted in Vectashield (Vector Laboratories #H-100) and visualized on the 10x objective of a Nikon Ti Eclipse microscope.

Antibodies

All antibodies were purchased from suppliers and used as designated without further purification as indicated in Table 3.4.

EdU pulse and visualization

To visualize proliferating cells (specifically, those in S phase), intestinal monolayers were incubated with 10 μM EdU (Thermo Fisher #A10044) in media for 2 h prior to fixation. After immunofluorescence staining, EdU+ cells were visualized using Click chemistry (Salic et al., 2008). Cells were incubated with a reaction mixture containing 1 mM CuSO4 (VWR International #470300-880), 5 μM sulfo-Cyanine5 azide (Lumiprobe #B3330) or 5 μM BDP-FL azide (Lumiprobe #11430), and 100 mM sodium ascorbate (Sigma Aldrich #A4034) in PBS for 30 min at room temperature.

Automated confocal microscopy

Intestinal monolayers were imaged on the 20x water objective of an Operetta CLS High-Content Analysis System on confocal mode with a binning of 2. The area of each well was covered by 61 individual scans. In each field of view, 4 z-planes were collected. Analyzed and representative images were all from maximum projections.

Immunofluorescence image segmentation and quantification

General information

Image segmentation was performed using the PerkinElmer Harmony 4.9 software. Starting with maximum intensity projections of stain images, we segmented and then quantified the number of nuclei, proportion of specific cell types, or stain intensity. The segmentation process for each object type typically consisted of three steps: a preprocessing step, a segmentation step to generate boundaries of objects, and a selection step to select correctly segmented objects.

Segmenting nuclei

Hoechst stain images were first smoothed through convolution with a gaussian filter (Width: 3 px). Nuclei were then found using a modified "Find Nuclei" algorithm with Method M (Diameter: 22 μm, Splitting Sensitivity: 0.40, Common Threshold: 0.10). To remove incorrectly segmented nuclei, morphological and intensity properties of each segmented nuclei were calculated. The "Calculate Intensity Properties" algorithm with Method Standard was used to calculate the mean intensity of each segmented nuclei. The "Calculate Morphology Properties" algorithm with Method Standard was used to calculate the roundness of each segmented nuclei. Selected nuclei were found with the "Select Population" algorithm with Method Filter by Property, such that selected nuclei have an intensity > 500 and a roundness > 0.75.

Segmenting proliferative cells

EdU stain images were segmented the same as nuclei. The only difference is selected EdU+ nuclei were found using an intensity > 225.

Segmenting enteroendocrine cells

Chromogranin A (ChgA) stain images were filtered with the same filter described for nuclei segmentation. Then enteroendocrine cells were found using the "Find Cells" algorithm with

Method C (Common Threshold: 0.80, Area: >100 μm2, Splitting Coefficient: 200, Individual Threshold: 0.80, Contrast: >0.20). The "Calculate Intensity Properties" algorithm with Method Standard was used to calculate the mean intensity of each segmented enteroendocrine cell. The "Calculate Morphology Properties" algorithm with Method Standard was used to calculate the area and roundness of each segmented enteroendocrine cell. Selected enteroendocrine cells were found with the "Select Population" algorithm with Method Filter by Property, such that each selected enteroendocrine cell has an intensity > 1200, area < 400, and roundness > 0.65.

Segmenting goblet cells

Mucin 2 (Muc2) stain images were filtered with the same filter described for nuclei segmentation. Then goblet cells were found using the "Find Cells" algorithm with Method M (Common Threshold: 0.50, Diameter: 25 μm, Splitting Sensitivity: 0.05). The "Calculate Intensity Properties" algorithm with Method Standard was used to calculate the mean intensity of each segmented goblet cell. The "Calculate Morphology Properties" algorithm with Method Standard was used to calculate the area of each segmented goblet cell. Selected goblet cells were found with the "Select Population" algorithm with Method Filter by Property, such that each selected goblet cell has an intensity > 500 and area > 150.

Segmenting Paneth cells

Lysozyme (Lyz) stain images were filtered with the same filter described for nuclei segmentation. Then Paneth cells were found and selected using the "Find Cells" algorithm with Method C (Common Threshold: 0.90, Area > 100 μm2, Splitting Coefficient: 22.0, Individual Threshold: 0.70, Contrast > 0.10). No selection step was used.

Segmenting enterocytes

Villin (Vil) stained regions of images were found using the "Find Image Region" algorithm with Method Common Threshold (Threshold: 0.50, Split into Objects: selected, Area > 20 μm2). Nuclei within the Vil+ region were found as described for nuclei segmentation. The "Calculate Intensity Properties" algorithm with Method Standard was used to calculate the mean intensity of the Vil channel in each segmented nucleus. The "Calculate Morphology Properties" algorithm with Method Standard was used to calculate the roundness of each segmented nuclei. Selected nuclei within Vil+ regions were found with the "Select Population" algorithm with Method Filter by Property, such that selected nuclei have a Vil intensity > 500 and roundness > 0.75.

Segmenting SATB2+ nuclei

Special AT-rich sequence-binding protein 2 (SATB2) stain images were filtered with the same filter described for nuclei segmentation. SATB2 + nuclei were then found using a modified "Find Nuclei" algorithm with Method M (Diameter: 26 μm, Splitting Sensitivity: 0.30, Common Threshold: 0.20). The "Calculate Intensity Properties" algorithm with Method Standard was used to calculate the mean intensity of the SATB2 and Hoechst channel in each segmented nucleus. The "Calculate Morphology Properties" algorithm with Method Standard was used to calculate the roundness and area of each segmented nucleus. Selected SATB2 + nuclei were found with the "Select Population" algorithm with Method Filter by Property, such that selected SATB2 + nuclei have DAPI intensity >500, 500< SATB2 intensity < 1600, roundness > 0.85, and 70 μm2 < area ≤ 300 μm2.

Quantifying Lrig1 tissue intensity

Leucine-rich repeats and Ig-like domains-1 (Lrig1) stain images were quantified by first identifying tissue regions in each image. Tissue regions were found by the "Find Image Region"

algorithm using the Lrig1 channel with Method Common Threshold (Threshold: 0.50, area > 1000px2, and Fill Holes selected). The "Calculate Intensity Properties" algorithm with Method Standard was used to calculate the mean intensity of Lrig1 in selected tissue regions. Next, background (non-tissue) regions were found by the "Find Image Region" algorithm using the Lrig1 channel with Method Absolute Threshold (Lowest Intensity ≥ 0, Highest Intensity ≤ 400, area > 0px2, and Fill Holes selected). The "Calculate Intensity Properties" algorithm with Method Standard was used to calculate the mean intensity of Lrig1 in background regions. The Lrig1 tissue and background intensity were averaged across 25 fields/well and then Lrig1 background intensity was subtracted from Lrig1 tissue intensity. The measurements of 5 wells are depicted.

Quantifying EGFR cellular intensity

To quantify the intensity of EGFR per cell, both EGFR and Hoechst stain images were used. First, all nuclei were found as described in "segmenting nuclei." Then for each nuclei a cell region was calculated using the "Find Surrounding Region" algorithm with Method C (Common Threshold: 0.10, Individual Threshold: 0.70). The "Calculate Intensity Properties" algorithm with Method Standard was used to calculate the mean intensity of EGFR in each selected cell region. Density plots for the intensity of EGFR per cell are depicted and include ≥50,000 cells from 5 wells.

qRT-PCR

RNA was harvested from both intestinal monolayers and murine crypts using an RNEasy Plus Mini Kit (Qiagen #74136). Reverse transcription was performed using iScript Reverse Transcription kit (Bio-Rad #1708841). Quantitative PCR was performed using SsoAdvanced Universal SYBR Green Supermix (Bio-Rad #1725272) on a BioRad CFXConnect. Test gene

values were normalized to β-actin values. RNA levels were determined using the primers listed in Table 3.5.

RNA sequencing analysis

RNA was harvested from either intestinal monolayers cultured for 24 h or from freshly isolated murine crypts using an RNEasy Plus Mini Kit. Library preparation and sequencing were outsourced to Genewiz, Inc. (South Plainfield, NJ). RNA sequencing was performed on the Illumina HiSeq. Paired-end sequencing reads were aligned to the reference genome GRCm38 and annotated to vM25.primary_assembly obtained from gencode (htttps://www.gencodegenes.org/mouse) using STAR v.2.7.9a and featureCounts v.2.0.2 (Dobin et al., 2013; Liao et al., 2014). The obtained gene count data was normalized by using DESeq2 v.3.13 (Love et al., 2014), followed by log1p transform. Hierarchical clustering of 110 intestine marker genes was conducted by calculating the Euclidian distance with the "clustermap" function of the package seaborn v.0.11.1 in Python (Kwon et al., 2021; Li et al., 2017). Next, the average normalized gene counts across three replicates were calculated for each sample for the 110 intestine marker genes. The pairwise Pearson's correlation across samples was calculated using the "corrcoef" function of the package NumPy v.1.21 in Python.

Toxicity screen data processing

Calculation of change in total cell number

The number of nuclei after drug treatment (average of 3 wells) was divided by the number of nuclei in control treatment (average of 6 wells) from the same plate. A drug was counted as having a "toxic" effect on total cell number only if the mean of its high concentration replicates decreased cell number by more than 2 standard deviations ($2\sigma = .28$) of the average number of nuclei in control wells across the 8 screened plates.

Calculation of change in proliferative cell number

The number of EdU+ cells after each drug treatment (average of 3 wells) was divided by the number of EdU+ cells in the control treatment (average of 6 wells) from the same plate. A drug was counted as having a "toxic" effect on proliferative cell number only if the mean of its high concentration replicates decreased proliferative cell number by more than 2 standard deviations ($2\sigma = 0.58$) of the average number of EdU+ cells in control wells across the 8 screened plates.

Statistics and reproducibility

To calculate statistical significances, we made use of a two-sided two-way analysis of variance (ANOVA) followed by Sidak's multiple comparison test or a two-sided unpaired t-test with Welch's correction.

Data availability

The RNA sequencing data included in this study are deposited in Gene Expression Omnibus (GEO) with the accession code GSE191018.

Code availability

Automated image analysis to quantify the number of total cells and specific cell types was conducted on the Harmony High-Content Imaging and Analysis Software Version 4.9. For detailed parameters see 'Methods'. Figures were generated from GraphPad Prism Version 7.1.

TABLES

Table 3.1: Screened oncology drugs.

Class	Subclass	Name	Concentrations (μM)	IC50 (μM)[18]	Cmax (μM)[19]	GI Adverse Events*
alkylating agents	metal salts	carboplatin	40, 0.4	na	135.00	v,p,d,c
		oxaliplatin	50, 0.5	41	4.96	v,n,m
	nitrosoureas	carmustine	100, 1	452	19.40	v,n
		lomustine	100, 1	na	na	v,n,s
		streptozocin	10, 0.01	na	1438.00	v,n,d
	hydrazines/ triazines	dacarbazine	2.5, 0.025	na	34.40	v,n
		temozolomide	20, 0.2	375	37.60	v,n,d,c
	nitrogen mustards	cyclophosphamide	100, 1	180	128.00	v,n,d,co
		chlorambucil	100, 1	na	1.62	v,n,d
		melphalan	10, 0.1	na	9.17	v,n,d,m
microtubule inhibitors	destabilizing	vincristine	5, 0.05	0.20	1.48	c
		vinorelbine	40, 0.4	0.05	0.81	v,n,c
		vinblastine	5, 0.05	0.03	0.04	v,n,d,c,m
	stabilizing	paclitaxel	5, 0.05	0.08	4.27	v,n
		docetaxel	100, 1	0.1	5.47	v,n,d,c,co
topoisomerase inhibitors	I	topotecan	40, 0.4	1.1	0.02	v,n,d
		irinotecan	30, 0.3	14	5.78	v,n,p,d,c
		SN-38	5, 0.05	0.02	0.14	v,n,p,d,c
	II	doxorubicin	50, 0.5	0.2	6.73	v,n
		epirubicin	10, 0.01	0.4	16.60	v,n,d,m
		mitoxantrone	90, 0.9	1.6	0.72	v,n,m
		etoposide	50, 0.5	4.7	33.40	p,c
antimetabolite	antifolates	methotrexate	40, 0.4	0.6	1.31	v,d,s
		pemetrexed	5, 0.05	15	306.00	v,n,a
	urea	hydroxyurea	100, 1	na	795.00	unspecified
	pyrimidine analogs	5-fluorouracil	100, 1	110	426.00	d,m
		capecitabine	30, 0.3	na	21.10	v,n,d
	purine analogs	6-mercaptopurine	20, 0.2	na	0.59	n
		fludarabine	50, 0.5	111	na	v,n
		cladribine	30, 0.3	na	0.17	p
	nucleoside analogs	gemcitabine	50, 0.5	0.03	89.30	v,n
		cytarabine	100, 1	4.6	54.40	v,n
kinase inhibitors	EGFR	erlotinib	2.5, 0.025	13	3.15	v,n,d
		gefitinib	100, 1	23	0.36	d
	VEGFR/EGFR	vandetanib	10, 0.1	na	2.16	n,p,d,co
	BRAF	vemurafenib	10, 0.1	na	127.00	n
	HER2	lapatinib	10, 0.1	21	4.18	n,d
	ALK	crizotinib	50, 0.5	21	0.91	v,n,d,c
	BCR/ABL	bosutinib	10, 0.1	5.9	0.38	v,n,p,d
		imatinib	10, 0.1	16	7.50	v,n,p,d
		nilotinib	10, 0.1	30	0.84	n,p,d,c
	multiple	sorafenib	10, 0.1	14	20.10	n,p,d,b
other antineoplastics	antibiotic	bleomycin	5, 0.05	5.4	706.00	none
	proteasome inhibitors	bortezomib	100, 1	0.01	0.31	v,n,d,c
		ixazomib	100, 1	na	0.12	v,n,d,c
		carfilzomib	20, 0.2	na	5.88	none
	retinoid	bexarotene	20, 0.2	32	3.39	n,p
	immunomodulator	lenalidomide	50, 0.5	46	1.74	n,d,c

* Common clinical GI adverse events listed on FDA drug prescription label.
[18]Geometric mean of screened cancer lines in the Genomics of Drug Sensitivity in Cancer database
v: vomiting; p: pain; d: diarrhea; c: constipation; n: nausea; m: mucositis; co: colitis; s: stomatitis; a: anorexia; b: bleeding; na: not available

Table 3.2: Drug hits for total (top) and proliferative (bottom) cell numbers by drug class.

	Alkylating agents	Microtubule inhibitors	Topo. inhibitors	Anti-metabolite	Kinase inhibitors	Other
Small intestine	70% (7/10)	80% (4/5)	100% (7/7)	90% (9/10)	90% (9/10)	100% (6/6)
Large intestine	40% (4/10)	100% (5/5)	86% (6/7)	80% (8/10)	80% (8/10)	67% (4/6)

	Alkylating agents	Microtubule inhibitors	Topo. inhibitors	Anti-metabolite	Kinase inhibitors	Other
Small intestine	60% (6/10)	80% (4/5)	86% (6/7)	60% (6/10)	40% (4/10)	83% (5/6)
Large intestine	10% (1/10)	80% (4/5)	71% (5/7)	40% (4/10)	60% (6/10)	50% (3/6)

Table 3.3: Calculated LC50 for drug dose-responses.

	Total cell number		Proliferative cell number	
	Small intestine (μM)	Large intestine (μM)	Small intestine (μM)	Large intestine (μM)
Cyclophosphamide	N.A.	N.A.	30.55	N.A.
Methotrexate	0.202	N.A.	0.053	N.A.
Pemetrexed	N.A.	N.A.	0.298	N.A.
Erlotinib	1.959	0.417	3.733	0.646
Gefitinib	0.885	0.519	1.995	0.282
Osimertinib	0.740	0.471	0.863	0.301

N.A.: not applicable

Table 3.4: Concentration of antibodies used in study.

Epitope	Vendor and Catalog #	Dilution
Lyz	Dako #A0099	1:2000
ZO-1	Invitrogen #33-9100	1:1000
E-Cadherin	Cell Signaling #3195 S	1:400
SATB2	Santa Cruz Biotechnology #81376	1:50
Villin	BD Biosciences #610358	1:100
Muc2	Santa Cruz Biotechnology #15334	1:100
ChgA	Santa Cruz Biotechnology #393941	1:100
αSMA	Abcam #32575	1:500
Ki67	Cell Signaling #9129 S	1:500
EGFR	Abcam #52894	1:500
Lrig1	R&D Systems #AF3688-SP	1:20

Table 3.5: Primers used in study

Target mRNA	Forward Primer (5′ to 3′)	Reverse Primer (5′ to 3′)
RFC	GGGTGTTGTAGTCTGCGTGT	CACTCCACCTTGCACTACCC
PCFT	ATCTACCCGGCCACTCTGAA	AGGAAACTGCTGGAACTCCG
Ki67	GTCAGCAAGAGGCAGCAAGGGG	CTGGGTCTTTGCCACTGGCTGG
EGFR	TCTTCAAGGATGTGAAGTGTG	TGTACGCTTTCGAACAATGT
Cyp3a11	TCACACACACAGTTGTAGGGAGAA	GTCCATCCCTGCTTGTTTGTC
Cyp3a13	ACCGGCGGCGCTTTG	ATTCTCAGAGATAGAGATGGCCTTTT
Cyp3a41	GGTTGTACCACGGGATGTAGTTATAA	TCTGATGTTCTTAGACACTGCC TTTC
β-*actin*	CGCCACCAGTTCGCCATGGA	TACAGCCCGGGGAGCATCGT

REFERENCES

Al-Saffar A., Costa A., Delaunois A. et al. (2015). Gastrointestinal safety pharmacology in drug discovery and development. *Principles of Safety Pharmacology*, 229:291–321.

Andreyev H.J.N., Davidson S.E., Gillespie C. et al. (2012). Practice guidance on the management of acute and chronic gastrointestinal problems arising as a result of treatment for cancer. *Gut*, 61:179–192.

Balázsi G., van Oudenaarden A., Collins J.J. (2011). Cellular decision making and biological noise: from microbes to mammals. *Cell*, 144:910-925.

Basak O., Beumer J., Wiebrands K. et al. (2017). Induced quiescence of Lgr5+ stem cells in intestinal organoids enables differentiation of hormone-producing enteroendocrine cells. *Cell Stem Cell*, 20:177-190.

Batlle E., Henderson J.T., Beghtel H. et al. (2002). Beta-catenin and TCF mediate cell positioning in the intestinal epithelium by controlling the expression of EphB/ephrinB. *Cell*, 11:251-263.

Beumer J., Clevers H. (2016). Regulation and plasticity of intestinal stem cells during homeostasis and regeneration. *Development*, 143:3639-3649.

Beumer J., Clevers H. (2021). Cell fate specification and differentiation in the adult mammalian intestine. *Nature Reviews Molecular Cell Biology*, 22:39-53.

Birchenough G.M.H., Nyström E.E.L., Johansson M.E.V. et al. (2016). A sentinel goblet cell guards the colonic crypt by triggering Nlrp6-dependent Muc2 secretion. *Science*, 352:1535-1542.

Bjerknes M., Cheng H. (1999). Clonal analysis of mouse intestinal epithelial progenitors. *Gastroenterology*, 116:7-14.

Boussios S., Pentheroudakis G., Katsanos K. et al. (2012). Systemic treatment-induced gastrointestinal toxicity: incidence, clinical presentation and management. *Annals of Clinical Gastroenterology and Hepatology*, 25:106–118.

Bowcutt R., Forman R., Glymenaki M. et al. (2014). Heterogeneity across the murine small and large intestine. *World Journal of Gastroenterology*, 20:15216–15232.

Brandenberg N., Hoehnel S., Kuttler F. et al. (2020). High-throughput automated organoid culture via stem-cell aggregation in microcavity arrays. *Nature Biomedical Engineering*, 4:863–874.

Carr D.F., Ayehunie S., Davies A. et al. (2017). Towards better models and mechanistic biomarkers for drug-induced gastrointestinal injury. *Pharmacology and Therapeutics,* 172:181–194.

Cheng H., Leblond C.P. (1974a). Origin, differentiation and renewal of the four main epithelial cell types in the mouse small intestine. V. Unitarian theory of the origin of the four epithelial cell types. *American Journal of Anatomy*, 141:537-561.

Cheng H., Leblond C.P. (1974b). Origin, differentiation and renewal of the four main epithelial cell types in the mouse small intestine. I. Columnar cell. *American Journal of Anatomy*, 141:461-479.

Chelakkot C., Ghim J., Ryu S.H. (2018). Mechanisms regulating intestinal barrier integrity and its pathological implications. *Experimental and Molecular Medicine*, 50:1–9.

Clevers H. (2013). The intestinal crypt, a prototype stem cell compartment. *Cell*, 154:274-284.

Cook D., Brown D., Alexander D. et al. (2014). Lessons learned from the fate of AstraZeneca's drug pipeline: a five-dimensional framework. *Nature Reviews Drug Discovery,* 13:419–431.

Dames P., Bergann T., Fromm A. et al. (2015). Interleukin-13 affects the epithelial sodium channel in the intestine by coordinated modulation of STAT6 and p38 MAPK activity. *Journal of Physiology*, 593:5269-5282.

Denny K. H., Stewart D. W. (2017). Acute, sub-acute, sub-chronic and chronic general toxicity testing for preclinical drug development. *A Comprehensive Guide to Toxicology in Preclinical Drug Development (Second Edition)* 109–127.

Dobin A., Davis C.A., Schlesinger F. et al. (2013). STAR: ultrafast universal RNA-seq aligner. *Bioinformatics*, 29:15–21.

Down M.J., Arkle S., Mills J.J. (2007). Regulation and induction of CYP3A11, CYP3A13 and CYP3A25 in C57BL/6J mouse liver. *Archives of Biochemistry and Biophysics*, 457:105–110.

Elting L.S., Cooksley C., Chambers M. et al. (2003). The burdens of cancer therapy. *Cancer*, 98:1531–1539.

Farin H.F., Jordens I., Mosa M.H. et al. (2016). Visualization of a short-range Wnt gradient in the intestinal stem-cell niche. *Nature*, 530:340–343.

Feng X.H. , Derynck R. (2005). Specificity and versatility in TGF-beta signaling through Smads. *Annual Review of Cell and Developmental Biology*, 21:659-693.

Fleming R.A. (1997). An overview of cyclophosphamide and ifosfamide pharmacology. *Pharmacotherapy*, 17:146–154.

Flentjar N., Chu P.Y., Ng A.Y.N. et al. (2007). TGF-betaRII rescues development of small intestinal epithelial cells in Elf3-deficient mice. *Gastroenterology*, 132:1410-1419.

Gehart H., Clevers H. (2019). Tales from the crypt: new insights into intestinal stem cells. *Nature Reviews Gastroenterology & Hepatology*, 16:19–34.

Haber A.L., Biton M., Rogel N. et al. (2017). A single-cell survey of the small intestinal epithelium. *Nature*, 551:333-339.

Hahn S., Nam M.O., Noh J.H. et al. (2017). Organoid-based epithelial to mesenchymal transition (OEMT) model: From an intestinal fibrosis perspective. *Scientific Reports*, 7:2435.

Han L., Diehl A., Nguyen N.K. et al. (2014). The Notch pathway inhibits TGFβ signaling in breast cancer through HEYL-mediated crosstalk. *Cancer Research*, 74:6509-6518.

Harirforoosh S., Asghar A., Jamali F. (2013). Adverse effects of nonsteroidal antiinflammatory drugs: an update of gastrointestinal, cardiovascular and renal complications. *Journal of Pharmacy & Pharmaceutical Sciences*, 16:821–847.

He. X.C., Zhang J., Tong W.G. et al. (2004). BMP signaling inhibits intestinal stem cell self-renewal through suppression of Wnt-beta-catenin signaling. *Nature Genetics*, 36:1117-1121.

Hong S.P., Song S., Cho S.W. et al. (2017). Generation of PDGFRα+ cardioblasts from pluripotent stem cells. *Scientific Reports*, 7:41840.

Houde M., Laprise P., Jean D. et al. (2001). Intestinal epithelial cell differentiation involves activation of p38 mitogen-activated protein kinase that regulates the homeobox transcription factor CDX2. *Journal of Biological Chemistry*, 276:21885-21894.

Jansen G., van der Heijden J., Oerlemans R. et al. (2004). Sulfasalazine is a potent inhibitor of the reduced folate carrier: implications for combination therapies with methotrexate in rheumatoid arthritis. *Arthritis & Rheumatology*, 50:2130–2139.

Kiela P.R., Ghishan F.K. (2016). Physiology of intestinal absorption and secretion. *Best Practice & Research Clinical Gastroenterology*, 30:145–159.

Koch S., Nusrat A. (2012). The life and death of epithelia during inflammation: lessons learned from the gut. *Annual Review of Pathology*, 7:35-60.

Kwon O., Jung K.B., Lee K.R. et al. (2021). The development of a functional human small intestinal epithelium model for drug absorption. *Science Advances*, 7:673–676.

Laederich M.B., Funes-Duran M., Yen L. et al. (2004). The leucine-rich repeat protein LRIG1 is a negative regulator of ErbB family receptor tyrosine kinases. *Journal of Biological Chemistry*, 279:47050–47056.

Lander A.D., Gokoffski K.K., Wan F.Y.M. et al. (2009). Cell lineages and the logic of proliferative control. *PLOS Biology*, 7:e15.

Lee C., Ding X., Riddick D.S. (2013). Downregulation of mouse hepatic CYP3A protein by 3-methylcholanthrene does not require cytochrome P450-dependent metabolism. *Drug Metabolism and Disposition*, 41:1782–1786.

Lenz H.J. (2006). Anti-EGFR mechanism of action: antitumor effect and underlying cause of adverse events. *Oncology*, 20:5–13.

Li, H., Courtois E.T., Sengupta D. et al. (2017). Reference component analysis of single-cell transcriptomes elucidates cellular heterogeneity in human colorectal tumors. *Nature Genetics*, 49:708–718.

Li Y., Liu Y., Liu B. et al. (2018). A growth factor-free culture system underscores the coordination between Wnt and BMP signaling in Lgr5+ intestinal stem cell maintenance. *Cell Discovery*, 4:49.

Liao Y., Smyth G.K., Shi W. (2014). featureCounts: an efficient general purpose program for assigning sequence reads to genomic features. *Bioinformatics*, 30:923–930.

Liston D., Davis M. (2017). Clinically relevant concentrations of anticancer drugs: a guide for nonclinical studies. *Clinical Cancer Research*, 23:3489–3498.

Love M.I., Huber W., Anders S. (2014). Moderated estimation of fold change and dispersion for RNA-seq data with DESeq2. *Genome Biology*, 15:550.

Low J.E., Borch R.F., Sladek N.E. (1982). Conversion of 4-hydroperoxycyclophosphamide and 4-hydroxycyclophosphamide to phosphoramide mustard and acrolein mediated by bifunctional catalysis. *Cancer Research*, 42:830–837.

Lukonin I., Serra D., Challet L.C. et al. (2020). Phenotypic landscape of intestinal organoid regeneration. *Nature*, 586:275-280.

Mani R., St Onge R.P., Hartman J.L. et al. (2008). Defining genetic interaction. *Proceedings of the National Academy of Sciences USA*, 105:3461-3466.

Marshall J.L., DeLap R.J. (1994). Clinical pharmacokinetics and pharmacology of trimetrexate. *Clinical Pharmacokinetics*, 26:190–200.

Massagué J. (1998). TGF-beta signal transduction. *Annual Review of Biochemistry*, 67:753-791.

Matsu-Ura T., Dovzhenok A., Aihara E. et al. (2016). Intercellular Coupling of the Cell Cycle and Circadian Clock in Adult Stem Cell Culture. *Molecular Cell*, 64:900-912.

Milano J., McKay J., Dagenais C. et al. (2004). Modulation of notch processing by γ-secretase inhibitors causes intestinal goblet cell metaplasia and induction of genes known to specify gut secretory lineage differentiation. *Toxicological Sciences*, 82:341–358.

Múnera J.O., Sundaram N., Rankin S.A. et al. (2017). Differentiation of human pluripotent stem cells into colonic organoids via transient activation of BMP signaling. *Cell Stem Cell*, 21:51–64.

Murata K., Jadhav U., Madha S. et al. (2020). Ascl2-dependent cell dedifferentiation drives regeneration of ablated intestinal stem cells. *Cell Stem Cell*, 26:377-390.

Muta Y., Fujita Y., Sumiyama K. et al. (2018). Composite regulation of ERK activity dynamics underlying tumour-specific traits in the intestine. *Nature Communications*, 9:2174.

Nelson D.R., Zeldin D.C., Hoffman S.M.G. et al. (2004). Comparison of cytochrome P450 (CYP) genes from the mouse and human genomes, including nomenclature recommendations for genes, pseudogenes and alternative-splice variants. *Pharmacogenetics*, 14:1–18.

Nenci A., Becker C., Wullaert A. et al. (2007). Epithelial NEMO links innate immunity to chronic intestinal inflammation. *Nature*, 446:557–561.

Pass G.J., Carrie D., Boylan M. et al. (2005). Role of hepatic cytochrome p450s in the pharmacokinetics and toxicity of cyclophosphamide: studies with the hepatic cytochrome p450 reductase null mouse. *Cancer Research*, 65:4211–4217.

Pereira V.B.M., Melo A.T., Assis-Junior E.M. et al. (2016). A new animal model of intestinal mucositis induced by the combination of irinotecan and 5-fluorouracil in mice. *Cancer Chemotherapy and Pharmacology*, 77:323–332.

Pfau D., Guler E., Smith D.A. et al. (2020). Imaging features of gastrointestinal toxicity in non-small cell lung cancer patients treated with erlotinib: A single institute 13-year experience. *Clinical Imaging*, 68:210–217.

Potten C.S. (1998). Stem cells in gastrointestinal epithelium: numbers, characteristics and death. *Philosophical Transactions of the Royal Society B Biological Sciences*, 353: 821-830.

Qi X., Li Y., Zhao B. et al. (2017). BMP restricts stemness of intestinal Lgr5+ stem cells by directly suppressing their signature genes. *Nature Communications*, 8:13824.

Qiu A., Jansen M., Sakaris A. et al. (2006). Identification of an intestinal folate transporter and the molecular basis for hereditary folate malabsorption. *Cell*, 127:917–928.

Ramirez M., Rajaram S., Steininger R.J. et al. (2016). Diverse drug-resistance mechanisms can emerge from drug-tolerant cancer persister cells. *Nature Communications*, 7:10690.

Ribeiro R.A., Wanderley C.W.S., Wong D.V.T et al. (2016). Irinotecan- and 5-fluorouracil-induced intestinal mucositis: insights into pathogenesis and therapeutic perspectives. *Cancer Chemotherapy and Pharmacology*, 78:881–893.

Richmond C.A., Rickner H., Shah M.S. et al. (2018). JAK/STAT-1 signaling is required for reserve intestinal stem cell activation during intestinal regeneration following acute inflammation. *Stem Cell Reports*, 10:17-26.

Rodríguez-Colman M.J., Schewe M., Meerlo M. et al. (2017). Interplay between metabolic identities in the intestinal crypt supports stem cell function. *Nature*, 543:424-427.

Rubenstein E.B., Peterson D.E., Schubert M. et al. (2004). Clinical practice guidelines for the prevention and treatment of cancer therapy-induced oral and gastrointestinal mucositis. *Cancer*, 100:2026–2046.

Salic A., Mitchison T.J. (2008). A chemical method for fast and sensitive detection of DNA synthesis in vivo. *Proceedings of the National Academy of Sciences USA*, 105:2415-2420.

Sangild P.T., Shen R.L., Pontoppidan P. et al. (2018). Animal models of chemotherapy-induced mucositis: translational relevance and challenges. *American Journal of Physiology-Gastrointestinal and Liver Physiology*, 314:231–246.

Sanman L.E., Chen I.W., Bieber J.M. et al. (2020). Generation and quantitative imaging of enteroid monolayers. *Methods in Molecular Biology*, 2171:99-113.

Sanman L.E., Chen I.W., Bieber J.M. et al. (2021). Transit-amplifying cells coordinate changes in intestinal epithelial cell-type composition. *Developmental* Cell, 56:356–365.

Sato T., Stange D.E., Ferrante M. et al. (2011). Long-term expansion of epithelial organoids from human colon, adenoma, adenocarcinoma, and Barrett's epithelium. *Gastroenterology*, 141:1762-1772.

Sato T., Vries R.G., Snippert H.J. et al. (2009). Single Lgr5 stem cells build crypt-villus structures in vitro without a mesenchymal niche. *Nature*, 459:262–265.

Stamataki D., Holder M., Hodgetts C. et al. (2011). Delta1 expression, cell cycle exit, and commitment to a specific secretory fate coincide within a few hours in the mouse intestinal stem cell system. *PLOS One*, 6:e24484.

Suzuki A., Sekiya S., Gunshima E. et al. (2010). EGF signaling activates proliferation and blocks apoptosis of mouse and human intestinal stem/progenitor cells in long-term monolayer cell culture. *Laboratory Investigation*, 90:1425–1436.

Thorne C.A., Chen I.W., Sanman L.E. et al. (2018). Enteroid monolayers reveal an autonomous WNT and BMP circuit controlling intestinal epithelial growth and organization. *Developmental Cell*, 44:624–633.

Tian A., Benchabane H., Wang Z. et al. (2016). Regulation of stem cell proliferation and cell fate specification by wingless/Wnt signaling gradients enriched at adult intestinal compartment boundaries. *PLOS Genetics*, 12:e1005822.

Tian H., Biehs B., Warming S. et al. (2012). A reserve stem cell population in small intestine renders Lgr5-positive cells dispensable. *Nature*, 482:120.

van de Wetering M., Francies H.E., Francis J.M. et al. (2015). Prospective derivation of a living organoid biobank of colorectal cancer patients. *Cell*, 161:933–945.

van der Flier L.G., Clevers H. (2009). Stem cells, self-renewal, and differentiation in the intestinal epithelium. *Annual Review of Physiology*, 71:241-260.

van der Flier L.G., Haegebarth A., Stange D.E. et al. (2009). OLFM4 is a robust marker for stem cells in human intestine and marks a subset of colorectal cancer cells. *Gastroenterology*, 137:15-17.

van Es. J.H., Jay P., Gregorieff A. et al. (2005). Wnt signaling induces maturation of Paneth cells in intestinal crypts. *Nature Cell Biology*, 7:381-386.

van Es. J.H., Sato T., van de Wetering M. et al. (2012). Dll1+ secretory progenitor cells revert to stem cells upon crypt damage. *Nature Cell Biology*, 14:1099-1104.

van Hasselt J.G.C., Iyengar R. (2019). Systems pharmacology: defining the interactions of drug combinations. *Annual Review of Pharmacology and Toxicology*, 59:21-40.

VanDussen K.L., Carulli A.J., Keeley T.M. et al. (2012). Notch signaling modulates proliferation and differentiation of intestinal crypt base columnar stem cells. *Development*, 139:488-497.

Visentin M., Diop-Bove N., Zhao R. et al. (2014). The intestinal absorption of folates. *Annual Review of Physiology*, 76:251–274.

von Moltke J., Ji M., Liang H.E. et al. (2016). Tuft-cell-derived IL-25 regulates an intestinal ILC2–epithelial response circuit. *Nature*, 529:221-225.

Wardill H.R., Bowen J.M., Al-Dasooqi N. et al. (2014). Irinotecan disrupts tight junction proteins within the gut: implications for chemotherapy-induced gut toxicity. *Cancer Biology & Therapy*, 15:236–244.

Waring M. J., Arrowsmith J., Leach A.R. et al. (2015). An analysis of the attrition of drug candidates from four major pharmaceutical companies. *Nature Reviews Drug Discovery,* 14:475–486.

Wee P., Wang Z. (2017). Epidermal growth factor receptor cell proliferation signaling pathways. *Cancers*, 9:52.

Xie F., Ding X., Zhang Q.Y. (2016). An update on the role of intestinal cytochrome P450 enzymes in drug disposition. *Acta Pharmaceutica Sinica B*, 6:374–383.

Yamashita T., Inui T., Yokota J. et al. (2021). Monolayer platform using human biopsy-derived duodenal organoids for pharmaceutical research. *Molecular Therapy*, 22:263–278.

Yang W., Soares J., Greninger P. et al. (2013). Genomics of drug sensitivity in cancer (GDSC): a resource for therapeutics biomarker discovery in cancer cells. *Nucleic Acids Research*, 41:955–961.

Yilmaz Ö.H., Katajisto P., Lamming D.W. et al. (2012). mTORC1 in the Paneth cell niche couples intestinal stem-cell function to calorie intake. *Nature*, 486:490-495.

Yin X., Farin H.F., van Es J.H. et al. (2014). Niche-independent high-purity cultures of Lgr5+ intestinal stem cells and their progeny. *Nature Methods*, 11:106-112.

Zhan T., Ambrosi G., Wandmacher A.M. et al. (2019). MEK inhibitors activate Wnt signaling and induce stem cell plasticity in colorectal cancer. *Nature Communications*, 10:2197.

Zhang Y.E. (2009). Non-Smad pathways in TGF-β signaling. *Cell Research*, 19:128-139.

Publishing Agreement

It is the policy of the University to encourage open access and broad distribution of all theses, dissertations, and manuscripts. The Graduate Division will facilitate the distribution of UCSF theses, dissertations, and manuscripts to the UCSF Library for open access and distribution. UCSF will make such theses, dissertations, and manuscripts accessible to the public and will take reasonable steps to preserve these works in perpetuity.

I hereby grant the non-exclusive, perpetual right to The Regents of the University of California to reproduce, publicly display, distribute, preserve, and publish copies of my thesis, dissertation, or manuscript in any form or media, now existing or later derived, including access online for teaching, research, and public service purposes.

DocuSigned by:
Jake Bieber
0DC44756711E46F...
Author Signature

5/5/2022
Date